UNIVERSITY OF OSLO

MASTER'S THESIS

The Effect on Plasmonic Behaviour in Quasi Two-Dimensional GeSe by Variation in Thickness & Phases

---

Author:
Kristoffer VARSLOTT

Supervisor:
Prof. Andrej KUZNETSOV

Co-supervisors:
Dr. Calliope BAZIOTI
Jon BORGERSEN

UiO : University of Oslo

ő *A thesis submitted in fulfillment of the requirements for the master's degree in science*

Light and electricity from novel semiconductors (LENS)
Department of Physics
University of Oslo

June 1, 2021

Abstract

GeSe is a layered compound semiconductor that can be exfoliated to form a quasi-two dimensional material, moreover GeSe has attained a growing interest in the scientific community in recent years. However, the plasmonic behaviour of quasi-two dimensional GeSe is poorly investigated, which consequently opens up a novel opportunity of understanding the complex band structure of GeSe as a function of the decreasing dimensions and stoichiometric changes. From literature, the optical bandgap of two-dimensional α-GeSe is predicted to have a direct bandgap in the range of $1.16 - 1.66eV$*, in accordance with ab-initio simulations. Experimental evidence of the bandgap of bulk GeSe is found to be* $\sim 1.2eV$*, even though pure two-dimensional GeSe flakes is yet to be realised experimentally, we suggest some interesting result regarding the bandgap of quasi-two dimensional GeSe.*

In this work we present a comprehensive analysis of GeSe plasmonic behaviour under the influence of thickness and atomic concentration variations. The determination of plasmonic behaviour of GeSe was done by Electron Energy Loss spectroscopy (EELS), where we locally investigate regions of interest with a nanometer spatial resolution. In addition to analysing the plasmonic behaviour, we also give an estimate of the bandgap of quasi-two dimensional GeSe through simple linear fit method by EELS and micro-photoluminescence (micro-PL). As an extension to the analysis of plasmonic behaviour and bandgap, a topography determination of GeSe is given by the use of optical microscope, atomic force microscopy (AFM) and scanning electron microscopy (SEM).

The topography analysis of GeSe was two-fold 1) determination of flake-sizes along the elongated direction by optical microscope images. 2) Thickness variation within a single flake by AFM. The estimated average flake size along the elongated direction gave mean value of $3.044\mu m$ *with a standard deviation of* $\sigma = 1.819\mu m$*. These results suggest a high spatial resolution for accurate measurements. In some of the selected samples, the flake thickness varied down to 2.70nm, i.e. equivalent to 3 monolayers of GeSe. The plasmonic behaviour as a function of thickness was measured trough EELS, demonstrating interesting shifts in the plasmon peaks. Where the blue shift in energy of the plasmon peak took place approximately* $t \lesssim 22 \pm 1.2nm$*, for a range of* $10x10nm$ *area of Low-loss spectra, this blue shift was due to reduced thickness as well as stoichiometry variations. By reducing the low-loss spectra area to* $1.5x10nm$ *we managed to lower the standard deviation of the average thickness from* $\sim 7.53\%$ *to* $\sim 6.04\%$ *as well as decrease the measured thickness. An observed blue shift as well as a red shift was confirmed. Once the thickness decreased below* $t \sim 15 \pm 1.3nm$*, a drastic red shift took place - which was attributed to surface plasmons. A clear blue shift was also confirmed by plasmon peak variation as a function of phases, between GeSe (flake-like morphology), Se-rich (random morphology) and Ge-rich (Needle-like morphology), where the blue shift took place from* $\sim Ge_{0.5}Se_{0.5}$*,* $\sim Ge_{0.1}Se_{0.9}$ *to* $\sim Ge_{0.9}Se_{0.1}$*. Micro-PL measurements showed a prominent emission band centred at* $1.24eV$*, whereas the linear fit method from EELS showed a bandgap from* $\sim 1.53eV$ *at* $t \sim 50 \pm 1.8nm$ *to* $\sim 1.64eV$ *at* $t \sim 14 \pm 4.6nm$*. The pros and cons attributed to these techniques are discussed for the advantage of determining the bandgap of quasi-two dimensional materials as well as nano-particles.*

Acknowledgements

The tremendous love and support during my time at UiO can not go unoticed. I would like to start by thanking my supervisor Prof. Andrej Kuznetsov for introducing me to the field of condensed matter physics and for the ongoing enthusiasm and encouragement throughout my years at LENS. Furthermore, I would also give my sincerest gratitude to my co-supervisor/mentor Jon Borgersen for his considerate thoughts, excellent scientific expertize and encouraging words at difficult times. I would also like to give a huge thanks to my other co-supervisor/mentor, Dr. Calliope Bazioti, for her tremendous work, knowledge and hours discussing our results - I could not have done this without you. For the micro-PL measurements done, thank you Dr. Augustinas Galeckas, excellent work with difficult samples. I would also like to thank the rest of the team at LENS for letting me feel welcome.

To my fellow students at LENS, these past few years has been substantially improved because of you. Being able to discuss small victories and failures to on-another, with a never-ending optimism, has been a memorable experience.

Lastly, to my friends and family, I sincerely appreciate the immense patience and support you have given me throughout my years as a student.

Contents

Abstract **i**

Acknowledgements **iii**

1 Introduction **1**

2 Theory **3**

2.1 Condensed matter physics in bulk structures 4
2.1.1 Crystal structure & Momentum space 4
2.1.2 Density of States from 3D to 2D samples 8
2.1.3 Electronic Band Structure & Electron Occupation 13
2.2 Electrical transport in Two dimensional materials 15
2.2.1 Electrical conductivity & mobility 16
2.2.2 Quantum confinement & Scattering mechanisms 18
2.2.3 Multivalley semiconductors & interlayer coupling 23
2.3 The Envelope Function Approximation for Quasi-Two-Dimensional Systems & Dirac equation 24
2.3.1 Envelope Functions 24
2.3.2 Dirac equation - relativistic Schr*ö*dinger equation 25
2.4 Excitons - Quasiparticles in 2D 26
2.4.1 Electron band structure cont. 27
2.4.2 Electron-hole pairs - Creation of excitons 30
2.4.3 Exciton binding energy & recombination 31
2.4.4 Spin-Orbit coupling 34

3 Experimental Techniques **37**

3.1 Transmission Electron Microscopy (TEM) 37
3.1.1 Scanning Transmission Electron Microscopy (STEM) 38
3.1.2 Electron Energy Loss Spectrometry (EELS) 41
Plasmon energies and specimen thickness from EELS 44
3.1.3 Energy Dispersive X-Ray Spectroscopy (EDX) 46
3.2 Atomic Force Microscopy (AFM) 47
3.2.1 Working principles 47
3.2.2 Imaging mode: Tapping mode 48
3.3 Scanning Electron Microscope (SEM) 48

3.4 Photoluminescence Spectroscopy 50

4 Group IV-VI: GeSe - In light of TEM & PL 53

4.1 Crystal structure & properties 53

4.2 Determining topography of GeSe 56

4.2.1 SEM & optical microscopy of layered structure 56

4.2.2 AFM-result of GeSe layered structure 59

4.3 Transmission Electron Microcopy results (TEM) 62

4.3.1 STEM & EDX of GeSe (flake morphology) 62

4.3.2 STEM & EDX of Se-rich phases (random morphology) 66

4.3.3 STEM & EDX of Ge-rich phase (Needle-like morphology) 69

4.4 Plasmonic behaviour as a function of thickness through EELS 73

4.5 Plasmonic behaviour as a function of phase through EELS 77

4.6 Bandgap measurements - EELS & micro-PL 79

5 Conclusion 83

A Effective mass I 87

References 89

List of Figures

2.1 Crystal structures 5
2.2 Reciprocal lattice 9
2.3 Illustration: Density of states 2D 11
2.4 Illustration of bandgap in semiconductor 14
2.5 Electron mean free path 19
2.6 Electron-electron interaction: Conservation of momenta & Feynman diagram 20
2.7 Degenerate Valley-states in multivalley semiconductor 23
2.8 Band structure from electron dispersion relation 28
2.9 MoS_2 Irreducible Brillouin zone, band structure and density of states 29
2.10 Exciton - Electron-hole pair 31
2.11 Decay of excess carriers by recombination. 33
2.12 Spin-Orbit Coupling 34

3.1 STEM without and with monochromator illustrated 39
3.2 Illustration of STEM detectors 40
3.3 Schematic of EELS 42
3.4 Schematics of EELS spectra 43
3.5 Simplified illustration of EDX 46
3.6 Simplified AFM setup 47
3.7 Schematic illustration of scanning electron microscope 49

4.1 Visual presentation of the crystal structure of α-GeSe 54
4.2 Microscopic image of GeSe on a 1x1cm Si-substrate 57
4.3 Scanning Electron Microscope image of GeSe deposited on a 1x1cm Si-substrate. 58
4.4 Histogram distribution of flake sizes. 58
4.5 Topography image using AFM of GeSe - flake 1 59
4.6 Topography image using AFM of GeSe - flake 2 60
4.7 STEM images of GeSe flake, regions of interest (ROI) & EELS spectra obtained 63
4.8 High resolution STEM-image of GeSe_ROI_2 64
4.9 Energy Dispersive X-Ray Spectroscopy (EDX) of GeSe flake 64
4.10 STEM image of Se-rich phases, regions of interest (ROI) & EELS spectra obtained 66
4.11 EDX maps of Se-rich phase (ROI 1) 67
4.12 EDX maps of Se-rich phase (ROI 2) 68

4.13 STEM image of Ge-rich phases, regions of interest (ROI) & EELS spectra obtained 69
4.14 EDX maps of Ge/Se-rich phase (ROI 1) 70
4.15 EDX maps of Ge-rich phase (ROI 1) 71
4.16 Complete overview of elemental composition 71
4.17 Low-loss spectra of GeSe with 10x10nm inset. 73
4.18 Bandgap estimation as a function of thickness through a linear fit method . . 74
4.19 Low-loss spectra of GeSe with 1.5x10nm inset. 75
4.20 Plasmon peak energy as a function of phases 78
4.21 Micro-PL measurements of GeSe 80

List of Tables

4.1 Table of α & β - GeSe, showing space group, lattice vectors (a,b,c), interlayer distance (d), calculated fundamental bandgaps (E_g^{HSE}, HSE hybrid functional) for bulk and monolayers.. The star (*) indicates direct band gaps. 55
4.2 Table of elemental composition from EDX measurements. Local edge measurements GeSe_ROI_#_Edge* does not include oxygen. 65
4.3 Table of elemental composition from EDX measurements of Se-rich phases with some discrepencies marked with (*). Local measurements of Se_ROI_#_POS_# are included due to EELS measurements at these regions. Relative average thickness t/λ, and standard deviation σ_t. 68
4.4 Table of elemental composition from EDX measurements of Ge-rich phases with some discrepencies marked with (*). Local measurements of Ge_ROI_#_POS_# is included due to EELS measurements at these regions. Relative average thickness t/λ, and standard deviation σ_t. 72
4.5 Table of measured average thickness for each Low-loss spectrum in figure 4.17c) and 4.19c). Standard deviation of thickness is given by σ_t. 76

Chapter 1

Introduction

In the recent decades an extensive investigation in various two-dimensional materials has been conducted, and a vast majority directed towards Graphene since its discovery in 2004 [1, 2]. In these materials we are witness to some remarkable physics due to quantum confinement which will be addressed in the subsequent chapter 2. One of the most known phenomena occurring in two-dimensional materials is the increase in bandgap as one reaches the monolayer as well as a transition from indirect to direct bandgap. In this thesis one will investigate the bandgap behaviour from multiple factors, such as thickness and phases through Electron Energy Loss Spectrum (EELS). Quasi-two dimensional materials with direct bandgap attract a growing attention for opto-electronic applications including solar cells, photo-detectors, light-emitting diodes and photo-transistors, capacitive energy storage, photodynamic cancer therapy and sensing on flexible platform. Furthermore, one will get a comprehensive understanding of how plasmon peaks are effected by thickness and phases. An interesting feature of plasmon peaks in quasi-two dimensional materials is surface plasmon, surface plasmon submerge as a dominant attribute for low-volumed materials and will be addressed in chapter 4.

The thesis will deal with GeSe classified as a two-dimensional material. We work with GeSe flakes dispensed in isopropanol, delivered by *2dsemiconductors Inc*. This is, in theory, an atomically thin semiconductor in group IV-VI. GeSe is an appealing two-dimensional photovoltaic material due to its desirable electronic and optical properties as well as being an earth-abundant constituent element. The manufacturing of monolayer GeSe has proven difficult with a range of mechanical and syntesizing processes in play. Pure monolayer GeSe sheet is yet to be realised, however, a range of publications provide a relative thin GeSe sample down to just a few layers of GeSe sheets [3–8]. In this thesis we investigate the quasi-two dimensional material GeSe through Transmission electron microscopy (TEM), providing a nanoscale spatial resolution. To overcome the problem of producing pure monolayer GeSe, we extended the study to atomic resolution. The bandgap measurements are two-fold, 1) through micro-PL, 2) through electron energy loss spectroscopy (EELS) by linear fit method. In the former, one may achieve a spatial resolution of a few microns in diameter, however, it is impossible to focus on a single edge location, which ultimately provide an uncertain bandgap estimation due to many locally varying emission bands. In

EELS, which is a subset of TEM, one measures the energy loss of an electron passing through the sample. The great advantages of EELS is the atomic resolution enabling investigation at edges, this also produces the possibility of extreme local investigation of plasmon peaks. In EELS, one is unfortunately subject to lower energy resolution - which may be reduced to 0.1 - 0.01eV by applying a monochromator [9], enabling the possibility of detect Spin-Orbit coupling.

In chapter 2 an overview of the main theory is explained, where one goes through basic condensed matter physics in bulk structures and work our way down to two-dimensional systems in section 2.1. Followed by electrical transport in two dimensional materials, whereas various attributes such as electrical conductivity, mobility, quantum confinement, scattering mechanisms, multivalley semiconductor and interlayer coupling is discussed in section 2.2. A brief explanation of envelope function for quasi-two dimensional system is explained through the use of relativistic Schr*ö*dinger equation - namely the Dirac equation in section 2.3. The last section 2.4, goes into the depth about excitons in order to understand the optical bandgap occurring in our measurements.

In order to fully appreciate the results of this thesis one would need an introduction to the experimental techniques applied, therefore, chapter 3 introduces a variety of instruments which is used throughout this thesis. As we have bare minimum control over the mean value of size and thickness as well as elemental composition of the flakes dispensed in isopropanol, one would need to analyse them through various characterisation techniques. The techniques used are Atomic Force microscopy in order to give an estimation of the thickness profile of the flakes, Scanning Electron Microscope (SEM) used to characterise the topography, Scanning Transmission Electron Microscope (STEM) which is a powerful characterisation technique enabling high spatial resolution. Within STEM one is able to determine the elemental composition at high spatial resolution through Energy Dispersive X-Ray Spectroscopy (EDX). Furthermore In order to analyse the plasmon peaks and give an estimation of optical bandgap one could implement Electron Energy Loss Spectrometry (EELS). An introduction and explanation of these techniques are provided in chapter 3.

The results will be presented in chapter 4, where the first section is dedicated to the crystal structure and properties of GeSe, whereas the information provided is solely from former experimental and theoretical work. Furthermore, section 4.2 will give an overview of the topography of GeSe through some of the techniques given in chapter 3. The determination of various phases by atomic concentration as well as thickness will be provided by STEM, EDX and EELS in section 4.3. Lastly, the results of plasmon peak variation as a function of thickness and phases will be presented as well as bandgap measurements from EELS and micro-PL.

Chapter 2

Theory

> Study hard what interests you the most in the most undisciplined, irreverent and original manner possible.
>
> *Richard Feynmann*

In this chapter I would like to talk about some basic, yet, necessary physics. I will cover some important concepts of condensed matter physics, mesoscopic physics and quantum physics. In order to understand two dimensional samples, as well as the rich physics which is expressed in such materials. ***I would like to emphasize a great deal on the theory for the purpose of establishing a thorough understanding of the rich physics behind quasi-two dimensional materials in contrast to its bulk counterpart - and it will not be specified towards the results given in this thesis.***

Furthermore, some of the most important elements in this chapter will be condensed matte physics, where we firstly will consider bulk materials, and gradually work our way towards 2D materials. Transition Metal Dichalcogenides (TMDs) and other layered structures materials turns out to have sizable bandgaps that change from indirect to direct in single layers, allowing applications such as transistors, photodetectors and electroluminescent devices. This chapter will not go into depth in the material of interest, namely, GeSe. However, the physics surrounding it will be discussed, and the material properties as well as the crystal structure will be discussed in chapter 4 section 4.1.

The structural composition of this chapter consist of a brief introduction in condensed matter physics regarding bulk structures as well as some implementations towards two-dimensional structures, explained in section 2.1. Here we will go into the physics of crystal structure and the importance of momentum space, as well as density of states in both bulk and two dimensions. Lastly, one will discuss the importance in electronic band structure and electron occupancy. Furthermore, electrical transport in semiconductors is of high value when researching condensed matter physics for application in electrical devices. In section 2.2 electrical conductivity and mobility is explained. When discussing two dimensional materials, one needs to understand the importance of quantum confinement as well as different scattering mechanism which is influenced by the diminished dimension. Brief explanation of multivalley semiconductors as well as the interlayer coupling present in two dimensional materials

is discussed. Interlayer coupling is of interest in two dimensional materials, as they consist of layers, whereas these layers interact in terms of Van der Waals forces. In section 2.3 we will briefly discuss the importance and use of envelope functions and the famous Dirac equation. As we enter the quantum realm and the electron velocity approaches the speed of light, one needs new methods for solving the Schrödinger equation. Furthermore, the implementation of envelope function is widely used throughout the scientific community to approximate the wavefunction in terms of imperfection of the crystal structure. In the last section 2.4 one will discuss and explain excitons in two dimensional structures. Where a further explanation of the electron band structure is discussed, and how electron-holes coupling is related to excitons. Furthermore, exciton binding energy and recombination mechanism is explained. Finally, an important introduction to spin-orbit coupling is presented.

2.1 Condensed matter physics in bulk structures

Condensed matter physics is a broad field of physics, here we will focus on the the crystal structure of materials, and the theory to explain and present crystal structure mathematically. Furthermore, in order to describe and explain the physics of condensed matter one converts real space into the reciprocal - momentum space. Ones momentum space is understood we work our way towards density of states, and this is a key concept of condensed matter physics, whereas it furthers our knowledge towards available energy states in a material. This section is based on the famous book "Introduction to solid state physics" by Kittel,C [10] and "Semiconductor Physics" [11]

2.1.1 Crystal structure & Momentum space

In condensed matter physics one often discuss solid crystaline materials. These solid materials possess a certain well defined crystal structure. This crystal structure is an important factor to take into account when determining electric, thermal, optical properties. It is possible to recreate the entire crystal by what is called a primitive unit cell. The mathematical formulation of such a cell is explained by the primitive lattice vectors, $\mathbf{a_1}, \mathbf{a_2}, \mathbf{a_3}$. Any vector in real space can be written as, $\mathbf{r} = u_1\mathbf{a_1} + u_2\mathbf{a_2} + u_3\mathbf{a_3}$, where (u_1, u_2, u_3) are real numbers, where $\mathbf{r}$ points to a specific point in real space. The primitive lattice vectors span the real space, creating the primitive unit cell, which is translated by translation symmetry across the crystal. There is no cell of smaller volume than, $\mathbf{a_1} \cdot \mathbf{a_2} \times \mathbf{a_3}$, that can be used as a building block of the crystal structure. It is convenient to create another vector determined by the same lattice vectors as $\mathbf{r}$:

$$\mathbf{r} = u_1\mathbf{a_1} + u_2\mathbf{a_2} + u_3\mathbf{a_3} \tag{2.1}$$

$$\mathbf{T} = n_1\mathbf{a_1} + n_2\mathbf{a_2} + n_3\mathbf{a_3} \tag{2.2}$$

In this case **T** is determined by integers (n_1, n_2, n_3). As an example, picture the simple cubic structure in figure 2.1. Since the primitive lattice vectors spans the real space, and thereby spans the simple cubic structure in our case. It is simple to see that if $n_1 = n_2 = n_3 = 0$, this would point to the origo. On the other hand, if n_1 had value one and the others value zero, the vector **T** would point to another atom. By this we could literally map all atoms in the crystal structure, this is an important tool to appreciate in condensed matter physics and becomes important when we touch upon momentum space when referring to crystal translation.

A unit cell is the smallest repeating unit in a crystal. If one where to take an example - Polonium - which has the crystal structure named simpel cubic. This is the easiest structure a material may possess, and Polonium is the only known material which possesses this structure. A simple cube where Polonium is places in each corner. This simple cubic structure is iterated throughout the crystal in all three dimensions (x, y, z) by the use of the primitive lattice vectors described above. One can therefore say that the unit cell of simple cubic structure has 1 atom in its unit cell, since each atom in the corner is shared among 8 other unit cells. Giving us $\#atoms = \frac{1}{8} \times 8$. In a simple cubic, depicted by figure 2.1 the primitive lattice vectors is:

$$\mathbf{a_1} = a\mathbf{x}, \qquad \mathbf{a_2} = a\mathbf{y} \qquad \mathbf{a_3} = a\mathbf{z} \tag{2.3}$$

Where $\mathbf{x}, \mathbf{y}, \mathbf{z}$ follows the Cartesian coordinate system, and a is the primitive lattice parameter,

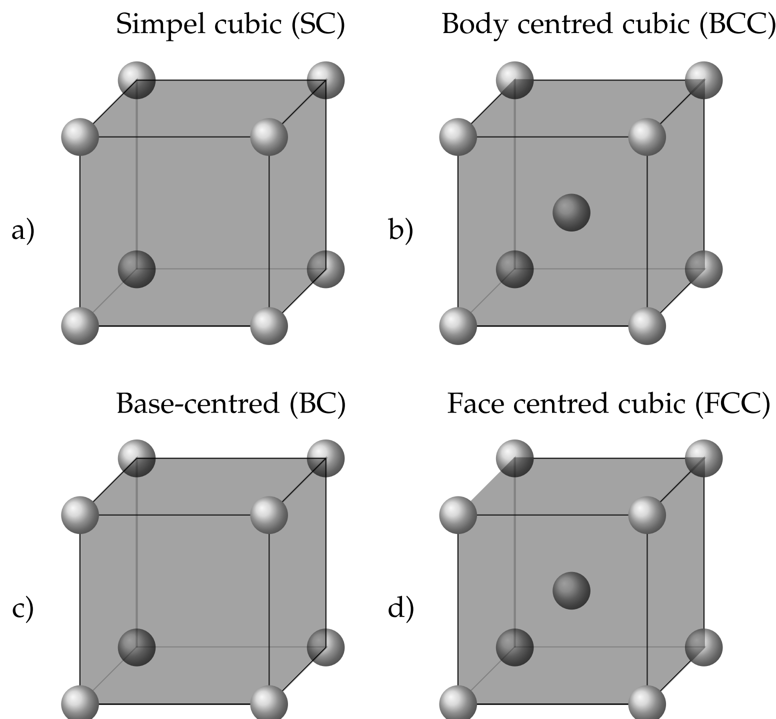

Figure 2.1: Illustration of Bravais lattices, simpel cubic, body centered cubic, base-centred cubic and face centred cubic

determining the length of vectors. Off-course, these primitive lattice vectors alters when the crystal structure differs from that of simple cubic.

One often finds one self directed towards momentum space also called **k**-space or reciprocal space, in condensed matter physics. A fairly simpel discussion about crystal structures and the use of primitive lattice vectors is the basis for tackling the use and meaning of momentum space. However there is one more thing to look at before we go into details, and that is crystal momentum itself. In short, momentum space is just converting real space to the reciprocal space named momentum space to make things much simpler when working with condensed matter physics. Especially when talking about electrons and holes, one need a proper way to describe the wavefunctions.

Schr*ö*dinger (S.H) equation is an equation widely used throughout quantum mechanics and other disciplines. It is a way to determine the eigenvalues of a certain eigenfunction, where a wavefunction typically is the eigenfunction. Also there is an operator operating on the wavefunction, $\mathscr{H}$ is the Hamiltonian operator, which is written as $\mathscr{H} = \frac{\hat{\mathbf{p}}^2}{2m_e} + V(\mathbf{r})$ which is the sum over kinetic and potential energies of the system. Where $\hat{\mathbf{p}}$ is the momentum operator written in quantum mechanics as: $\hat{\mathbf{p}} = -i\hbar\nabla_{\mathbf{r}}$. The wavefunction $\psi_{\mathbf{k}}(\mathbf{r})$ may in the simplest case be written as a traveling plane wave:

$$\psi_{\mathbf{k}}(\mathbf{r}) = e^{i(\mathbf{k}\cdot\mathbf{r}-\omega t)} \tag{2.4}$$

This is just a plane wave traveling in one direction. Whereas **k** is the wavevector and k is the magnitude of that vector called wavenumber ($|\mathbf{k}| = k = 2\pi/\lambda$). Here we have introduced the first take on reciprocal space. As one can see the wavenumber is the reciprocal of real space. Further on we have the S.H equation for a singel electron where we neglect the potential $V(\mathbf{r})$ acting in the crystal.

$$\mathscr{H}\psi_{\mathbf{k}}(\mathbf{r}) = \epsilon_{\mathbf{k}}\psi_{\mathbf{k}}(\mathbf{r}) \tag{2.5}$$

We know that the hamiltionan operates on the wavefunction. Giving us the corresponding energy eigenvalue:

$$-\frac{\hbar^2}{2m_e}\nabla_{\mathbf{r}}e^{i(\mathbf{k}\cdot\mathbf{r}-\omega t)} = \epsilon_{\mathbf{k}}e^{i(\mathbf{k}\cdot\mathbf{r}-\omega t)}$$

$$\epsilon_{\mathbf{k}} = \frac{\hbar^2\mathbf{k}^2}{2m_e} \tag{2.6}$$

This is called the energy dispersion relation for free electron fermi-gas (FEFG). The same goes for the momentum operator. One can simple let the momentum operator act on the wavefunction - where $\hat{\mathbf{p}} = -i\hbar\nabla_{\mathbf{r}}$, giving us the eigenvalue of the momentum to be $\mathbf{p} = \hbar\mathbf{k}$,

however this is not the crystal momentum. In order to introduce the crystal momentum one needs to take into account the periodicity of the crystal. Our wavefunction becomes a bit more complicated, because we are now looking at an electron wavefunction perturbed by the periodicity of the crystal. We usually depict the wavefunction as a Bloch function.

$$\psi_{\mathbf{k}}(\mathbf{r}) = e^{i\mathbf{k}\cdot\mathbf{r}} u_{\mathbf{k}}(\mathbf{r}) \tag{2.7}$$

Where the function $u_{\mathbf{k}}(\mathbf{r})$ is the part that contains the periodicity of the crystal structure.

$$u_{\mathbf{k}}(\mathbf{r}) = \sum_{\mathbf{G}} u_{\mathbf{k}+\mathbf{G}} e^{i\mathbf{G}\cdot\mathbf{r}} \tag{2.8}$$

Here we have to introduce a new vector, namely $\mathbf{G}$, this is in analogy to the translation vector derived earlier $\mathbf{T}$, however, this vector is in reciprocal space. The close definition and value will be explained shortly. We can now arrive at the proper crystal momentum:

$$-i\hbar\nabla_{\mathbf{r}}\psi_{\mathbf{k}}(\mathbf{r}) = \mathbf{p}\psi_{\mathbf{k}}(\mathbf{r}) \tag{2.9}$$

Simply inserting for the Bloch periodicity in the wavefunction.

$$-i\hbar\nabla_{\mathbf{r}} \sum_{\mathbf{G}} u_{\mathbf{k}+\mathbf{G}} e^{i(\mathbf{k}+\mathbf{G})\cdot\mathbf{r}} = \mathbf{p} \sum_{\mathbf{G}} u_{\mathbf{k}+\mathbf{G}} e^{i(\mathbf{k}+\mathbf{G})\cdot\mathbf{r}} \tag{2.10}$$

We then arrive to the proper depicted crystal momentum:

$$\mathbf{p} = \hbar(\mathbf{k} + \mathbf{G}) \tag{2.11}$$

It is now due time for an explanation for what momentum space is. We go by in the same manner as we descibed real space, namely by introducing some primitive vectors which has the purpose of spanning the reciprocal space. We call these primitive reciprocal lattice vectors for ($\mathbf{b_1}, \mathbf{b_2}$ and $\mathbf{b_3}$), and we define them as such:

$$\mathbf{b_1} = 2\pi\frac{\mathbf{a_2}\times\mathbf{a_3}}{\mathbf{a_1}\cdot\mathbf{a_2}\times\mathbf{b_3}} \quad \mathbf{b_2} = 2\pi\frac{\mathbf{a_3}\times\mathbf{a_1}}{\mathbf{a_1}\cdot\mathbf{a_2}\times\mathbf{b_3}} \quad \mathbf{b_3} = 2\pi\frac{\mathbf{a_1}\times\mathbf{a_2}}{\mathbf{a_1}\cdot\mathbf{a_2}\times\mathbf{b_3}} \tag{2.12}$$

We can see by geometry that we use the primitive lattice vectors in order to describe the primitive reciprocal lattice vectors. We may now proceed to define $\mathbf{G} = m_1\mathbf{b_1} + m_2\mathbf{b_2} + m_3\mathbf{b_3}$, where m_1, m_2, m_3 are integers. One important property of the primitive reciprocal lattice vectors is:

$$\mathbf{b_i}\cdot\mathbf{a_j} = 2\pi\delta_{ij} \tag{2.13}$$

Where $\delta_{ij} = 1$ if i = j and $\delta_{ij} = 0$ if $i \neq j$. This is an important property which manifests itself throughout calculations. It shows that the potential of a perfect crystal is invariant under translation by a vector **T**- giving us $V(\mathbf{r}) = V(\mathbf{r} + \mathbf{T})$. This can be shown as:

$$V(\mathbf{r}) = \sum_{\mathbf{G}} V_{\mathbf{G}} e^{i\mathbf{G}\cdot\mathbf{r}} \tag{2.14}$$

$$V(\mathbf{r} + \mathbf{T}) = \sum_{\mathbf{G}} V_{\mathbf{G}} e^{i\mathbf{G}\cdot(\mathbf{r}+\mathbf{T})} = \sum_{\mathbf{G}} V_{\mathbf{G}} e^{i\mathbf{G}\cdot(\mathbf{r})} e^{i\mathbf{G}\cdot\mathbf{T}} = V(\mathbf{r}) \tag{2.15}$$

This result important yet obvious, since the crystal is periodic one would expect the potential to be periodic. Shifting the potential by a translation vector **T** simply reproduces the potential, this implies for the periodic Bloch part as well, $u_{\mathbf{k}}(\mathbf{r}) = u_{\mathbf{k}}(\mathbf{r} + \mathbf{T})$, due to equation 2.13 - important to note that this is for a perfect crystal and we are off course neglecting certain impurities such as defects.

2.1.2 Density of States from 3D to 2D samples

Density of states (DoS) is an important value of materials. The energy eigenvalue for a free electron mentioned in subsection 2.1.1, may indeed occupy various energy levels, often one add an index n ($\epsilon_{n\mathbf{k}}$) - called band index. This subscript determines the energy level the electron is at, the reader is encouraged to read "particle in a box in one dimension", for further description. The main thing to know is that to completely describe an electron, four quantum numbers is needed: energy (n), angular momentum ($\mathscr{L}$), magnetic moment ($m_{\mathscr{L}}$), and spin (m_s). Whereas the quantum number (n = 1,2,3 ...), determines at which energy level the electron is at, and it is not possible for more than two electron to occupy the same energy level, orbital or electron wavefunction. This is indeed due to Pauli exclusion principle, which states that two fermions can not have identical quantum numbers or energies. Therefore, if we consider $1s^2$ orbital in Helium, there are two electrons in the first orbital. However these electron do not have the same quantum number, because they have opposite spin $m_s = [\frac{1}{2}, -\frac{1}{2}]$, typically denoted in Bra-Ket notation as: $\psi_+ = |+\rangle$ and $\psi_- = |-\rangle$.

We may yet again direct our attention towards the electron wavefunction $\psi_{n\mathbf{k}}(\mathbf{r})$. However this time we need to take into account that the crystal structure is limited in all three dimensions. In order to incorporate this into our wavefunction we need to establish a boundary condition. We define a new vector called $\mathbf{L} = N\mathbf{a_1} + N\mathbf{a_2} + N\mathbf{a_3}$, where N is number of atoms and $L_x = Na$, gives us the length of the crystal in a given direction. The boundary condition reads:

$$\psi_{n\mathbf{k}}(\mathbf{r}) = \psi_{n\mathbf{k}}(\mathbf{r} + \mathbf{L}) \tag{2.16}$$

We know from subsection 2.1.1 that $e^{i\mathbf{k}\cdot\mathbf{L}} = 1$ in order for the translation to be valid and that the Bloch wavefunction needs to be invariant under translation. As we saw previously the Bloch part $u_{\mathbf{k}}$ is invariant under translation by **T**, it will therefore be invariant under translation by the vector **L**. This puts a restrain on our wavevector **k**. We may now define **k**-values as a consequence of the periodic boundary condition applied:

$$\mathbf{k} = \frac{2\pi n}{\mathbf{L}} \qquad n = \pm 0, \pm 1, \pm 2, \pm 3 \ldots \frac{N}{2} \tag{2.17}$$

This gives us a discrete set of **k**-values. All other values of **k** is invalid and will destroy the wavefunction in the applied boundary condition. Furthermore if we remember equation 2.6, we figured out the energy dispersion relation for FEFG, and one can clearly see that this energy is dependent of the wavevector. We showed above that the wavevector is indeed discrete when boundary condition is applied to the wavefunction. This implies that the energy is discrete as well. Another important fact to recognise is that the maximum value of **k** is $\mathbf{k}_{max} = \frac{\pi}{a}$. This is an interesting result, that shows importance of Brillouin zones and wave diffractions in a crystal. We know from before in subsection 2.1.1 that the reciprocal lattice vector **G** spans the reciprocal space. We now introduce the diffraction condition in reciprocal space:

$$\mathbf{k} \cdot \left(\frac{1}{2}\mathbf{G}\right) = \left(\frac{1}{2}G\right)^2 \tag{2.18}$$

Some algebra gives us the following condition:

$$k_G = \frac{1}{2}|\mathbf{G}| \tag{2.19}$$

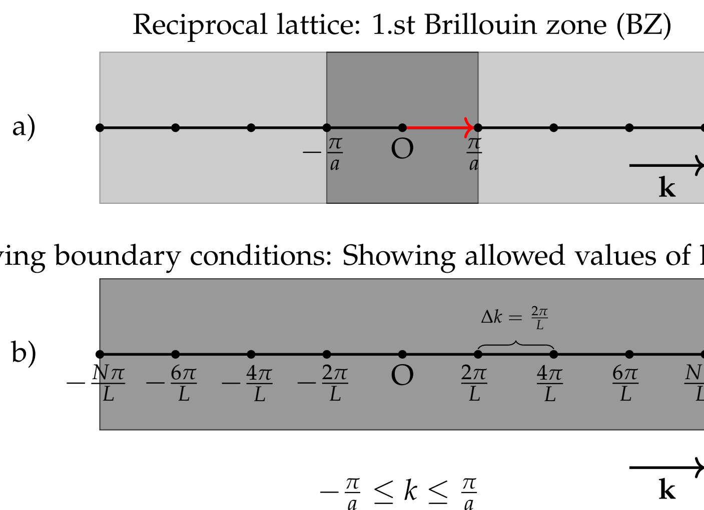

Figure 2.2: a) Reciprocal lattice in one dimension, showing the 1.st Brillouin zone (BZ) in the darker grey region. b) illustration of allowed **k**-values inside the 1.st BZ. The letter O stands for origo.

Where k_G is $|\mathbf{k}|cos(\theta)$. This is what defines the Brillouin zone in the reciprocal space, it is a consequence of the diffraction condition. In analogy to the Brillouin zone, it is somewhat useful to compare it with the Wigner-Seitz cell in real space. In figure 2.2, there is a schematic representation of the 1.st Brillouin zone in a one dimensional crystal.

In figure 2.2 a), the dark grey region represent the first BZ and shows the lengt of the reciprocal lattice vector as $\frac{1}{2}|\mathbf{G}|$. Furthermore, in figure 2.2 b) the 1.st BZ is zoomed in showing allowed states in **k**-space, due to boundary condition.

The definition of density of states is number of states/orbitals per unit volume. There is a simple mathematical representation of this interperiated in three dimensions:

$$D_{3D}(\epsilon_{n\mathbf{k}}) = \frac{dN}{d\epsilon_{n\mathbf{k}}} \tag{2.20}$$

Firstly we need to find the total number of states N. An easy way of doing that is to create a sphere with radius k_F. The magnitude of k_F points to the fermi surface of the sphere - and this is the fermi-energy. There is also two allowed states within a volume element $(2\pi/L)^3$, due to Pauli exclusion principle.

$$N = 2 \times \frac{4\pi {k_F}^3/3}{(2\pi/L)^3} = \frac{V}{3\pi^2}{k_F}^3 \tag{2.21}$$

Using our previously calculated results for the energy dispersion relation for FEFG, and insert for k_F in equation 2.21 we end up with the density of states in a three dimensional sample following FEFG:

$$D_{3D}(\epsilon_{n\mathbf{k}}) = \frac{1}{2\pi^2}\left(\frac{2m_e}{\hbar^2}\right)^{3/2} \epsilon_{n\mathbf{k}}^{1/2} \tag{2.22}$$

Which shows that the density of states in 3D is proportional to $\epsilon_{n\mathbf{k}}^{1/2}$.

We have yet spoken about temperature-dependency. If the system is at the lowest energy possibly we say that it is in ground state, and this is possible at zero kelvin. However, in order to incorporate an analysis of how the system is perturbed under the influence of temperature, we introduce Fermi-Dirac distribution. Fermi-Dirac distribution gives the probability that an orbital/state at energy $\epsilon_{n\mathbf{k}}$ will be occupied in thermal equilibrium:

$$f(\epsilon_{n\mathbf{k}}, T) = \frac{1}{e^{(\epsilon_{n\mathbf{k}}-\mu)/k_BT} + 1} \tag{2.23}$$

Where k_B is Boltzmann constant and μ is the chemical potential. At zero kelvin, $\mu = \epsilon_F$ and the Fermi-Dirac distribution is a step-function around $\epsilon_{n\mathbf{k}}$, by this we see that all states below Fermi energy ϵ_F is occupied while all states with energies greater than ϵ_F is unoccupied

(zero probability). However at greater temperatures this probability changes, and there is a likelihood that energies above ϵ_F is occupied. This is mainly due to thermal energy given by $k_B T$, as this energy is increasing the probability that an electron is excited to another energy level is increased.

Electrons occupy the valence band and conduction band in a semiconductor. The electron density in a band is obtained by integrating over the spectral electron density n(E), i.e. the density of electrons in the interval [E, E + dE]. The spectral electron density is given by the spectral density of electronic states $D(E)$ available, multiplied by their occupation probability. Furthermore at zero kelvin the conduction band is empty according to the fermi-dirac function and that the fermi level resides within the bandgap in a semiconductor. The electron density in a band is given by:

$$n = \int_{E_{bottom}}^{E_{top}} n(\epsilon_{n\mathbf{k}}) d\epsilon_{n\mathbf{k}} = \int_{E_{bottom}}^{E_{top}} D(\epsilon_{n\mathbf{k}}) f(\epsilon_{n\mathbf{k}}, T) d\epsilon_{n\mathbf{k}} \tag{2.24}$$

In order to appreciate these results in comparison to two dimensional samples. The density of states is basically determined the same way, except we confine our self to two dimensions, giving us the total number of states:

$$N = 2 \times \frac{\pi {k_F}^2}{(2\pi/L)^2} = \frac{L^2 {k_F}^2}{2\pi} \tag{2.25}$$

Once again, we need to account for electron spin. Here we create a circle with radius k_F, and find out how many states there is per possible state $(2\pi/L)^2$

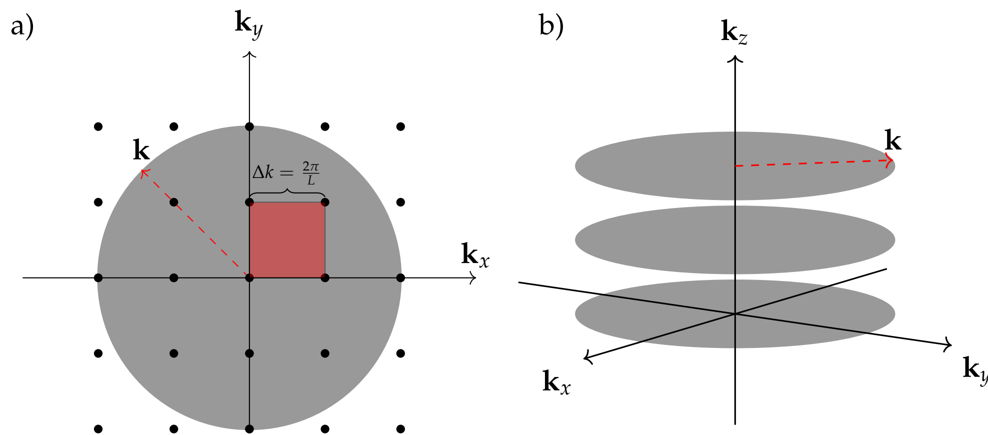

Figure 2.3: Illustration of Density of States in 2D. a) showing available states within the two dimensional plane. b) If we are in a quasi-two dimensional state the restriction of k_z-values are incorporated

We can now solve for density of states in a two dimensional system using equation 2.20 in the similar manner as previously:

$$D_{2D}(\epsilon_{n\mathbf{k}}) = \frac{m_e}{\hbar^2 \pi} \tag{2.26}$$

As we can see, the wavevector falls and those where the only one containing $\epsilon_{n\mathbf{k}}$, and by that the density of states in 2D is independent of energy. If we further our investigation, we find that the density of states in 2D is in fact a step-function in real life. As we compress one dimension we get large values in **k**-space. So we still have 3D, but in fragments sort of. The areas created also move in the 3rd dimension, but with large spacing, this is what gives rise to the step-function. Figure 2.3 a,b) is not correctly scaled of course. But it gives an overview, that the area we created during D_{2D} calculation are indeed also in 3D with discreet values in k_z. The planes comes further apart as the dimension is reduced.

In this two dimensional model we have a finite confinement in one direction. This leads to discrete values as illustrated in figure 2.3b), which again lead to a step-function in D_{2D}. As we saw for 3D case, the density of states varies with $\epsilon^{1/2}$.

For the 2D case in we find that the electrons can move about in the x-y plane approximate to that in bulk and dispersion relation can be written as:

$$\epsilon_n(k_x, k_y) = \epsilon_{n,z} + \frac{\hbar^2(k_x^2 + k_y^2)}{2m_e} \tag{2.27}$$

A more general way of formulating this equation would be to incorporate the so called electron effective mass and the overlapping of directions, through a summation.

$$\epsilon_n(\mathbf{k}) = \epsilon_{n,z} + \frac{\hbar^2}{2} \sum_{\alpha,\beta} \frac{\mathbf{k}_\alpha \mathbf{k}_\beta}{m^*_{e(\alpha,\beta)}} \tag{2.28}$$

Where $\epsilon_{n,z}$ is the quantized bound state energies and α, β are the x and y direction, the effective mass will be explained fairly soon. So by this we can see that the Density of state as we calculated earlier is in fact:

$$D_{2D}(\epsilon_{n\mathbf{k}}) = \frac{m_e}{\hbar^2 \pi} \sum_n \Theta(\epsilon_{\mathbf{k}} - \epsilon_{n\mathbf{k}}) \tag{2.29}$$

Changes as we increase the band index n, where $\Theta(\epsilon_{\mathbf{k}} - \epsilon_{n\mathbf{k}})$ is a Heaviside step function. So $D_{2D} = 0$ until the first bound state is reached, then it increases with $\frac{m_e}{\hbar^2 \pi}$ and so on. We can also look at L_z dependency since it is this dimension we are confining.

$$D_{2D}(\epsilon_{n\mathbf{k}}) = \frac{m_e}{\hbar^2 \pi} \frac{1}{L_z} \tag{2.30}$$

So with larger values of L_z - increasing dimension- gives us an increasingly overlap with the bulk case. Since the steps in the step-function are decreasing and the values comes closer to the 3D case. So by increasing L_z we enter the three dimensional case, and the discreteness vanishes.

We now further our interest toward Electronic band structure & electron occupancy in light of semiconductors.

2.1.3 Electronic Band Structure & Electron Occupation

In this thesis we are working with semiconductors, a neat but powerful definition of a semiconductor is that the bandgap is at intermediate value compared to metals and insulators. The bandgap has a satisfying value which serves as an important fact for electronic devices. Will come back to this later on. As briefly touched upon in subsection 2.1.2 a semiconductor has a valence and conduction band. The region separating these bands is called the bandgap. The valence band is in the lower energy region and the conduction band is in the higher energy region. In a metal the "free" electron is in the conduction band - or there is only one electron in the outer orbital. This electron would then be semi-free to conduct electricity, yielding the high conductivity for metals.

So far we have looked at free electron fermi gas, and have purposely neglected the potential acting on the electrons in a crystal. If we are to consider the band structure of a crystal the potential needs to be incorporated in to our model.

The nearly free electron model starts from a free electron gas and treats a weak periodic crystal potential within perturbation theory [1]. Here, the bandgap emerge from interferences of the electronic waves that get scattered from the crystal potential, which results in standing waves at the edges of the Brillouin zones. These edges is often referred to as special symmetry points the Brillouin zone.

$$\epsilon_{n\mathbf{k}} = \frac{\hbar^2 \mathbf{k}^2}{2m_e^*} \tag{2.31}$$

Here we have incorporated the so-called electron effective mass, which is needed in semiconductors, the effective mass is a second order tensor in three dimensions, and it effects the mass of electrons and holes. As one is studying the bandstructure of semiconductors, electrons and holes effective masses are influenced by the curvature of this bandstructure, it is therefor necessary to implement the effective masses into our equations. Further information about effective masses is shown in Appendix A. Due to periodicity the electron

[1]Pertubation theory refers to an approximation of the model due to some abnormalities. These abnormalities may just as well be impurities or other types of defects such as vacancies, grain boundary etc. These abnormalities breaks the periodic symmetry of the crystal

energy is repeated throughout reciprocal space with interval of $\frac{2\pi}{a}$. The band crossing that occur at $k = \pm\frac{\pi}{a}$, is highly relevant. At these points, bragg's reflection is fulfilled. $(\mathbf{k}+\mathbf{G})^2 = k^2 \rightarrow k = \pm\frac{1}{2}\mathbf{G} = \frac{\pi n}{a}$. At these brillouin zone edges the propagating waves are interfering in such a manner that a standing wave is formed and consequently a bandgap emerges, as can be seen from figure 2.4c), where the bandgap is illustrated by the filled red regions. Furthermore one can look at this picture with ease, and say that the first band (band index n = 1) comes from $1s^2$ orbitals, which means it is full, also it has the quantum number $n = 1$, the second band (band index n = 2) may as well be $2s^2$ orbital serving the quantum number $n = 2$, and the third band (band index n = 3) may then be $2p^6$ orbitals having quantum number $n = 2$ as well. These last two bands differs in energy even though they have the same quantum number n, where angular momentum, magnetic moment, and spin all contribute to the total energy of the system.

When talking about semiconductors the typical bandgap value is below 4eV, anything above this value is classified as an insulator. In the valence band there are a high population of

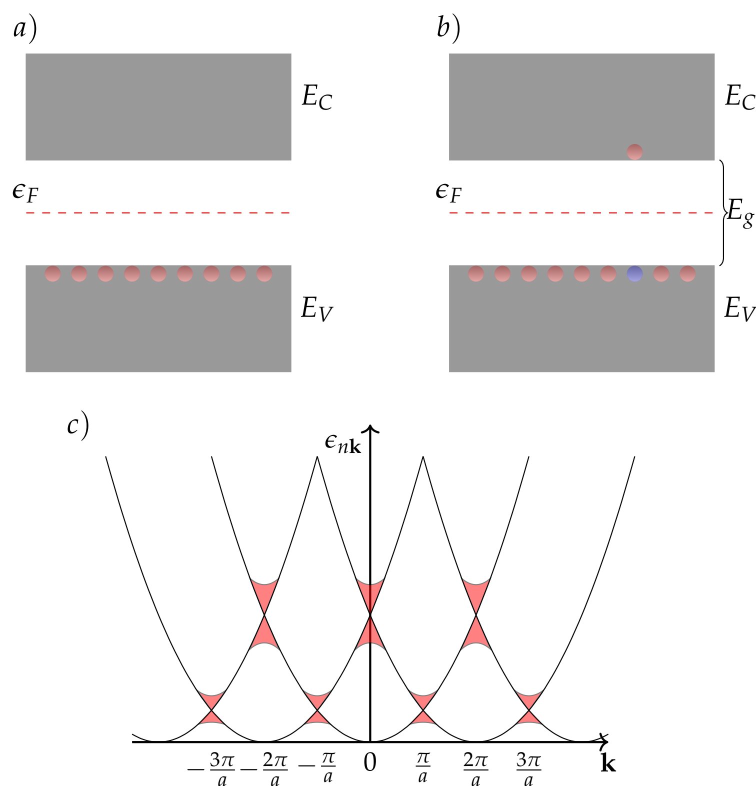

Figure 2.4: a,b) Intrinsic semiconductors with T = 0K and $\mu = \epsilon_F$. a) Illustration of intrinsic semiconductor with valence E_V and conduction E_C band, fermi level E_F, consequently in the middle. b) An electron is excited to the conduction band, leaving behind a hole illustrated as a blue ball. This excitation is demanding an energy of E_g, and can only take place if the electron receives this amount, either through phonons or photons etc. c) Illustration of nearly free electron model, where high symmetri points $\frac{n\pi}{a}$ gives standing waves due to interference and a bandgap emerges, where $[-\frac{\pi}{a}, \frac{\pi}{a}]$ defines the 1.st Brillouin zone. The filled red regions illustrates the bandgap.

electrons, which is possible to calculate using equation 2.24, with well defined boundaries. The concentration of electrons in the conduction band may be expressed as:

$$n_e = \int_{E_C}^{\infty} D_d(\epsilon_{n\mathbf{k}}) f(\epsilon_{n\mathbf{k}}, T) d\epsilon_{n\mathbf{k}} \tag{2.32}$$

Equivalently the hole concentration in the valence band may be expressed as:

$$p_h = \int_{\infty}^{E_V} D_d(\epsilon_{n\mathbf{k}}) \left[1 - f(\epsilon_{n\mathbf{k}}, T)\right] d\epsilon_{n\mathbf{k}} \tag{2.33}$$

Where p_h is the hole concentration in the valence band and the subscript d indicates dimensions $d = 1, 2, 3$. Here, we need to consider the effective hole mass in the density of states, which may be abbreviated as m_p^*.

Let us look at intrinsic carrier concentrations in semiconductors as illustrated by figure 2.4a,b). Semiconductors which is free of impurities and other defects, is called intrinsic, and the equations 2.32,2.33 are appropriate means to calculate the concentrations. In these types of semiconductors, the carriers are provided due to thermal excitation. The thermal energy may be expressed as; $\epsilon_T = k_b T$, if this thermal energy is in the range of the bandgap, E_g, the the thermal energy is sufficient to excite electrons up to the conduction band, this can also be seen through the fermi-dirac distribution. Where, higher temperature smears out the fermi-dirac distribution, and thereby increasing the probability that an electron occupy another state.

Interestingly, the number of $\mathbf{k}$-states in the 1.st Brillouin zone is equal to the number of primitive unit cells, N, in a given volume of L_x, L_y, L_z. Due to the nature of electrons they still behave according to Pauli exclusion principle, and thereby two electrons can be in one distinct $\mathbf{k}$-state yielding 2N independent orbitals/$\mathbf{k}$-states in each energy band.

In the next section electrical transport in two dimensional materials will be analysed, where one need to consider the different boundary conditions that comes into account. Mesoscopic systems will be of importance when discussing two dimensional materials, where the effect of small dimensions in on direction prohibits motion of electrons and phonons causing various phenomena.

2.2 Electrical transport in Two dimensional materials

This section aims to give an explanation of the basic electronic transport in semiconductors as well as two dimensional semiconductors. Furthermore, the importance of quantum confinement and the change in various scattering mechanisms is explained. Where we discuss the mean free path of electrons and the influence of diminished dimension, and electron-electron interactions. This

section is based on the books "Mesoscopic electronics in solid state nanostructures", "Transport in nanostructures"[12, 13] and "Introduction to solid state physics" by Kittel,C [10].

2.2.1 Electrical conductivity & mobility

Two dimensional materials possess some special attributes due to its two-dimensional nature. Strictly speaking we confine ourself in the x,y-plane, however, most materials do extend in the third dimension. These are not exactly two dimensional, but quasi-two dimensional. We will use these terms quite interchangeably, but it will be stated otherwise if needed. In these systems there are profoundly more interesting substance to cover in the quantum confinement of two dimensional materials. In order to give an overview of the electrical properties of two dimensional materials we will confine ourself to carrier transport parallel to the confining potential, that is the non-reduced x,y-plane. By this we may treat the material in the same manner as homogeneous transport in bulk system in terms of conductivity and mobility. Various scattering events as a consequence of the lower dimensionalities will be discussed in a subsequent section.

We now proceed to inventigate carrier mobilities and conductivity. We may start with a classical approach, namely Newtons second law. $F = m \cdot d\mathbf{v}_{||}/dt$, where we here are considering the force upon an electron in an electrical field $\boldsymbol{\xi}_{||}$, all subsequent vectors will be in the non-confined spacial plane, if otherwise, it will be stated. In order to accommodate the electric field we may rewrite Newtons second law in terms of Lorentz force as follows:

$$m_e^* \frac{d\mathbf{v}}{dt} = -e\left(\boldsymbol{\xi} + e\frac{\mathbf{v}}{c} \times \mathbf{B}\right) \tag{2.34}$$

To get an overview over the velocity of carrier electrons in a semiconductor we need to address the so-called group velocity. The group velocity is defined as such:

$$v_g = \frac{\partial \omega(\mathbf{K})}{\partial \mathbf{K}} \tag{2.35}$$

Where $\omega(\mathbf{K})$ is the dispersion relation for phonons, and $\mathbf{K}$ is the corresponding wavevector. Further on if we use the definition that $\epsilon_{n\mathbf{k}} = \hbar\omega$, we may substitute for $\omega(\mathbf{K})$ and get the group velocity for electrons:

$$\mathbf{v}_n(\mathbf{k}) = \frac{1}{\hbar}\nabla_{\mathbf{k}}\epsilon_{n\mathbf{k}} \tag{2.36}$$

Where we now have calculated the group velocity of electrons in a subsequent band indexed by n. As we can see, the velocity is determined by the change in the dispersion relation. We can now determine the velocities at the dispersion relation extrema. This gives us:

$$\mathbf{v}_n(\mathbf{k}) = \frac{1}{\hbar}\nabla_{\mathbf{k}}\epsilon_{n\mathbf{k}}|_{\mathbf{k}=0} = 0 \tag{2.37}$$

The velocities of electrons is indeed affected by the effective mass of the electron. We once again refer to appendix A for further reading on effective mass. We circle back to equation 2.34 and assumes that the magnetic field is zero $\rightarrow \mathbf{B} = 0$, we then end up with:

$$m_e^* \frac{d\mathbf{v}}{dt} = -e\boldsymbol{\xi} \tag{2.38}$$

Instead of implementing our definition of the electron velocity in this equation we would rather set $m_e^*\mathbf{v} = \hbar\mathbf{k}$, and look at how $\mathbf{k}$-space changes with applied electric field. We may now understand that, once the momentum space shifts in a direction, it directly effects the motion of electron, this will become clear in a moment. If we further the discussion of equation 2.38, and solve for the velocity we find:

$$\mathbf{v} = -\frac{e\boldsymbol{\xi}\tau}{m_e^*} \tag{2.39}$$

As we discussed, briefly, the momentum space is shifted incrementally when as force is exerted upon it, in this case an electric field. Here we have arrived to an expression of the velocity of this incrementally shift of momentum space which is also called the *drift velocity*. We consider the time between successive scattering events of electron to be τ, it is basically the average time between each electron collision. We are then considering the shift in momentum space to be defined from this mean free time of electron scattering events. Quick rearrangement of equation 2.39 with $m_e^*\mathbf{v} = \hbar\mathbf{k}$, we get that the infidesimal change in momentum space is $\delta\mathbf{k} = -e\boldsymbol{\xi}/\hbar$. The electric current density is now possible to work out. We start by considering the number of electron per unit volume in a constant electric field $\boldsymbol{\xi}$ and that each electron has charge $-e$, we get:

$$\mathbf{J} = -en_{2D}\mathbf{v}$$

Substituting for the incremental electron velocity in the momentum space shift we get:

$$\sigma = \frac{e^2 n_{2D}\tau}{m_e^*} \qquad\qquad \rho = \frac{m_e^*}{e^2 n_{2D}\tau} \tag{2.40}$$

We have now arrived to the electron conductivity and the reciprocal of that namely the electron resistivity, extracted from **Omh's law**, which is defined as $\mathbf{J} = \sigma\boldsymbol{\xi}$. By surprise we have already worked out the electron mobility at this point. If we redirect our attention towards equation 2.39, we define the electron mobility as $\mathbf{v} = \mu\boldsymbol{\xi}$, we then have:

$$\mu = -\frac{e\tau}{m_e^*} \tag{2.41}$$

The electron mobility tells how easily the electron is transported inside the material. As we can see, the electron mobility is as well affected by the electron effective mass, however we

are in this subsection limiting ourself to the non-confining plane. That means that we do not have the full second order tensor describing the electron effective mass. It is somewhat common to call the effective mass remaining in the two dimensional plane for transverse effective masses (m_e^*).

2.2.2 Quantum confinement & Scattering mechanisms

In order to get a comprehensive view of electronic transport in two dimensional systems, one first needs to be familiar with some important features. De Broglie wavelength of electrons (size quantization), Electronic mean free path (Ballistic transport), scattering events (electron-electron, electron-phonon). All these features determines the electronic transport in two dimensional systems.

de Broglie wavelength We may start with the first one which directly involves the diminished z-dimension. Fermi wavelength, this wavelength is defined as $\lambda_F = \frac{2\pi}{k_F}$, where k_F is the fermi **k**-vector used in equation 2.25. λ_F is also named de Broglie wavelength of the electrons at the Fermi edge. Size quantization may occur if the sample size orthonormal to the x,y-plane is comparable to the Fermi wavelength of the electrons. We have this condition: $L_z \leq \lambda_F$. We may further calculate the Fermi-wavelength, by applying k_F from equation 2.25, by using that the electron density is $n_{2D} = N/L^2$.

$$k_F^2 = 2\pi n_{2D} \tag{2.42}$$

$$\lambda_F = \frac{2\pi}{k_F} = \left(\frac{2\pi}{n_{2D}}\right)^{1/2}, \qquad \lambda_F = \frac{h}{p} = \frac{h}{\sqrt{2m_e^*\epsilon_{n\mathbf{k}}}} \tag{2.43}$$

Where we can see that the Fermi wavelength is inversely proportional with the square root of the electron density and also the momentum p. If one where to assume room-temperature and simplify by the use of thermal energy, the thermal energy would be $E = \frac{3}{2}kT = 26meV$ and an effective mass of one tenth the free electron mass, de Broglie wavelength would then be $\lambda_F = 10nm$. So if the statement $L_z \leq \lambda_F$ is for fulfilled one would expect some sort of quantization present[2]. If the wavelength of the electrons that carry the current is comparable to the size L_z the wave character becomes important and the kinetic energy of the electrons will be quantized as shown in figure 2.3. Where the diminished L_z-direction unfolds a quantization in $\mathbf{k}_z$. There is however one more criterion which needs to be fulfilled before one gets this effects, and that is the so-called mean free path of electrons.

[2]This does, however, not give a quantization of different phenomena such as quantum Hall effect when a magnetic field is applied perpendicular to the x,y-plane.

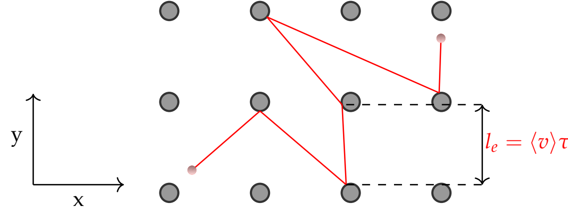

Figure 2.5: Illustration of electron mean free path in a perfect crystal, showing trajectories after scattering events. Grey and red circles illustrate, ions and electron respectively.

Electron mean free path

As we know, electrons travel through the material if either a metal or semiconductor. We are expecting that the electrons collide after some length l_e. This length scale is called mean free path, and is roughly speaking the average length an electron travels before getting scattered as shown in figure 2.5. We talked about the mean free time in the previous subsection, and this will come into mind shortly. If this length scale (l_e) is comparable to the device length - L_z in our case, we have fulfilled the criterion $L_z \leq l_e$. This gives rise to what is called Ballistic regime. This would in, theory, suggest that the electron may travel without scattering events, and we should expect lossless transportation - meaning we would expect superconducting behaviour. This is unfortunately not the reality, we cannot transport electrons across a ballistic regime without resistance. We are once again experiencing quantization of electrical transport. If one where to consider the extrinsic property of conductance, one sees that the quantization is represented in multiple integer values of $\frac{e^2}{\pi\hbar}$. Further-on if we where to look at the mean free path through the consideration of expectation value of velocity for electrons. We would firstly need to consider the velocity through the momentum $\mathbf{p}$:

$$\mathbf{v} = \frac{\mathbf{p}}{m_e^*} \tag{2.44}$$

We have previously introduced the momentum operator $\hat{\mathbf{p}} = -i\hbar\nabla_{\mathbf{r}}$, if we then were to look at the expectation value of velocity and introduce the fact that mean free path is calculated as $l_e = \langle \mathbf{v} \rangle \tau$ we get [3]:

$$\langle \mathbf{v} \rangle = \frac{\langle \mathbf{p} \rangle}{m_e^*} = \frac{1}{m_e^*}\langle \psi | \hat{\mathbf{p}} | \psi \rangle = -\frac{i\hbar}{m_e^*} \int \psi_{\mathbf{k}}(\mathbf{r})^* \nabla_{\mathbf{r}} \psi_{\mathbf{k}}(\mathbf{r}) d\mathbf{r} \tag{2.45}$$

$$l_e = \langle \mathbf{v} \rangle \tau = -\frac{i\hbar\tau}{m_e^*} \int \psi_{\mathbf{k}}(\mathbf{r})^* \nabla_{\mathbf{r}} \psi_{\mathbf{k}}(\mathbf{r}) d\mathbf{r} \tag{2.46}$$

[3] It is fully possible to calculate the expectation value of velocity without the momentum operator $\hat{\mathbf{p}} = -i\hbar\nabla_{\mathbf{r}}$, one would then need to translate the wavefunctions into momentum space by the use of Fourier transform - $\theta(\mathbf{p}) = \frac{1}{\sqrt{2\pi\hbar}} \int_{-\infty}^{\infty} e^{-i\mathbf{p}\cdot\mathbf{r}/\hbar} \psi_{\mathbf{k}}(\mathbf{r}) d\mathbf{r}$

This is off-course a simplified estimation of the mean free path for electrons, whereas the laws are altered once the mean free path is in the order of the device length L_z - where quantization effects enters. We will not go into more depth on this matter.

Electron-electron interactions

Regarding electron-electron interaction in terms of energy levels, and electron orbitals one need to incorporate conservation laws. Take figure 2.6a) as an example. Two electrons with wavevector $\mathbf{k_1}, \mathbf{k_2}$ are interacting and produces to subsequent electron wavevectors $\mathbf{k_3}, \mathbf{k_4}$. Momentum conservation law then tells us $\mathbf{k_1} + \mathbf{k_2} = \mathbf{k_3} + \mathbf{k_4}$, furthermore one may exhibit an elastic collision between these two electrons, which would furthermore conserve energy. In this elastic regime, there are limited options, given that no energy is lost, as well as gained during the interaction. As an example, let us consider electrons in the valence band. There are an accumulation of electrons in the occupied electron orbitals which forms the valence band. The only possible energy levels, or orbitals lies in the conduction band - as a consequence of the Pauli exclusion principle, electron-electron interaction does not cause any transition of energy levels, the electron-electron interaction is elastic.

Another case to consider is the inelastic scattering event, in this case, momentum is stil conserved while the energy is converted into heat, photon, lattice vibrations(phonons) and so forth. The famous physicist Richard Feynman[4], created the so-called Feynman diagram as shown in figure 2.6b) of electron-electron scattering named Møller scattering. This diagram shows the interaction between two fermions in which a photon is created during the interaction time. Where energy conservation in this system may be formulated as $\epsilon_1 + \epsilon_2 = \epsilon_3 + \epsilon_4 + \hbar\omega_{\mathbf{k}}$. The creation of a photon with energy $\hbar\omega_{\mathbf{k}}$, may be possible, if an incoming electron source with sufficient energy, excited an electron in the valence band

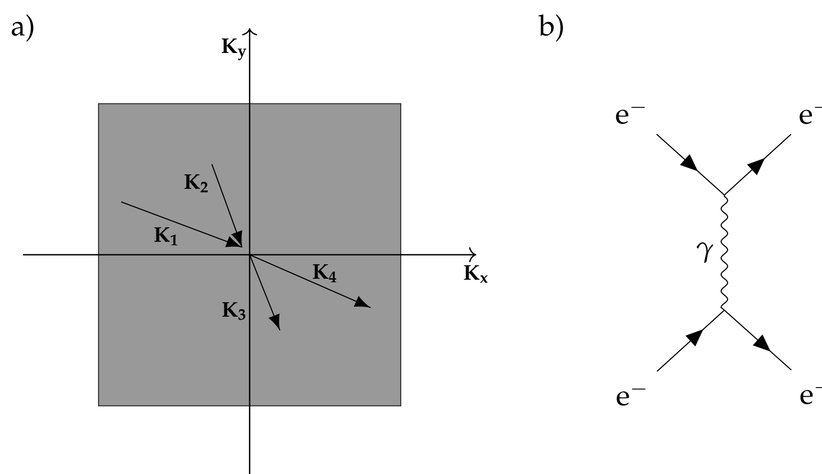

Figure 2.6: a) Electron-electron scattering resulting in two new wave vectors $\mathbf{k_3}, \mathbf{k_4}$ which needs to obey Pauli exclusion principle. b) Feynman diagram of electron-electron interaction, called møller scattering.

[4]Richard Feynman first introduced Feynman diagrams in 1949 in a Physical Review [14]

to the conduction band. The excited electron is then after a certain amount of time relaxed down to a lower energy state. The difference in energy may then produce a photon - typically in the range of the bandgap.

As we are working in quasi-two dimensional system, electron-electron scattering is rather unlikely in the diminished dimension, and if we where to consider the electron mean free path to be comparable to the device lengt L_z. The electron would simply scatter with the boundaries before colliding with an electron in som sense (If the electrons travels perpendicular to the two-dimensional plane, meaning, no x,y- component in the electron velocity vector).

Let us now briefly look at the electron-electron scattering rate through Fermi's Golden Rule. The Fermi's Golden Rule is used to define the scattering rates between different scattering events. It utilises quantum mechanics, and an unperturbed Hamiltonian is perturbed by a time-dependent term. This time dependent term translate or rotate the system frame in such a manner that we may consider the interaction to be "frozen" in time. An elongated process is needed order to reach the Fermi's Golden Rule, and it may be formulated as this for the electron-electron interaction.

$$\frac{1}{\tau_{|\mathbf{k}\rangle \to |\mathbf{k}'\rangle}} \approx \frac{2\pi}{\hbar} |\langle \mathbf{k}' | W_{ee} | \mathbf{k} \rangle|^2 \delta(\epsilon_{\mathbf{k}} - \epsilon_{\mathbf{k}'}) \tag{2.47}$$

Here we have a transition from $|\mathbf{k}\rangle \to |\mathbf{k}'\rangle$, and inside the square on the right-hand side is the so-called transition matrix element or scattering matrix element. As in the case for electron-electron interactions, the scattering matrix element comes from the screened Coulomb interactions as well as perturbation theory. The last factor is a delta-function, which in this case takes care of energy conservation. One, may convert this formulation of Fermi's Golden Rule to a more appropriate version by:

$$\frac{1}{\tau_{ee}} \approx \frac{2\pi}{\hbar} |V_q|^2 D_d(\epsilon_{\mathbf{k}}) n_e \tag{2.48}$$

Where $D_d(\epsilon_{\mathbf{k}})$ is the joint density of states, and in our case, we are looking at d = 2, meaning a constant density of state (as long as constant band index n). The only interference is the scattering matrix element itself as well as the energy range for which the electrons may interact. This is incorporated inside n_e from equation 2.32 as we discussed in section 2.1.3. The energy range in which electrons is capable of interaction, is in fact, given by the fermi-dirac distribution. Higher thermal energy yields a greater number of electron in which are capable of interaction. A rather crude estimate gives us that the number of electron in which are available is proportional to $\propto 1/T$

Electron-phonon interactions

In quasi-two dimensional system where the ballistic regime is working in the diminished direction, we also need to consider the in-plane electrons interaction with lattice vibrations. This is of interest due to the potential electron-phonon scattering effects. As we do not have any confinement in this plane we do indeed have electron-phonon scattering events. These scattering events cause a decreased mobility. As we may write the total mobility by the use of Matthiessen's rule:

$$\frac{1}{\mu_{tot}} = \frac{1}{\mu_{imp}} + \frac{1}{\mu_{lattice}} \tag{2.49}$$

Where the first term on the right-hand side is mobility in terms of impurity scattering. In figure 2.5 we showed a perfect crystal lattice, if one where to introduce impurities in an otherwise perfect lattice, the total mobility would indeed decrease as a consequence of decreased mean free path. The second term is scattering events such as electron-phonons interactions - called lattice scattering events. Phonons are described as the quanta of energy of a lattice vibration $\epsilon_{n\mathbf{k}} = (1/2 + n)\hbar\omega_{\mathbf{K}}$, where thermal energy is $\epsilon = k_b T$, $\hbar$ is the reduced Planck constant and $\omega_{\mathbf{K}}$ is the phonon mode dispersion relation between angular frequency and the wavenumber given by $\mathbf{K}$-values. As the carriers are confined in the in-plane, mobility is affected by the electron-phonon scattering time τ_{ep}, by $\mu_{ep} = -e\tau_{ep}/m^*_{||}$, where $m^*_{||}$ is the in-plane effective mass. Whereas the scattering time is manly influenced by occupation number as well as temperature - high temperature yields a lower scattering time which further reduces the mobility. At high temperatures, more phonons are excited [5] and may contribute in scattering events. Further-on, we may as previously, approximate the scattering rate by using the Fermi's Golden Rule:

$$\frac{1}{\tau_{|\mathbf{k}\rangle\rightarrow|\mathbf{k}'\rangle}} \approx \frac{2\pi}{\hbar}|\langle\mathbf{k}'|W_{ph}|\mathbf{k}\rangle|^2 \left[\underbrace{\delta(\epsilon_{\mathbf{k}} - \epsilon_{\mathbf{k}'} + \hbar\omega_{\mathbf{K}})}_{\text{absorption}} + \underbrace{\delta(\epsilon_{\mathbf{k}} - \epsilon_{\mathbf{k}'} - \hbar\omega_{\mathbf{K}})}_{\text{emission}}\right] \tag{2.50}$$

In contrary to electron-electron scattering rate, electron-phonon scattering rate is either dominated by absorption of an energy quanta of phonon $\epsilon_{\mathbf{k}'} = \epsilon_{\mathbf{k}} + \hbar\omega_{\mathbf{K}}$ or the emission $\epsilon_{\mathbf{k}'} = \epsilon_{\mathbf{k}} - \hbar\omega_{\mathbf{K}}$. Also, the scattering matrix element matrix is formulated according to the electron-phonon interaction. In the case of emission, the phonon energy is used to relax an electron after collision, reducing the energy of the electron by $\omega_{\mathbf{K}}$. Interestingly, elastic collision happens at so-called degenerate valleys. If symmetry allows it, there may be multiple valleys with states $|\mathbf{k}\rangle$ and $|\mathbf{k}'\rangle$ in which are close in energy- called degenerate states. An interaction between phonon and electron may then shift the electrons momentum, but conserve its energy, a type of valley transition would occur. On the other hand, inelastic collision occurs if states $|\mathbf{k}\rangle$ and $|\mathbf{k}'\rangle$, which are located at different position in $\mathbf{k}$-space, does

[5] According to Bose−Einstein statistics, phonons have a higher probability to be excited to a higher mode as temperature is increased. Bose-Einstein distribution is formulated as: $\langle n\rangle = \frac{1}{e^{\hbar\omega_{\mathbf{K}}/k_b T}+1}$

not have the same energy. Then, energy is not conserved and is transmitted in the form of light or other energy packages.

2.2.3 Multivalley semiconductors & interlayer coupling

In the previous subsection we briefly mentioned degenerate valleys in semiconductors. In order for degenerate valley to form, rotational symmetry about the z-axis needs to be present. Meaning, if a correct rotation about the z-axis is applied, one would simply reproduce the crystal structure - the crystal structure is invariant under certain rotation translations. Figure 2.7, shows degenerate valleys in a semiconductor with hexagonal structure. Whereas the hexagonal Brillouin zone shows a six-fold rotational translation about the z-axis. At the high-symmetry point K, K' we see the formation of conduction band and valence band. In this illustration they are at the same **k**-space, giving us a direct bandgap.

$$V\left(\mathbf{r}+\mathbf{T}_{\phi_6}\right)=\sum_{\mathbf{G}} V_{\mathbf{G}} e^{i\mathbf{G}\cdot\left(\mathbf{r}+\mathbf{T}_{\phi_6}\right)}=\sum_{\mathbf{G}} V_{\mathbf{G}} e^{i\mathbf{G}\cdot\mathbf{r}} e^{i\mathbf{G}\cdot\mathbf{T}_{\phi_6}}=V(\mathbf{r}) \tag{2.51}$$

We can see the invariance under translation here, where $\mathbf{T}_{\phi_6}$ is the six-fold translation matrix. The same yields for the periodic Bloch part; $u_{\mathbf{k}}(\mathbf{r})=u_{\mathbf{k}}\left(\mathbf{r}+\mathbf{T}_{\phi_6}\right)$.

As mentioned in subsection 2.2.2 electrons may scatter through electron-phonon interaction into a new degenerate valley by the transfer of momentum. Furthermore these electron transition events between successive valley may be traced and stored as information through Spin-Valley locking. So-called Valleytronics is a way of storing information in bits of 0 and 1 ($\uparrow$ and $\downarrow$). Each valley possesses a discrete **k**-space value and zeros and ones is stored in these discrete valleys. This is a possible way of manipulating multivalley semiconductors. We will not go further into this matter.

Two-dimensional material stems from original three dimensional structures. In bulk formation, the structure is layered. Each layer is separated by van der Waals (vdW) forces. If

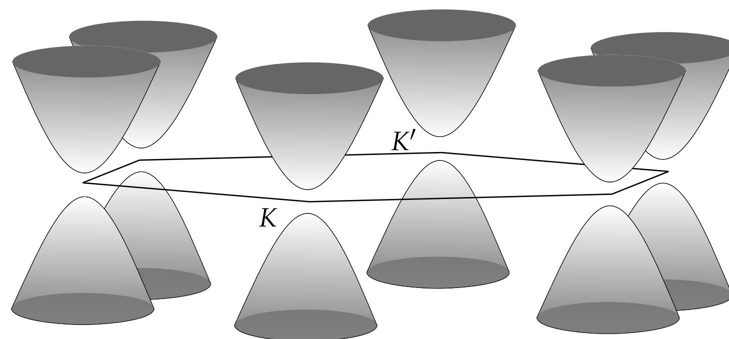

Figure 2.7: Valley degenerate states in a Hexagonal structure. Degenerate bands occurs in six-fold symmetry crystal structure. A direct bandgap is illustrated at the high symmetry points K, K'.

these forces are sufficiently weak, mechanical exfoliation is possible [6], where one separate layer by layer until desired thickness is achieved. Unique properties alters as one goes from bulk to two-dimensions. Some of these changes in property is due to interlayer coupling. The interlayer interaction determines to which degree the band structure is alternated as one decrease number of layers. In a more technical approach, the wave function overlap and interaction between layers determines to which degree the band structure is changed with number of layers. The vdW energy - energy required to exfoliate layered crystals, or the cost of removing a single layer from the surface of the bulk compound, has been estimated from both experiments [15, 16].

Interlayer coupling is a factor which gives rise to the phenomena of valence band maximum (VBM) splitting. In a multilayered structure spin-orbit coupling (SOC) as well as interlayer coupling determines VBM splitting, and VBM splitting becomes important in section 2.4. SOC is a relativistic effect which will be discussed in subsection 2.4.4. As one reached monolayer structures the effect of interlayer coupling disappears in VBM splitting, the monolayer behaves as an isolated layer, however we can still see the effect of SOC in some 2D-materials.

2.3 The Envelope Function Approximation for Quasi-Two-Dimensional Systems & Dirac equation

This brief section applied for the sole purpose of giving the reader a more in-depth view of the rich and complex physics present in condensed matter and quantum physics. We will not go into depth on any of the topics discussed here, but rather give an overview. Where we dip our toes into the envelope function and Dirac equation in order to give a more in-depth understanding of the physics occurring within these crystalline materials. This section is based on the book "Spin-Orbit Coupling in Two-Dimensional Electron and Hole Systems" [17]

2.3.1 Envelope Functions

Real crystals are not perfect, as we have touched upon throughout this chapter. Their translational symmetry can be perturbed, either by unwanted lattice imperfections, or by intentionally built-in defects. The question then rises, how do the wave functions and energy leves look in such a perturbed crystal? This question can not be answered by the simple S.H equation, an approximation in the form of a slowly varying envelope function is needed - called the Envelope Function Approximation (EFA). We will not go into depth on $\mathbf{k} \cdot \mathbf{p}$ - theory, and derive the entire EFA.

[6] Typically graphene is produced in this way, furthermore the so-called transition metal dichalcogenide (TMDC) are also layered structures with vdW forces. DFT calculation may determine interlayer binding energies in order to achieve mechanical exfoliation.

A perturbed crystal gives rise to internal electric or magnetic fields which alters the lattice potential. If we where to consider a lattice imperfection with the perturbation potential $V_p(\mathbf{r})$, this potential takes into account various defects formation which induces electric and magnetic fields. For simplicity, we take only one electronic band into account. It is important to notice that the perturbed potential is slowly varying on the scale of the crystal unit cell. The Schrödinger equation for the imperfect crystal reads:

$$\left[-\frac{\hbar^2}{2m^*}\nabla + V_{lattice}(\mathbf{r}) + V_p(\mathbf{r})\right]\psi_{\mathbf{k}}(\mathbf{r}) = E\psi_{\mathbf{k}}(\mathbf{r}) \tag{2.52}$$

The additional term $V_p(\mathbf{r})$ is incorporated into the equation. We are not able to solve this by the use of the conventional wavefunction as formulated in subsection 2.1.1. As the potential is perturbed the wavefunction is also perturbed to follow the slowly varying potential applied. As the Bloch function in the previous case takes into account the periodicity of the crystal structure our new envelope function is indeed affected by the defect formations. The resulting Envelope function may be formulated with the influence of effective mass approximation as follows:

$$\psi'_{\mathbf{k}'}(\mathbf{r}) = \frac{1}{\sqrt{\Omega}}\sum_{\mathbf{k}'} c_{\mathbf{k}'} e^{i\mathbf{k}'\mathbf{r}'} \tag{2.53}$$

Substituting this Envelope function into our wave equation yields the Envelope wave equation, which is given as:

$$\left[-\frac{\hbar^2}{2m^*}\nabla + V_p(\mathbf{r})\right]\psi'_{\mathbf{k}'}(\mathbf{r}) = [E - E_C]\psi'_{\mathbf{k}'}(\mathbf{r}) \tag{2.54}$$

This Envelope function solves the energy eigenvalues for the perturbed system with potential $V_p(\mathbf{r})$, it is only valid for slowly varying potential on the scale of the crystal unit cell, as mentioned. Notice that the energy eigenvalues are given relative to the conduction band E_C. The means of this Envelope function is to solve energy eigenvalues of a perturbed crystal potential with a slowly varying wavefunction - called the Envelope wavefunction.

2.3.2 Dirac equation - relativistic Schr*ö*dinger equation

So far we have investigated Bloch electron which travels in a periodic structure, where they are considered free in the exception of scattering mechanisms. These Bloch electron travel with thermal velocities in the order of (10^7cm/s) in semiconductors, and relativistic effects may therefor be neglected. Once the electron approaches the speed of light ($c = 3.0 \times 10^{10}$ cm/s) relativistic effects needs to be incorporated into our equations of motion. There are some fine examples of which such effects is needed in order to approximate the solution to

a finer degree.

The most known example unfolds itself in graphene, where we observe so-called Dirac-cones in the bandstructure at the K, K'-points, where we have time-reversal and inversion symmetry[7]. These Dirac-cones show a linear dependent dispersion relation which yields mass-less Dirac-fermions. As these electron experience no mass, they reaches the speed of light within these reciprocal space locations, and therefore Dirac equation is needed in order to fully understand and approximate the energy eigenvalues at these subbands. Furthermore, SOC, as briefly mentioned in subsection 2.2.2 is dependent of relativistic effects. Due to Coulomb interaction between the nuclei and electron, electrons near the nuclei reaches velocities near the speed of light, typically for 2D TMDCs the SOC is originated from d-orbitals of the heavy metal atoms. Large nuclei with correspondingly larger charge induces a greater SOC effect. As usual, S.H equation is not valid here and the implementation of relativistic effects needs to be considered. The Dirac equation may be formulated as:

$$\left[\left(\underbrace{-\frac{\hbar^2}{2m_0}\frac{\partial^2}{\partial\mathbf{r}^2}+V(\mathbf{r})}_{\text{S.H}}+\underbrace{\frac{1}{8m_0^3c^2}\frac{\partial^4}{\partial\mathbf{r}^4}-\frac{\hbar^2}{4m_0^2c^2}\frac{\partial V(\mathbf{r})}{\partial\mathbf{r}}\cdot\frac{\partial}{\partial\mathbf{r}}}_{\text{Relativistic correction}}\right)\underline{1}-\underbrace{\frac{i\hbar^2}{4m_0^2c^2}\underline{\sigma}\cdot\left(\frac{\partial V(\mathbf{r})}{\partial\mathbf{r}}\times\frac{\partial}{\partial\mathbf{r}}\right)}_{\text{SOC}}\right]\psi=\epsilon\psi \tag{2.55}$$

The relativistic corrections within the curly brakets are correction of the potential and kinetic energies as implemented in the original S.H equation. The last term within the curly brakets named SOC, is the spin-orbit coupling term. Further information about Dirac equation will not be addressed.

As mentioned, Graphene exhibit Dirac cones, however, this is a rare quality in 2D materials. There has been some studies showing that a square-octagon square lattice monolayer of MoS_2 showed Dirac-cones. The Dirac cones where forming in the $d_{x^2-y^2}$ orbitals. Whereas as d_{z^2} exhibits heavy fermions, approximately $1.1m_e$ from $X-\Gamma$ and $1.78m_e$ from $M-\Gamma$. The masse-less Dirac-fermions where calculated to have a velocity of $v_F = 2.3 - 2.4 \times 10^6 m/s$, which is indeed comparable to the mass-less Dirac-fermions in graphene. [18]

2.4 Excitons - Quasiparticles in 2D

This section focuses on the creation and property of the exciton quasiparticle in two dimensions. Firstly a furthered explanation of the band structure is needed, then we explain the formation and

[7] Time-reversal symmetry yields $\epsilon_n(\mathbf{k},\uparrow)=\epsilon_n(-\mathbf{k},\downarrow)$ and inversion symmetry yields $\epsilon_n(\mathbf{k},\uparrow)=\epsilon_n(-\mathbf{k},\uparrow)$. The presence of both symmetries gives Kramers' degeneracy which is formulated as $\epsilon_n(\mathbf{k},\uparrow)=\epsilon_n(\mathbf{k},\downarrow)$. In the case of SOC, inversion symmetry is broken and splitting off energy bands that lift degeneracy unfolds itself: $\epsilon_n(\mathbf{k},\uparrow)\neq\epsilon_n(\mathbf{k},\downarrow)$

creation of excitons by electron-hole pairs. A brief explanation of the variety of electron-hole pair interactions is presented - where we see two distinct excitons: Wanner-Moth and Frenkel excitons. Their binding energies and recombination mechanisms is discussed, and finally the influence of spin-orbit coupling is implemented.

This section is based upon the review article "Exciton physics and device application of two-dimensional transition metal dichalcogenide semiconductors" [19] and a number of books "Spin-Orbit Coupling in Two-Dimensional Electron and Hole Systems" [17], "Introduction to solid state physics" by Kittel,C [10], and "Two-Dimensional Transition-Metal Dichalcogenides" [20, 21]

2.4.1 Electron band structure cont.

The electric band structure where briefly discussed in section 2.1.3, where figure 2.4 shows **The nearly free electron model** and simplified picture of valence band and conduction band in an intrinsic semiconductor. In order to understand Excitons, a slightly different approach is needed. The band structure of a semiconductor is often given in terms of $\epsilon_n(\mathbf{k})$ in **k**-space. Where the high-symmetry points is of main interest - these high-symmetry points are aligned at origo and at the 1.st Brillouin zone edges. Furthermore, it is often convenient to give an explanation through the free electron model. Here we may as previously, describe our electron through the electron dispersion relations from equation 2.31. The electron effective mass is already taken into account here. What emerges from this equation is a set of parabolas, with various quantum number n. We are in this case interested in the quantum number which yields the valence and conduction band. Since, it is between these that the bandgap emerges.

If we use this approach to describe the valence and conduction band, the electrons are placed in the valence band and exhibits different **k**-values, as previously. In this case they do indeed exhibit an effective mass due to the curvature of the bands. Electrons in the valence band may experience an increase in energy due to various influences in the crystal structure. Thermal energy is a possibility as well as photon energy of an incoming light source. Thermal energy is often transferred to lattice vibration or phonons. High temperature yield an higher thermal energy which is often converted to higher phonon modes. In light of excitons, which will be described in the subsequent section, photons is of great importance. If a light source with photon energy at the magnitude of the energy bandgap $E_g \leq \hbar\omega_{\mathbf{k}}$, where $\omega_{\mathbf{k}}$ is the angular frequency of the incoming light, this contains information about the frequency as well as the wavelength. If the energy of the photon is large enough, there is a possibility that the incoming light excites the electron from the valence band into another unoccupied energy level. Note that the bandgap is undefined in the sense that electron can not be present in this regime due to lack of electron orbital levels. The only possible energy levels for the electron in an otherwise occupied valence band is the conduction band which is in this case unoccupied.

We have two kinds of valence and conduction band transitions, direct and indirect bands. In the case of a direct bandgap the valence and conduction band is placed at the identical **k**-value. This has profound impact in photoluminescence, as the excitation of electrons does not need to change momentum in the excitation process. In the other case, indirect banggap, the valence and conduction band is misplaced in **k**-space. If an excitation of electrons where to take place, we also need to convert some of the energy into **k**-space transfer, meaning that some of the energy under this process is lost in heat dissipation - energy may be converted into thermal energy or lattice vibrations.

If one where to illustrate the various processes figure 2.8 is a good place to start. In figure 2.8a) a simplified electron band structure is illustrated, where to the left we have a direct bandgap and to the right an indirect bandgap. The curvature of the bands is approximated through the electron dispersion relation by a simple $\mathbf{k}^2$-behaviour. The inset showing exciton energy levels will be addressed in the subsequent section 2.4.2. The figure to the right in a) show an indirect bandgap, where a shift in **k**-space is precent between the valence and conduction band. Important to note that the axis are $\epsilon_{n\mathbf{k}}$ as a function of $\mathbf{k_x}$, in this case. Meaning, we are in principle looking at a one dimensional band structure which unfolds itself into a two dimensional plot. In figure 2.8b) an illustration of a two dimensional band structure with $\epsilon_{n\mathbf{k}}$ as a function of $\mathbf{k_x}, \mathbf{k_y}$, which unfolds in a three dimensional plot. Meaning if we where to examine a three dimensional band structure we would need a four dimensional plot, which is inconceivable to the human eye.

As we are working with quasi-two dimensional system we would indeed need all three spatial directions in order to describe the band structure. It is therefore convenient to

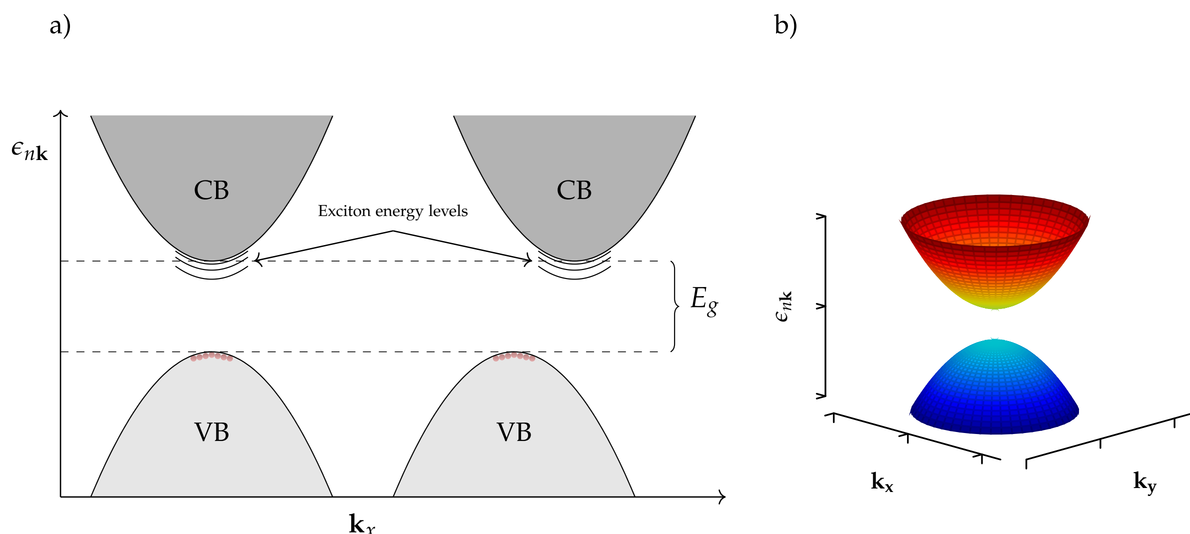

Figure 2.8: Band structure depicted from the free electron energy fermi-gas dispersion relation, showing. a) Band structure in one dimension showing bandgap as well as valence band and conduction band, The two insets show direct and indirect bandgap respectively. Red dots illustrates electrons in the upper valence band energy levels. b) A two dimensional example of the band structure, showing energy as a function of $\mathbf{k_x}, \mathbf{k_y}$, where the valence and conduction band is separated by a bandgap E_g

produce a so-called irreducible Brillouin zone from the 1.st Brillouin zone. This irreducible Brillouin zone consist of the special symmetry points as mentioned earlier. In a sense we are only interested in the paths between each special symmetry point - due to translation symmetry this comprehensively incorporate all values of interest whitin the 1.st Brillouin zone, without loss of generality. We may then present the band structure as a classical two dimensional band structure.

In Figure 2.9 a real *Density Functional Theory* (DFT) calculation of a two dimensional transition metal dichalcogenide (TMDC) MoS_2 is presented. In a) we see an illustration of the 1.st Brillouin zone as well as the irreducible Brillouin zone in red lines. The high symmetry lines are here called $[\Gamma, K, M, L, H, A]$. In figure 2.9b) the actual DFT-calculations are presented, showing the band structure of the two dimensional MoS_2, as well as the density of states. As we may see, MoS_2 exhibit a direct bandgap at the high symmetry point K [8]. In close proximity to K, the approximated dispersion relation yields an adequate estimate. As mentioned in the previous sections, each band comes from different contribution from electron orbitals. The main orbital character at the edge of the valence band is due to a combination of $d_{x_2-y_2}$ and d_{xy} orbitals from Mo-metal, which hybridizes with p_x and p_y orbitals of the chalcogen atom S. The edge of the conduction band is formed by $d_{3z_2-r_2}$ orbital of Mo-metal, additionally some contribution of p_x and p_y orbitals of S atom.

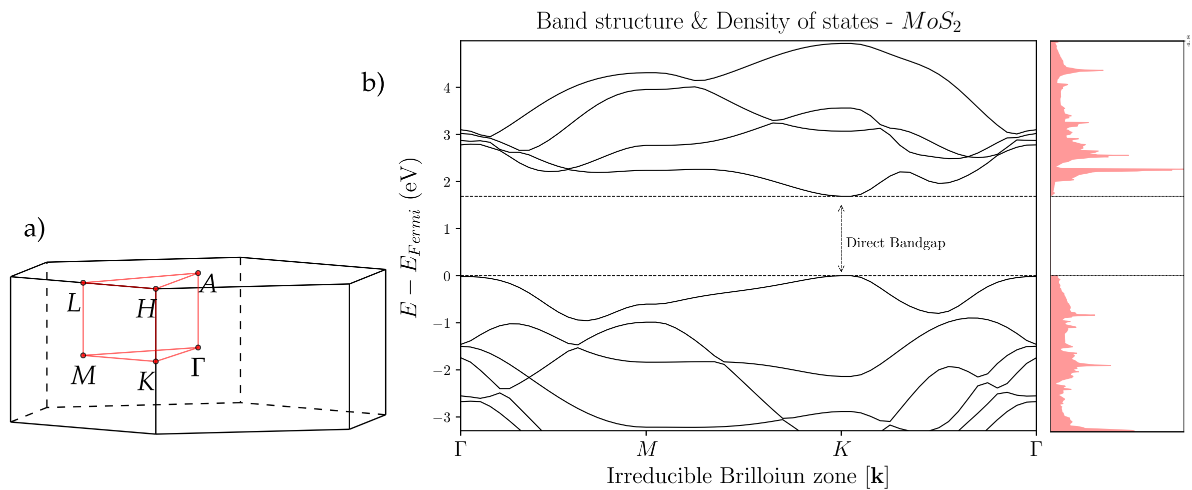

Figure 2.9: a) Irreducible Brillouin zone of 1.st Brillouin zone of Hexagonal structure in three dimensions. Showing special symmetry points along the sides and edges. b) Band structure and Density off states as *ab intitio* calculated using density functional theory (DFT) by simulation package (VASP) of monolayer MoS_2. Arrows indicates the indirect bandgap at the special symmetri point K. Band structure and density of states of MoS_2 presented, were calculated during the course of FYS-MENA4111.

[8] MoS_2 exhibits an indirect bandgap at bulk structure, as the dimension is reduced we see an indirect-direct bandgap transition.

2.4.2 Electron-hole pairs - Creation of excitons

Electron-hole pairs have a significant meaning in physics, especially in semiconductors and transistors. Previously in this chapter we have investigated the creation of the bandstructure and the meaning of energy levels in which the electrons occupy. Further on we have also seen how electrons interact trough scattering mechanisms. These mechanism may very well excite electron to the nearest free orbital or energy level. In semiconductors we know by now that the electrons are prohibited from choosing energy levels which lies in-between the valence and conduction band. Thereby, in order to excite electrons which lie in the top of the valence band, an energy larger than the bandgap is necessary. An energy source is needed to provide the electron the sufficient energy in order to be excited, and this source may very well be electromagnetic waves with energy $\hbar\omega$, such as photons. Incoming light excites a given electron in the valence band with energy $\hbar\omega = E_g$. Consequently, the excited electron naturally leaves behind a positively charged hole. By this the electron and hole has a coupling constituted by electro-static forces, such Coulomb forces. The coupling between electron and hole are named exciton, which is a quasi-particle with neutral charge.

The relationship between the coupled electron and hole are explained by considering $\mathbf{k} - space$. The total wavevector of an otherwise filled valence band is zero, due to inversion symmetry ($\mathbf{r} \rightarrow -\mathbf{r}$) and that the summation over the entire Brillouin zone yields zero. If an electron at $\mathbf{k_e}$ where to be excited, the total wavevector is deduced to $-\mathbf{k_e}$. This is then applied to the description of the hole. We then get $\mathbf{k_h} = -\mathbf{k_e}$. Further on, a hole is different from the electron by the obvious term, namely the charge, but it also possesses different spin (m_s). As mentioned, electrons have spin $\pm\frac{1}{2}$, whereas the holes have spin $m_s = \frac{3}{2}$. The coupling between electron and hole provides an integer spin value, the consequence of this spin value is that the Exciton quasi-particle is treated as a Bose-Einstein condensate [9].

We mainly differentiate between to types of excitons, Wanner-Moth and Frenkel exciton as seen in figure 2.10. The difference is mostly due to the coupling between the electron and hole. As we know by now, in two-dimensional semiconductors the electron is confined in the plane due to boundaries at the surface. As the exciton is created from various processes they are bound by Coulomb forces, and the effect of these Coulomb forces is affected by the electric field screening. For semiconductors the relative permittivity is relatively large, which means dipoles generally align, and thereby inducing a field. This field reduced the Coulomb interaction between the electron and hole. Consequently, the radius is large in-between the electron and hole, this is called Wanner-Moth excitons. As for material with small relative permittivity the opposite is true, the internal field weakly screens the Coulomb interactions and the electron-hole is more densely packed, yielding a shorter radius named Frenkel

[9]The fact that excitons exhibit integer spin values, opens up the possibility of an electron pairing mechanism similar to Cooper-pairs - in relation to superconductivity. This is theoretical work which has not been realised experimentally. The main idea is to create layered structure of semiconductors and metals in order to induce the relative permativity to increase the binding energy of excitons which consequently would increase the critical temperature T_c for superconductivity. [22, 23]

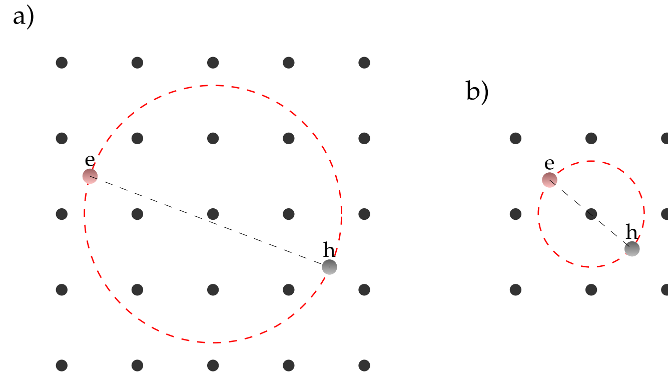

Figure 2.10: Illustration showing the bound state between the electron and hole resulting in excitons in a crystal structure lattice. a) Wanner-Moth exciton with small dielectric constant , yielding a large radius between electron and hole. b) Frenkel exciton with radius in the range of the unit cell, given by the small dielectric constant.

exciton. Interestingly, for quasi-two dimensional material, this relative permittivity can drastically decrease as the dimension in reduced. This is mainly due to confinement effects, the electric field screening is reduced due to change in the relative permittivity, the exciton is confined in the monolayer plane with a small radius (Typically, in the order of the unit cell). This provides an interesting topic of research for quasi-two dimensional materials, as the exciton binding energies has increased.

2.4.3 Exciton binding energy & recombination

Binding energy

As mentioned, electron and holes couple through electro-static forces, such as Coulomb forces. This particular force between electron and holes may be converted into binding energy. This is the energy needed for the electron and hole to loose its coupling and recombine. One may also see it as the difference between the electronic and optical bandgaps[10], which reflects the strength of the Coulomb interaction. Typical exciton binding energies are in the meV range, however TMDCs are a magnitude order larger - these values all point to exceptionally strong Coulomb interaction, due to the large effective masses of both electrons and holes and the reduced screening in the quasi-two dimensional limit. Once the electron is excited to the conduction band, and a coupling between the electron and hole emerges, the total energy of the exciton is reduced by the exciton binding energy. The energy of the bound electron or exciton is lowered due to attractive Coulomb forces. As we can see from figure 2.10, the exciton resonances occur within the forbidden bandgap. This is only possible due to the lowering of energy from Coulomb interaction, and under

[10]Optical bandgap is used for optical measurement when a photon excites an electron to the conduction band. It is the possible to measure the optical bandgap through photoluminescence or cathodeluminescence, the energy required to create an exciton is measured

excitonic effects, strong peaks at energies equal to $E_{ex}^{2D}(n)$ just below the band edge are expected to appear in absorption and emission spectra.

In order to determine the excitons binding energy one need to possess the relative permattivity of the material, spectroscopic ellipsometry [11], is an effective method to measure the dielectric constant directly. Furthermore the binding energy may be determined by the 2D screened potential, and solved by (S.H) as we have seen previously. This model for solving the exciting binding energy for quasi-two dimensional materials was provided by Thomas Olsen, Simone Latini, Filip Rasmussen, and Kristian S. Thygesen [24]

$$\left[-\frac{\nabla^2}{2\mu} + W(\mathbf{r})\right]\psi(\mathbf{r}) = E_n\psi(\mathbf{r}) \tag{2.56}$$

This is not much different from the Envelope function we showed in subsection 2.3.1, where equation 2.54 provides the same information, except, in this case we use μ as the effective mass of the exciton. $W(\mathbf{r})$ 2D convolution of the Coulomb interaction. Previous reports have suggested that a 2D Rydberg series is sufficient for calculating the exciton binding energy, as reported in [24], the exciton spectrum of WS_2 was measured and shown to deviate significantly from the Rydberg series of a 2D hydrogen model scaled by an overall screening factor. By some calculations, they ended up with an expression for the exciton binding energy.

$$E_{ex}^{2D}(n) = E_g - \frac{\mu}{2(n-\frac{1}{2})^2\epsilon_n^2} \tag{2.57}$$

This is model is based upon the Rydberg Excitonic Series, but has implemented the n-dependent relative permittivity (ϵ_n) as well as the effective mass of the exciton ($\frac{1}{\mu} = \frac{1}{m_e^*} + \frac{1}{m_h^*}$). This model estimates the exciton energy levels as depicted in figure 2.10, by the overall screening factor ϵ_n and quantum number n. Quantum number n = 1 has the lowest exciton energy level, namely the exciton ground state, and correspondingly the highest exciton binding energy, and n = ∞ diverges towards the lowest energy state of E_C.

Recombination

We mentioned that the typical exciton binding energy for TMDCs are a magnitude order larger than that of bulk materials which lies in the meV range. In comparison the thermal energy at room-temperature is as mentioned in subsection 2.2.2 $E_{RT} = 26meV$, this would mean that the coupling between electron and hole would be destroyed and the recombination probability would increase. We briefly mentioned direct and indirect bandgaps in

[11]Spectroscopic ellipsometry is an optical technique used for measuring dielectric properties of materials. Ellipsometry measures the change of polarization upon reflection or transmission - by this dielectric properties are extracted

section 2.4.1,and this material quality has profound consequence of exciton recombination mechanism. For a direct bandgap semiconductor the recombination occurs spontaneously, meaning that the probability of an electron and hole to recombine is constant in time. One could then expect an exponential solution to the excess carriers and that the electrons and holes recombine in pairs, meaning that the concentration of excess electrons and holes remains are equal throughout the recombination process. By excess electron and holes, we mean the concentration of electrons and holes created by excitations.

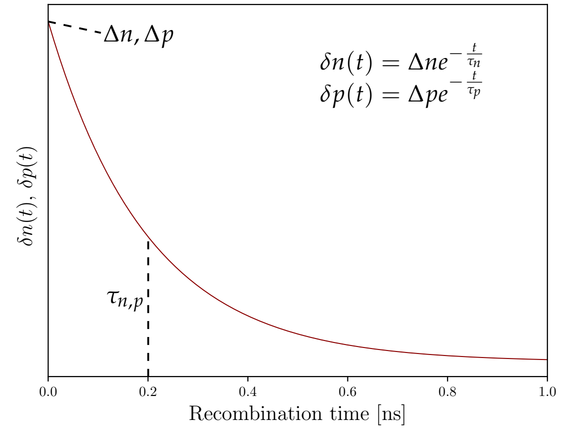

Figure 2.11: Decay of excess carriers by recombination.

$$\delta n(t) = \Delta n e^{-\frac{t}{\tau_n}} \tag{2.58}$$

Where $\delta n(t)$ is the change of carrier concentration with time (t), Δn is the excess carrier concentration at initial time. τ_n is the carrier lifetime, a general expression may be formulated as:

$$\tau_n = \frac{1}{\alpha_r(n_e + p_h)} \tag{2.59}$$

α_r is the proportionality for recombination and n_e, p_h is the electron and hole concentration shown in equations 2.32, 2.33. As shown in figure 2.11, the excess electron and holes recombine in an exponential manner. Usually, recombination times is in the order of $10^{-9} - 10^{-15}s$. Recombination times in the order of ps is a typical value for many semiconductors. Once excitons is created they may either recombine radiatively, meaning - as a direct band transition, emitting electromagnetic radiation in the visual range or non-radiativley, through indirect band transitions. As explained earlier, through indirect transitions, the electron scatters with phonons to adjust for the momentum space difference. One would have a wide range of possibilities of recombination, one could suggest defect levels within the bandgap that acts like intermediate transition states for the electron, this implication would prolong the recombination time. Furthermore, the recombination through phonon scattering or background carriers would mean non-radiatively recombination outside the light cone, into so-called dark states.

2.4.4 Spin-Orbit coupling

Spin-Orbit coupling (SOC) is an interesting phenomena which occurs in some semiconductors. One of the effects which is observable from SOC is VBM splitting, as well as a potentially much weaker CBM splitting. These effects is observable in photoluminescence and cathodoluminescence experiments, where one investigate the optical spectra of a material. The bandgap observed is called the optical bandgap as mentioned in 2.4.3. Due to the splitting of VBM one can observe an additional peak in the optical spectra which is manifested from SOC. We briefly mentioned the potential mechanism behind VBM splitting - interlayer coupling as well as SOC, however, in pure two-dimensional materials the interlayer coupling vanishes yielding SOC as the main contributor.

The most typical occurrence of SOC is in two-dimensional materials. The reason for this can be reviewed from symmetry arguments, where one finds that SOC is possible with broken inversion symmetry. As mentioned in the footnote in 2.3.2, Time-reversal symmetry dictates that the energy at a band $\epsilon_n(\mathbf{k}, \uparrow)$ is equal to the energy of band $\epsilon_n(-\mathbf{k}, \downarrow)$. Time-reversal symmetry then yields the criteria $\epsilon_n(\mathbf{k}, \uparrow) = \epsilon_n(-\mathbf{k}, \downarrow)$, furthermore the inversion symmetry follows the operation $\mathbf{k} \rightarrow -\mathbf{k}$, which give us $\epsilon_n(\mathbf{k}, \uparrow) = \epsilon_n(-\mathbf{k}, \uparrow)$. The presence of both Time-reversal symmetry and inversion symmetry gives what is called Kramers' degeneracy - $\epsilon_n(\mathbf{k}, \uparrow) = \epsilon_n(\mathbf{k}, \downarrow)$. This does not lift the degeneracy, and consequently VBM splitting is absent. Breaking off inversion symmetry is present in two dimensional materials, and this implies that SOC could be present and the degeneracy is lifted. The splitting of energy bands that lifts degeneracy may be written as - $\epsilon_n(\mathbf{k}, \uparrow) \neq \epsilon_n(\mathbf{k}, \downarrow)$, where the difference in energy is the VBM splitting energy Δ_{SOC}, associated with SOC.

We mentioned in the Dirac equation in subsection 2.3.2, whereas one of the contribution to the relativistic effects was the SOC. Further-on, due to the strong internal field near the nuclei the electron in the vicinity would feel a strong effect from the internal field, which would induce a higher velocity. SOC becomes stronger with increasing nuclei with correspondingly increasing charge. Typically heavy metal atoms produces large VBM splitting due to a large SOC. The Dirac equation, as seen, incorporate the SOC as a third term yielding a more precise measurement of the Dirac equation as well as reducing symmetry and removing some degeneracies of valence band states (conduction band states) - providing spin-orbit splitting

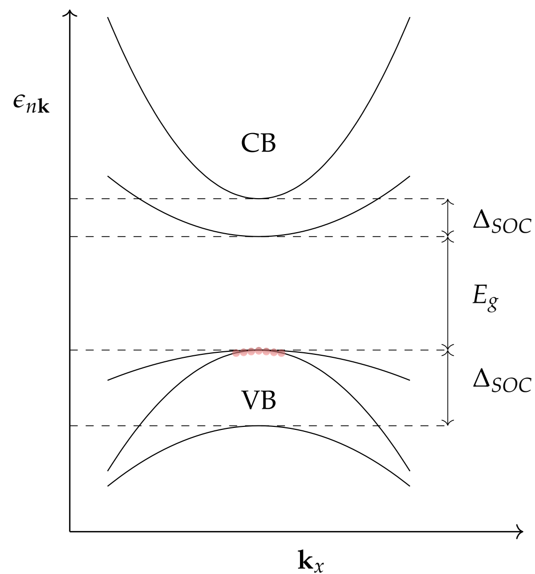

Figure 2.12: Bandstructure showing conduction band (CB) and valence band (CV), effect of Spin-Orbit coupling splitting the valence band by energy Δ_{SOC}.

of valence band (conduction band). The SOC term is also relativistic, from our explanation this makes sense. Furthermore, the SOC term in the Dirac equation may be written in terms of angular momentum operator (**L**) and Pauli spin matrices **S**.

$$H_{SOC} = \frac{i\hbar^2}{4m_0^2c^2}\underline{\sigma} \cdot \left(\frac{\partial V(\mathbf{r})}{\partial \mathbf{r}} \times \frac{\partial}{\partial \mathbf{r}}\right) \tag{2.60}$$

$$H_{SOC} = \frac{1}{2m^2c^2}\frac{1}{\mathbf{r}}\frac{\partial V(r)}{\partial \mathbf{r}}\mathbf{S} \cdot \mathbf{L} \tag{2.61}$$

$$\mathbf{S} = \frac{\hbar}{2}\underline{\sigma} \qquad \mathbf{L} = -i\hbar(\mathbf{r} \times \nabla) \tag{2.62}$$

Here we have simply converted the H_{SOC} from subsection 2.3.2 to a form which consist of a clear insight into $\mathbf{S} \cdot \mathbf{L}$. Here we can see the direct coupling between spin and orbit - as given by the Pauli spin matrices and angular momentum operator. Further discussion related to VBM and CBM splitting and the difference in energy is manifested in $\mathbf{S} \cdot \mathbf{L}$ and which orbital that contribute to the given band.

Figure 2.12 shows a simplified illustration of the bandstructure of a direct material. The VBM is split as a consequence of SOC, the magnitude of Δ_{SOC} mainly depends upon the heavy metal atoms. As mentioned, one can observe this effect in photoluminescence experiments, but Δ_{SOC} needs to be sufficiently large in order to observe it. As indicated by $\epsilon_n(\mathbf{k}, \uparrow) \neq \epsilon_n(\mathbf{k}, \downarrow)$, the two subbands have spin up $\uparrow$ and spin down $\downarrow$ giving the possibility of optical selection rules.

In monolayer materials with broken inversion symmetry, the valence and/or conduction bands are split ut by the SOC. If we circle back to the discussion about Spin-valley coupling 2.2.3. The SOC would occur at the high symmetry points and the spin splitting must be opposite at the two equivalent valleys, meaning that potentially, multiple valley would experience a band splitting. One could potentially control excitation of spin up $\uparrow$ and spin down $\downarrow$ electrons by right and left-handed circularly polarized light[12], that only couples to a certain valley.

Keeping the previous sections in mind, particular features associated with quasi-two dimensional materials with decreasing dimensionality is the appearance of a direct bandgap, large binding energies of exciton due to large effective masses and reduced screening and their scattering mechanism which is quantum confined. Furthermore, many features are

[12] In order to achieve right or left-handed circular polarized light a photoelastic modulator may one implemented in the experimental setup. A photoelastic modulated is an optical device which modifies the polarization of the light source

detectable through various experiments such as photoluminescence and Raman scattering. In photoluminescence and cathodoluminescence it is possible to determine the transition from indirect to indirect bandgap by absorption measurements as well as detecting VBM splitting due to SOC. This furthers the discussion about features, as the dimensionality is reduces to monolayer the inversion symmetry is broken yielding SOC, which one can calculate using the relativistic Dirac equation in Density functional theory.

Chapter 3

Experimental Techniques

This chapter contains an overview of the experimental techniques used in this work. Transmission Electron Microscopy (TEM) has been central, and we describe the fundamentals behind different modes of operation and techniques that have been used. Furthermore, an introduction to Atomic Force Microscopy and Scanning Electron Microscope will be given. The aim is to provide descriptions and details of the employed techniques as a supplement to the information given in chapter 4. This chapter is based on the book "Physical Principles of Electron Microscopy" by R.F. Egerton [25]

3.1 Transmission Electron Microscopy (TEM)

Throughout this thesis Transmission Electron Microscopy (TEM) is extensively employed in order to analyse the sample. TEM's are widely used in the scientific community for its superior spacial resolution as well as imaging variety compared to other imaging techniques. TEM operates through a high electron energy beam accelerated towards the sample. Due to the low wavelength of the electron beam, high resolution imaging is possible. In contrast to SEM, TEM usually analyses the transmitted electrons after passing through the sample due to high electron accelerating voltages (60-300keV). Due to high acceleration voltages extreme details of the structure and morphology can be achieved at atomic scale. The development of TEM throughout the last decade is unchallenged. In 1986 Ruska was awarded the Nobel Prize in Physics for his work in Transmission Electron Microscope [26]. There have afterward been fundamental developments, and modern TEM's are able to achieve sub-angstrom spatial resolution. Furthermore, the development is still growing and the attention toward TEM's is ever increasing.

The are many different interaction mechanisms between the electron beam and the specimen, each with different physics in play. In this theses we will mainly focus on Scanning Transmission Electron Microscopy (STEM), which differs from TEM in that the incident electron beam is focused on a small region on the sample through various condenser lenses. Electron energy loss spectroscopy (EELS), which operates through STEM, and collect electrons within a certain energy range after interaction with the specimen (several scattering mechanisms involved). Energy Dispersive X-Ray Analysis (EDX) very well comparable to

various compositional mapping in SEM. Scattered x-rays from the surface from the incident electron beam is collected to form an energy dispersive map of the sample.

3.1.1 Scanning Transmission Electron Microscopy (STEM)

Historically, imaging in TEM-mode has been the most used method, however due to the increasing growth in the development of aberration, electron guns, and generally improved electronics, the interest in STEM has increased. One of the main attraction with operating TEM in STEM-mode is the improved spatial resolution, however, it also provides the opportunity of using multiple detectors simultaneously. This means that STEM is more versatile, able to collect different information from several scattering mechanisms.

As mentioned, development of aberration correction in STEM has improved greatly. This furthers the improvement of providing a smaller probe for increased resolution. As a consequence of a more local electron beam, the focused beam decrease illumination of the neighbouring columns in the specimen, enabling the possibility of increasing the probe current without decreasing the resolution. The ultimate goal is to improve resolution, and the decrease in probe size and increase in probe sharpness improves the contrast as well as signal-to-noise ratio.

In figure 3.1, and illustration of the STEM is provided, giving us a brief overview of the electron beam path towards the sample. In figure 3.1a) we have a pure STEM mode, showing the incident electron beam from the electron beam source. The electron beam source is typically a probe composed of W or ZrO_2-coated W, enabling a relatively coherent emission of electrons [1]. The high coherent emission of electrons is a criteria for the possibility of both coherent and incoherent[2] imaging which is crucial for STEM [27]. By applying a voltage at the probe tip a current is induced, further on, each electron increases its thermal energy as a function of current, at some point the electrons possesses enough energy to bypasses the work function of the solid.

By this the electrons are emitted from the solid to vacuum, an electrical field is applied for accelerating the electrons to high velocities given by eq. 2.39. Further on, the electron beam passes by the lenses, marked C1,C2 and C3, and an aperture is chosen optimised beam convergence. These lenses aims to focus the electron beam/wave front into a perfect

[1] Remember that electron are fermions, not bosons. Meaning that coherence in this sense is attributed to the individuality of each electron. When there is coherence between two points within the beam, it means that the individual electron wave has spread out over these two points.

[2] When talking about coherent and incoherent imaging one usually refers to the wave nature of electrons. In that sense, coherent represent elastically scattered electrons and incoherent represent inelastically scattered electrons

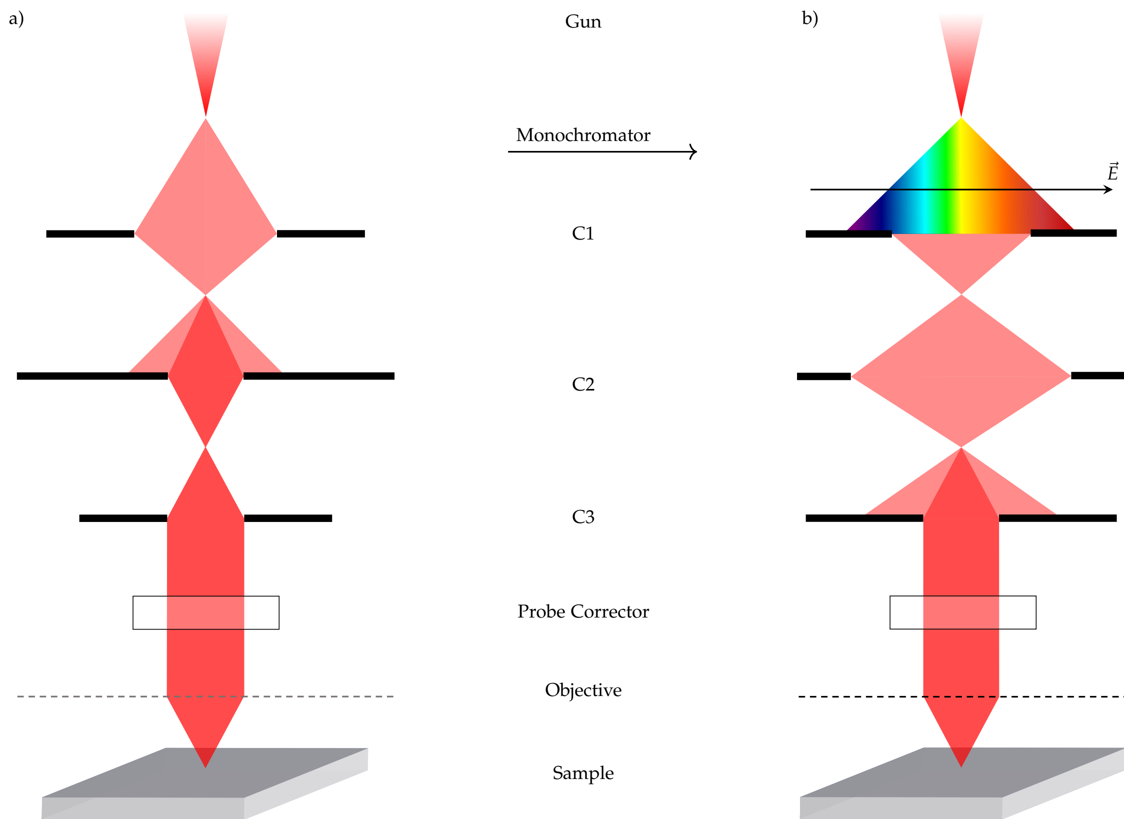

Figure 3.1: Beam paths of STEM without and with monochromator illustrated. a) Operational mode: STEM b) Operational mode: monochromated STEM

spherical wave so that it will eventually converge to a single point on the specimen. With the ongoing development of aberration correctors, the lenses are extremely complex, and differs from conventional lenses. These highly complex lenses consist of quadrupoles, hexapoles, or octuples, however, the physics and principle of optics remains the same. In figure 3.1 a monochromator is applied after the electron gun. The monochromator acts as an energy filter and is dispersing the electrons as a function of energy, and the first lens C1 and its aperture is selecting which energy range that should be bypassed. As a consequence of this filtering of electrons in the beam, the total beam current is decreases as well as the brightness, however, the electron brightness per electron volt energy spread remains constant. The use of a monochromator increases the spatial resolution of STEM images, and complementary, band gap measurements through EELS is enhanced [28–30]

Once the focused incident electron beam reaches the surface of the sample multiple scattering mechanisms between the electron beam and the sample takes place. The electron beam hits a column of atoms orthogonal to the surface plane and a cascade of scattering events occur. As seen in figure 3.2 once the electrons are scattered through the sample they have various angles according to the scattering mechanism that took place. We have four main detectors, which collect electrons that has transmitted from the sample at a certain angle β. Firstly, we have High-Angle Annular Dark-field Imaging (HAADF), also known as Z-contrast

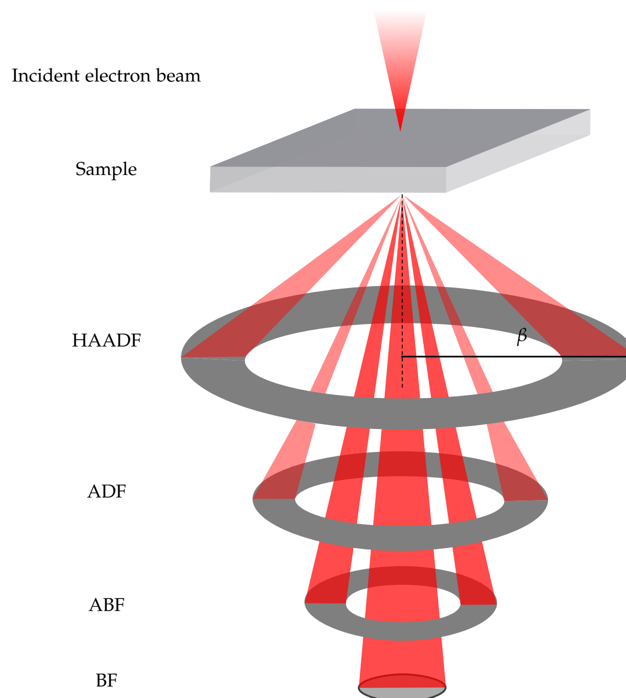

Figure 3.2: Imaging of sample through various detectors. Electron beam is scattered from the sample, at an angle β. STEM images is collected according to scattering angle. The detectors can be defined as High-Angle Annular Dark-Field (HAADF), Annular Dark-Field (ADF), Annular Bright Field (ABF) and Bright Field (BF).

imaging. HAADF is sensitive to atomic number (Z) and shows what is known as incoherent characteristic. Every electron that is not scattered at these angles consistent with the HAADF detector simple passes by and is collected through another detector. The reason HAADF is sensitive to atomic number is due to the high scattering angles achievable through electron-nucleus interactions. Once the high energy electron beam enters the sample some electrons will interact with the nucleus charge giving an unscreened high angle scattering. The scattering mechanism between electron and nucleus in this high energy regime becomes essentially pure Rutherford scattering[3] with a cross-section that is approximatly Z^2[4]. As the nuclear potential is localised in space, the scattering power becomes comparable to the thermal vibration amplitude of atoms. The incident electrons would then "see" the atoms with different atomic spacing and scatter in different direction - incoherent scattering. Further-on, incoherent imaging is the summation of scattering cross-sections and the scattering from an entire column is then approximated as $\langle Z^2 \rangle$. As the scattering cross-section provides information of number of particles scattered at a certain angle β per unit time per incident intensity, we would see a clear distinction between elements with different atomic number in HAADF image. In this respect, heavy elements provide a brighter contrast image than light elements.

[3]Elastic scattering of charged particles by Coulomb interactions

[4]As the nucleus potential is localised in space, this provide an image that makes the atoms appear smaller when seen through the HAADF detector.

Annular Dark-Field (ADF) captures slightly smaller angles than HAADF, furthermore, ADF also captures electrons which are affected by the screening of nucleus potential by localised electrons. Even though ADF collects electrons scattered due to higher screened potentials near the nucleus, it is still Z-number sensitive. It does, in fact, have a lower Z-number exponent compared to HAADF. One may also detect certain local characteristics such as local electric fields present due to strain. Annular Bright-Field (ABF) is mostly used for capturing lighter elements such as oxygen and nitrogen [31], as light elements have substantially less screened potential the scattered electrons are reflected at a much smaller angle than Dark-Field imaging. Lastly, we have Bright Field, this contains the initial electron beam. As the scattering angle is severely small compared to HAADF, ADF and ABF, the electron does not interact with the nucleus and one implies that the BF-detector collects unscattered electrons but with a high enough angle to collect outer Bragg reflections.

3.1.2 Electron Energy Loss Spectrometry (EELS)

The spectroscopy of electrons that passes through a thin sample in STEM is massively complex and offers a way to analyse the inelastically scattered electron through Electron Energy Loss spectroscopy (EELS). EELS is a powerful tool equipped to the STEM or TEM-mode and provides information about the energy loss of the inelastically scattered electrons. This information manifests itself to the chemical and structural properties of the specimen of study. As for the STEM-mode EELS electrons scattered through small angles enter an energy-loss spectrometer and form an energy-loss spectra or an energy-filtered image. [32]

When operating EELS through STEM-mode transmitted electrons scattered at large angles form a dark-field image, by feeding the signal from the annular detector to a display device as mentioned earlier. Furthermore, smaller scattered electrons transmitted through the sample forms the energy-loss spectra. The main principle behind EELS is the energy filter mechanism, this provides further information about the inelastically scattered electrons post sample. In figure 3.3a) an illustration of the electron beam passing through the sample is displayed. Once the electron beam is transmitted through the sample is reaches the Gatan Imaging Filter-entrance (GIF-entrance). The GIF-entrance aperture determines which portion of the electron beam that contribute to the spectrum image. The GIF consist of a series of apertures for correction, the apertures controls the collection angles as well as the signal intensity (I_c)for EELS. The most important feature of the GIF is the energy filter. This is a magnetic prism that generates a magnetic field to which the electrons respond to. The electron beam is bends 90° within this energy filter. Typical magnetic field is around 0.01T[32], and the magnetic field acts on the electron through $F = \mathbf{B}e\mathbf{v} = \frac{m\mathbf{v}^2}{R}$, where $\mathbf{B}$ is the applied magnetic field, e is the electron charge, $\mathbf{v}$ is the electron velocity, m is the relativistic mass and R is the radius at which the electron is bent. As the radius depends on the electron velocity it also depends on the kinetic energy of the electron.

$$R = \frac{m\mathbf{B}\mathbf{v}}{e}$$

Figure 3.3a) is just for illustration purposes, the electron beam passing through the energy filter, is bent as described above, elastically or unscattered electrons may contribute[5].These have the highest energy, and therefore the larges radius through the energy filter in GIF, they form the so-called zero-loss peak in the energy-loss spectra. As seen 3.3a), once the electron passes through the energy filter they goes through a series of lenses such as quadrupole and sextupole (named imaging optics). Finally, the filtered electron beam gets collected by a Charge-Coupled Device detector (CCD-detector). In figure 3.3b) a three dimensional illustration of the process is illustrated. An incident electron beam focused at a single point

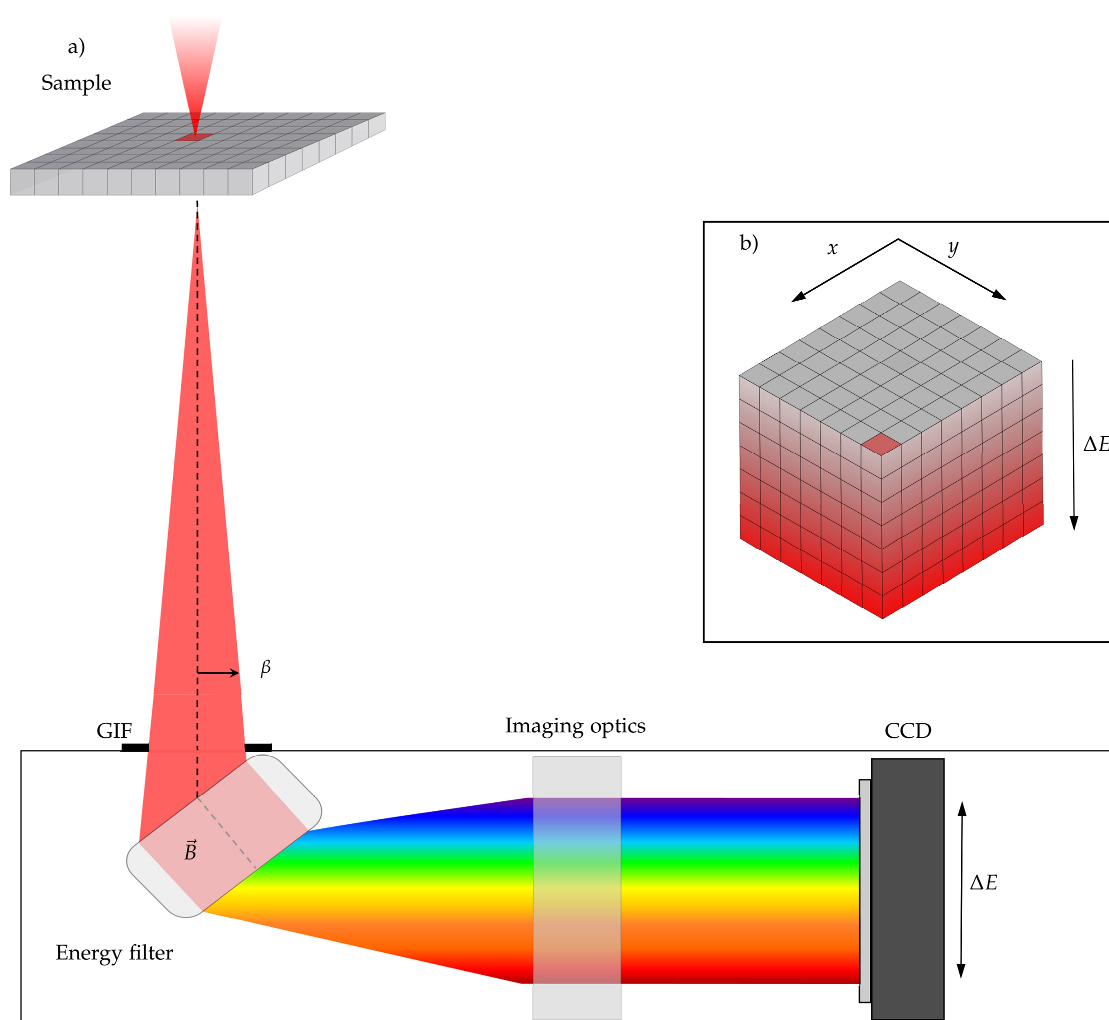

Figure 3.3: a) Illustration of EELS, where the incident beam penetrates the sample and gets collected in GIF-entrance. An energy filter is applied and the incident beam is collected in CCD. b) Schematic of electron energy loss as a function of x,y-position.

[5]Elastically scattered electrons are electrons that have negligible energy loss after scattering. This occurs when an electron is deflected by an electrostatic field of an atomic nucleus, which is determined by the screened potential of the electron around the nucleus.

(pixel) forms an entire EELS spectra according to 3.3a). The STEM scans through the desired region and EELS collects data for each pixel, creating a so-called EELS spectra.

In figure 3.4b) simplified illustration of different atomic excitation from various scattering mechanisms. The gray arrow, illustrated elastically or unscattered electrons which does not lose energy when transmitted, and they are collected and displayed as a zero-loss peak at $\Delta E \approx 0$ and this is seen as the most intense feature in EELS, see first region in figure 3.4a) . We usually separates EELS spectra in three regions, 1) zero-loss peak, 2) low-loss region and 3) high-loss/core-loss region, as depicted in figure 3.4a). The 'pink' arrow illustrates low-loss region interactions, where the incident electron beam scatters inelastically with the sample. In the case of semiconductors and insulators, the electrons get excited to the conduction band from the valence band as described in chapter 2. The intensity (I_c) in the EELS spectra is proportional with the joint density of states [6], meaning that the signal becomes visible within the energy range of the bandgap, typically energies are less than 50eV [33–35]. The high-loss or core-loss region which operates above 50eV stems from core electrons excitations, as illustrated by 'red' arrow. These are electrons within a deeper shell, and they need to acquire a large amount of energy in order to be excited to the conduction band. This region has much lower intensities than the low-loss region. Ionization occurs at this region, and each element has a characteristic binding energy E_k at each orbital, by this, one can determine which element that is present at a given pixel in the EELS spectra.

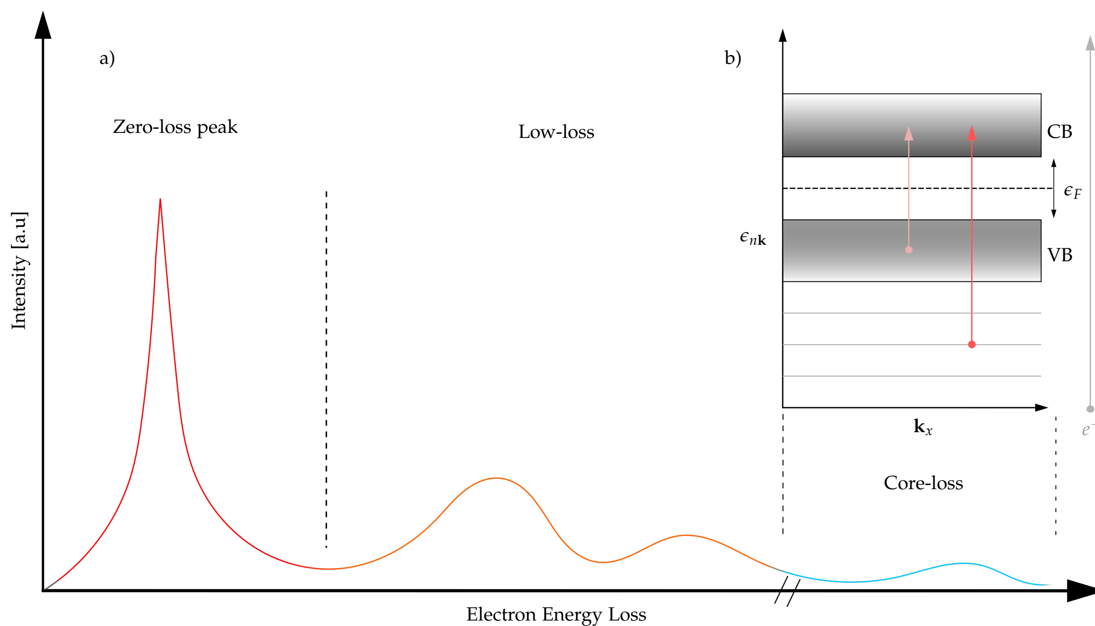

Figure 3.4: a) EELS spectra showing Zero-loss peak, low-loss and core-loss regions. b) Energy diagram is illustrated showing the atomic excitations from various scattering mechanisms.

[6]The joint density of states that appeared In the Fermi Golden rule subsection 2.2.2 is a consequence of the so-called Van Hove Singularity, which is when the derivative of the density of states diverges. This is due to band nesting, when valence and conduction band is parallel within a certain energy range ΔE. The joint density of states is then the number of electronic states in the conduction and valence band that are separated by a certain energy E_g.

Furthermore, one can calculate the amount of each element by measuring the intensity (I_c) above the background.

Plasmon energies and specimen thickness from EELS

Previously we discussed the low-loss region of EELS spectra. In this region we investigate the weakly bound valence electrons and their transition mechanisms. As mentioned in chapter 2 there are many forms of transition. Whether the electron is excited trough direct, indirect, intra- and interband [7] transitions is dependent on many factors, and we will not go any further into the specifics of the above-mentioned mechanisms. However, the Fermi-Golden rule is essential for explaining the probability and frequency of a certain transitions occuring. As for the low-loss region of EELS we have essentially looked at individual electrons excited to the conduction band or other intraband transitions - so-called single-electron mode of transition. As, we know there is a beam of initial electron passing through the sample. This collection of electron induces a local electric field in the sample. This induced field collectively displaces the 'free' electrons in the sample, causing a collective oscillation of electrons known as plasmons (in analogy to phonons). This collective oscillation of valence electron density takes the form of a longitudinal traveling wave and can be described as a pseudoparticle, *plasmon*, with energy $E_p = \hbar\omega_p$, where ω_p is the plasmon frequency - usually the plasmon energy lies in the range of 5-30eV for most solids. Furthermore the plasmons provide information about the dielectric function [36], valence electron densities, and in some cases, phases presented. The plasmon peak is the second most intense feature in EELS, and the *free electron* plasmon energy is described as [37]:

$$E_{p,F} = \hbar\omega_p = \hbar\sqrt{\frac{n_v e^2}{m_0 \epsilon_0}} \tag{3.1}$$

Where the plasmon frequency ω_p comes from the equation of motions in an applied electric field as well as polarization which is discribed by the displacement in the equation of motions. As we can see by 3.1 the plasmon frequency ω_p is proportional to the electron density in the valence band n_v, electron charge e, electron rest-mass m_0 and permittivity of free space ϵ_0. Furthermore, this *free electron* model has it limitations. For semiconductors, we also have a contribution from the core electrons in terms of another damped oscillation $\omega_b = \frac{E_g}{\hbar}$. This damped oscillations is influencing the *plasmon* oscillation as the core electron and ion core has strong interaction causing a damped oscillation mechanism to the *plasmon* oscillation. One may simply modify the *free electron* model to *semi-free electron* model by incorporating the damped oscillation arising from core electrons[37]: :

$$E_{p,S-F} = \hbar\sqrt{E_{p,F}^2 + E_g^2} \tag{3.2}$$

[7] Interband transitions refers to the transition between valence band and conduction band. Intraband transition refers to the transition within the same band.

EELS also possesses the possibility of local relative thickness measurments. As discussed earlier, STEM-EELS collects a set of spectra over the entire EELS spectra of choice. Furthermore, in each pixel one may calculate the relative thickness through *Poisson statistics* [32]:

$$P_n = \left(\frac{1}{n!}\right)\left(\frac{t}{\lambda}\right)^n e^{-\frac{t}{\lambda}} \tag{3.3}$$

Where P_n is the probability of exciting n plasmon peaks, t is the relative thickness and λ is the inelastic mean free path [8] By choosing $n = 0$ for the zero-loss peak one may rewrite 3.3 as:

$$P_0 = e^{-\frac{t}{\lambda}} = \frac{I_0}{I_t} \rightarrow \frac{t}{\lambda} = -ln\left(\frac{I_0}{I_t}\right) \tag{3.4}$$

Where we have rewritten P_0 as a fraction of integrals of zero-loss peak intensity I_0 and the entire EELS spectra integral I_t. Once the dimension is diminished and one approaches quasi-two dimensions so-called surface plasmons becomes dominant, surface plasmons dominates only at (<20nm). We have a simple relationship between bulk plasmon energies and surface plasmon energies E_s give by $E_p = \sqrt{2}E_s$[38].

Even though plasmon peak is the second most prominent feature in EELS spectra there is also a possibility to observe excitons, as discussed in 2.4. However, a high-resolution spectrometer is needed in order to detect the associated energy losses. The energy loss from an excited electron to an exciton state is observed adjacent to that of plasmon energy losses. Optical bandgaps is therefor possible to detect through high-resolution EELS measurements[9][37]. A number of books shows that the bandgap varies with sample thickness [20, 21], this is a well know phenomena for quasi-two dimensional materials, also, there is reports of strain [39] and plasmon energies [40] effect on bandgap. As thoroughly discussed in chapter 2, the effect on bandgap from variations in thickness is dependent on a numerous factors. The most important reason is the quantum confinement effects that becomes dominant for quasi-two dimensional materials. This effects the interlayer coupling distance as well as lattice parameters, which further redefines the band structure. The number of bands (N) also becomes more prominent as one reaches monolayer thickness - which again influences the band structure.

[8] The inelastic mean free path is the average distance an electron travels through a solid before losing energy - typically in the order of 100nm.

[9] By applying a monochromator to the EELS setup one may reach an energy resolution of 0.1-0.01eV [9]

3.1.3 Energy Dispersive X-Ray Spectroscopy (EDX)

Energy dispersive X-ray spectroscopy (EDX) is a widely used technique for determining elemental composition at high spatial resolution. EDX used in STEM-mode provides high spatial resolution due to the highly focused initial electron beam, and it is even possible to identify single atoms using this technique [41].

In figure 3.5a) we see an illustration of how EDX is set up in STEM. Where the initial electron beam operates as in standard STEM, with a highly focused beam localised at a single point (pixel) at the sample. Furthermore, characteristic X-rays are emitted from the sample and collected through a series of scintillation EDX detectors. As a consequence of the highly focused electron beam yielding high spatial resolution, one is subject to low count rate - yielding low signal-to-noise ratio. In this illustration four scintillation EDS detectors are displayed, this would increase the signal-to-noise ratio and optimise detector efficiency and acquisition time. In figure 3.5b) A simplified illustration of electron-electron interaction from initial electron beam and sample are displayed. The atom may be ionized by the initial electron beam, furthermore, an electron in a higher energy shell could relax to the free energy state. This de-excitation of an electron could emit a characteristic X-ray depending on the energy transfer occurring. We distinguish between multiple characteristic X-rays by $K-\alpha$ (red)$K-\beta$ (purple) and $L-\alpha$ (yellow). For further information about EDX the reader is referred to the book by Williams and Carter [42].

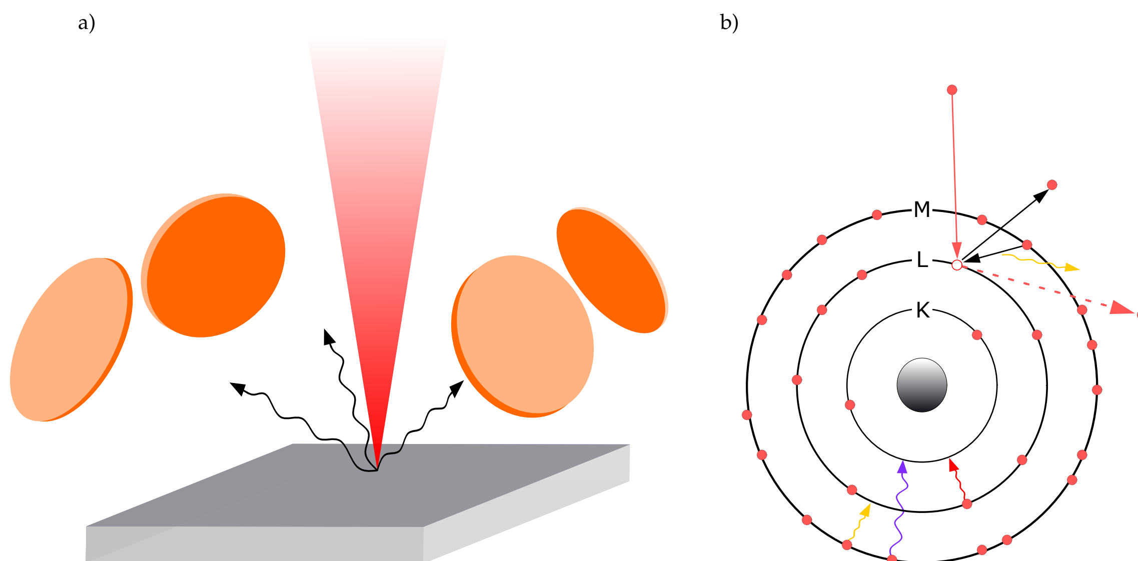

Figure 3.5: a) Simplified illustration of EDX, showing characteristic X-rays emitted from sample and detectors. b) illustration of electron-electron interaction, which indirectly causes a characteristic X-ray.

3.2 Atomic Force Microscopy (AFM)

Atomic Force Microscopy (AFM) is extensively used in the scientific community and is a type of scanning probe microscopy. As discussed in chapter 2, an important parameter for the properties of quasi-two dimensional materials is the number of atomic layers in the sample. AFM aims to, quantitatively, provide measurements of small variations in thickness. On the other hand, qualitative thickness variations in a flake can be observed with an optical microscope, but this provides no quantitative data [43, 44]. With AFM it is possible to identify a single atomic layer. The high sensitivity of this technique enables measurements down to the nanometer scale and the proven resolution is in the order of fractions of a nanometer [45]. This gives an improved resolution of 1000 times, compared to the optical diffraction limit.

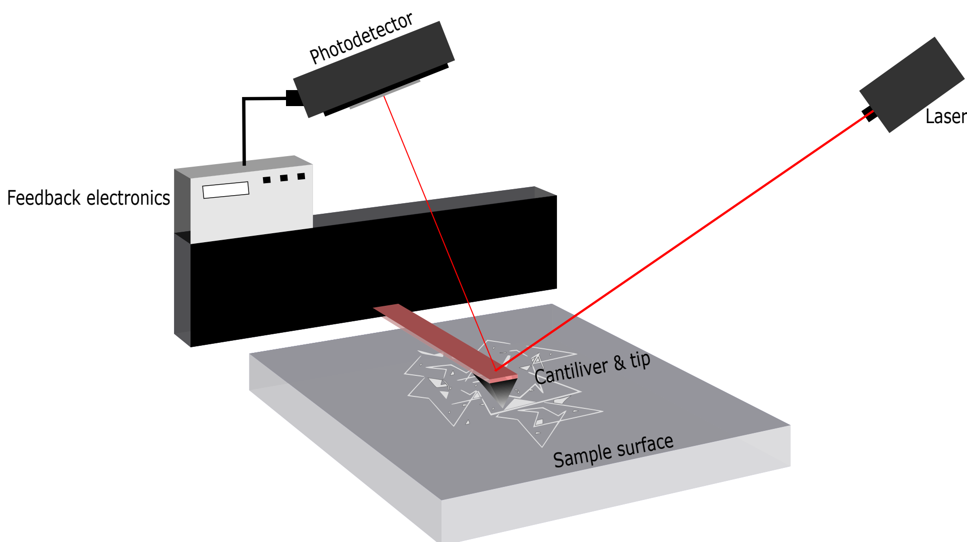

Figure 3.6: Simplified AFM setup. The laser beam is aimed at the cantilever for feedback, cantilever with a sharp tip scans the desired area. The laser beam is reflected towards a photodetector which forwards informations to the feedback electronics.

3.2.1 Working principles

In figure 3.6 we see the essential parts of an AFM setup. The cantilever acts as a beam for the tip, and its fundamental property is its elasticity. As the cantilever is elastic, it is possible to measure infinitesimal changes in its z-coordinates. The sharp tip placed at the end of the cantilever is usually made from silicon or silicon nitride, with a radius on the order of nanometers in order to achieve high resolution imaging. As seen in figure 3.6 the sample is placed underneath the cantilever and tip. A laser beam is directed towards the cantilever and reflected onto a photodetector. As the tip scans the sample surface, irregularities in the topography are detected by a slight change in the laser beams phase. The measured height, along with the corresponding x- and y-coordinates are stored as a 3D matrix. One of the

most common ways of illustrating the dataset is through a 2D map with colorbar of the z-direction.

When the tip is brought into close proximity of the sample a number of forces has to be taken into account, and according to Hook's law the cantilever will experience bending/deflection as a consequence of the acting forces. Depending on the material, imaging mode and situation, the forces that are measured in AFM include mechanical contact force, capillary forces, chemical bonding, electrostatic forces, magnetic forces and van der Waals forces.[46]

3.2.2 Imaging mode: Tapping mode

The imaging mode may vary, here we will talk about tapping mode. Keep in mind that there are other modes as well, such as non-contact and contact mode. Firstly, taping mode, also called dynamic mode, intermittent contact, AC mode, or vibrating mode.

Tapping mode is widely used and is gentle to the sample, as there is a small amount of force applied to the surface as well as a short duration of time when the tip is brought in close proximity to the sample surface. The distance between the tip and sample is approximately the distance needed for close range forces to be present. These forces are Van der Waals forces, dipole-dipole interactions and electrostatic forces and Van der Waals forces are strongest at about 1nm-10nm range. In tapping mode, the cantilever is driven to oscillate at its resonance frequency, determined by its spring constant. The resonance frequency of the cantilever regulates the scan rate. Higher resonance frequency yields a higher scan rate, AFM cantilevers with resonance frequency of 300kHz and above yields fast scan rates. In order to achieve and control the image contrast in AFM tapping-mode, we look at the difference in what is called set-point and free amplitudes of the cantilever and tip (prope). The free amplitude is the amplitude when the tip oscillates above the sample surface. Set-point amplitude is the amplitude when the tip is engaged to the surface.

3.3 Scanning Electron Microscope (SEM)

The scanning electron microscope is in many ways the little brother to Transmission electron microscope, discussed in 3.1. Due to high spatial resolution and many operating possibilities such as Energy Dispersive X-Ray Spectroscopy (EDX), cathodoluminescence (CL) and high resolution topography imaging it is a widely used instrument.

The working principle of an SEM is shown in figure 3.7. In the electron gun, electrons are emitted through either thermionic emission or field emission. In thermionic guns tungsten or LaB6 filaments are used, where the latter typically produces brighter emission and higher resolution. Field emission guns have even brighter emission and higher resolution than the thermionic LaB6 guns, but are also considerably more expensive.

The emitted electrons are accelerated through a potential of up to 30 kV and directed towards the sample. Before the beam hits the sample it goes through a number of condensers and objective lenses. The electron beam is scanned across the sample yielding an emission of electrons. The emitted electron or emission of X-rays is collected through a series of detectors placed in the vicinity of sample. The number of electrons collected in the detectors depends on the scattering angle, a steep and inhomogeneous sample would thereby produce a high contrast image, showing the topography of the sample.

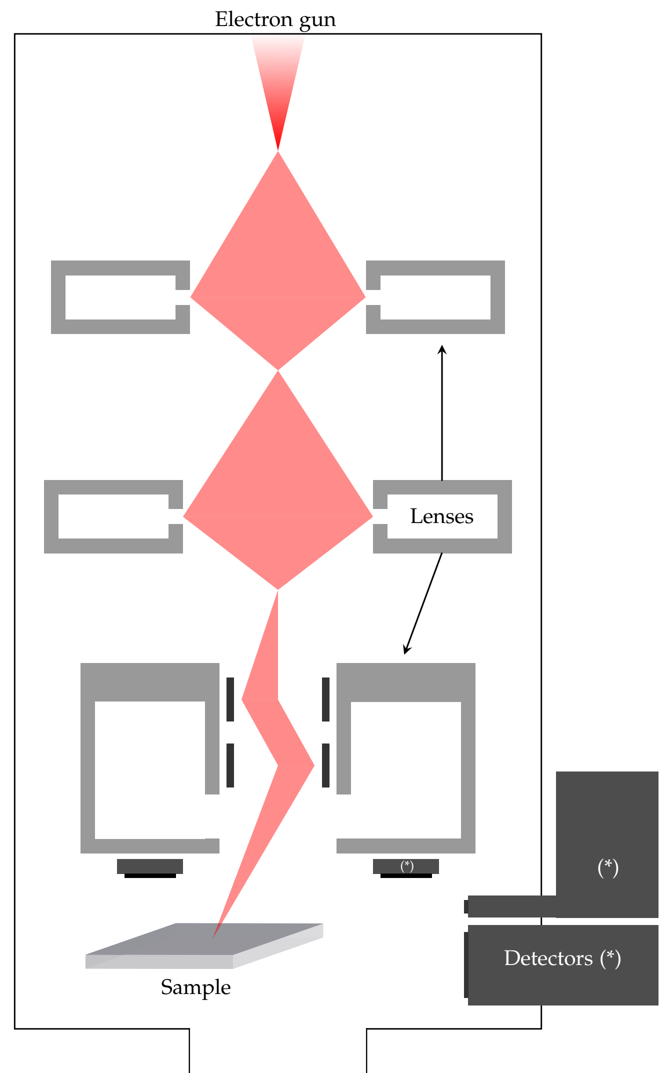

Figure 3.7: Schematic illustration of scanning electron microscope.

In order to fully understand the principles of SEM one needs to look into the various emissions that occur once the electron beam hits the sample. The two most important emissions are created by backscattered and secondary electrons. The incident beam of electrons emitts electrons by either backscattered or secondary electrons. Firstly, backscattered electrons (BSE) are electrons which are scattered by the crystal structure of the sample. BSEs can occur at half the penetration depth of the initial electrons, around several hundred nanometers. BSEs give an elemental contrast due to its Z-dependency (see section 3.1.1). Large atomic number yields a higher scattering angle than a low atomic number. It is thereby possible to distinguish the large angle scattering from the low scattering angles in the BSE-detectors, giving a contrast image which is dependent on the Z-number. Secondly, secondary electrons (SE) are created by ionized atoms and originate from near-surface regions of the sample. The initial electron beam ionizes the atom within the sample, and the ejected electrons get detected by the SE-detector. Usually, the SEs have a significantly lower energy than the BSEs, meaning that SEs generated deep within the sample does not have sufficient energy to escape the sample. Therefore, SEs are usually detected near the surface of the sample in contrast to BSE. The SEs then provides information about the surface structure of the sample, the topography, and does not provide information about the elemental composition. The penetration depth of the primary electrons are dependent on two main factors. (i) The primary electron energy, given by the acceleration voltage. An increase in acceleration voltage increases the

interaction volume with the sample. (ii) The density of the material also influences the penetration depth, a high density material would decrease the penetration depth, and vice versa. In addition to detecting electrons, SEM is also equipped with an appropriate detector capable of performing energy dispersive x-ray spectroscopy (EDX). The principles of EDX are discussed in section 3.1.3.

There are multiple factors to adjust in order to increase spatial resolution in SEM. The main factors which are crucial are acceleration voltage and probe current. The acceleration voltage affects the initial electron beam energy, one needs to be careful when managing the acceleration voltage, as excessive voltage may damage the sample. On the other hand, too low acceleration voltage yields a low image resolution. The probe current affects the number of incident electrons on the sample per unit time. As for the acceleration voltage, there is a balance between low and high probe current in order to achieve optimal image resolution.

3.4 Photoluminescence Spectroscopy

Photoluminescence (PL) spectroscopy is a characterisation technique which is widely used for its brilliant determination of optical properties for semiconductors. This section will briefly mention the important and rich physics intervened in PL, where the fundament is laid in chapter 2, section 2.4 . The measurements presented in this thesis were done my Dr. Augustinas Galeckas, and due the sample under investigation, micro-PL technique was utilised for its improved spatial resolution. This section is based upon the review article of Gilliand, [47].

The underlying principles of PL are already mentioned in chapter 2, however, we will redirect this information towards PL. Photoluminescence is subject to radiative and non-radiative processes, see subsection 2.4.3. Assuming only radiative transitions occur, Fermi's Golden Rule mentioned in subsection 2.2.2, determines the radiation rate as a product of density of lower empty states and density of carriers in higher energy states. One would assume that there is no difference between absorption and emission, as they are counterparts of one another. Absorption is often descriped as the mean free path of an incident photon decay. Whereas, emission is often described as the photon generation per unit volume. The incident photons directed towards the sample gets absorbed to some extend - which could lead to a broad emission band as the absorbed photon energies may be dispersed in energy. These absorptions excite electrons to higher energy states, dependent on the band structure and the nature of the transition. As mentioned in subsection 2.4.3, recombination processes by radiative transitions lead to an emission of electromagnetic radiation. These photons generated by the absorption is detected by a photomultiplier tube and is compiled as an intensity (counts/s) as a function of photon energy (eV) dataset.

The usual graphical presentation of Photoluminescence measurements is a simple graph containing the intensity of photons detected as a function of photon energies. As mentioned previously, we also have intra- and interband transitions, see subsection 3.1.2, as well as defect states present within the bandgap. These are all possible to detect through Photoluminescence Spectroscopy, as one may observe prominent emission bands consistent with a defect states, or the optical bandgap. The curvature of the band structure influences the measured intensity significantly, as well as the energy location of the emission band, and a keyword is band nesting, as mentioned in subsection 3.1.2. Furthermore, it is also possible to detect and observe Spin-Orbit coupling, discussed in subsection 2.4.4, and also exciton binding energies, discussed in section 2.4.

Chapter 4

Group IV-VI: GeSe - In light of TEM & PL

4.1 Crystal structure & properties

Two dimensional materials such as ,graphene and transition metal dichalcogenides (TMDCs) have unique properties [20, 21, 48, 49]. Furthermore, GeSe, which is the scope of this thesis also has some abnormal qualities as one reaches two-dimensional structure. These qualities are enhanced optical properties as one goes from indirect to direct bandgap from quantum confinement as well as thermal and electrical changes. GeSe is of interest for many scientists, due to its high stability, earth abundant constituents, environmental friendliness as well as many similar properties of other TMDs. Germanium and Selenium have densities of $5.32 g/cm^3$, $4.82 g/cm^3$ and electron configurations: $[Ag]3d^{10}4s^24p^2$ and $[Ag]3d^{10}4s^24p^4$, respectively.

As reported by Zhang et al.,[50] there are five polymorphs of GeSe monolayer - α-GeSe, β-GeSe, γ-GeSe, σ-GeSe and ϵ-GeSe. However, to the best of my knowlegde, only α, $-\beta$ have been realised experimentally. These structures are layered, as the usual TMDCs, but consist of elements in group IV-VI, meaning the typical monochalgonides are $SnSe$, SnS, $GeSe$ and GeS. GeSe has a phosphorus crystal structure which is orthorhombic. Furthermore, the most stable phase of GeSe is the α-GeSe [50]. A brief introduction of the structural arrangement of GeSe, optical properties and other properties will be discussed. Furthermore, we will see how plasmons behave in GeSe.

In figure 4.1 a visual representation of the α-GeSe crystal structure as well as irreducible Brillouin zone of the orthorhombic structure. In figure 4.1a) we see the layered structure of GeSe, showing zigzag chains along the single GeSe layers. As discussed in chapter 2 the layers are bonded together through van der Waals forces with an interlayer binding energy. In order to mechanically exfoliate layered structured material one needs to overcome the van der Waals interlayer binding energy. Experimental and theoretical studies of these forces have been applied to a number of TMDs, showing an interlayer binding energy of

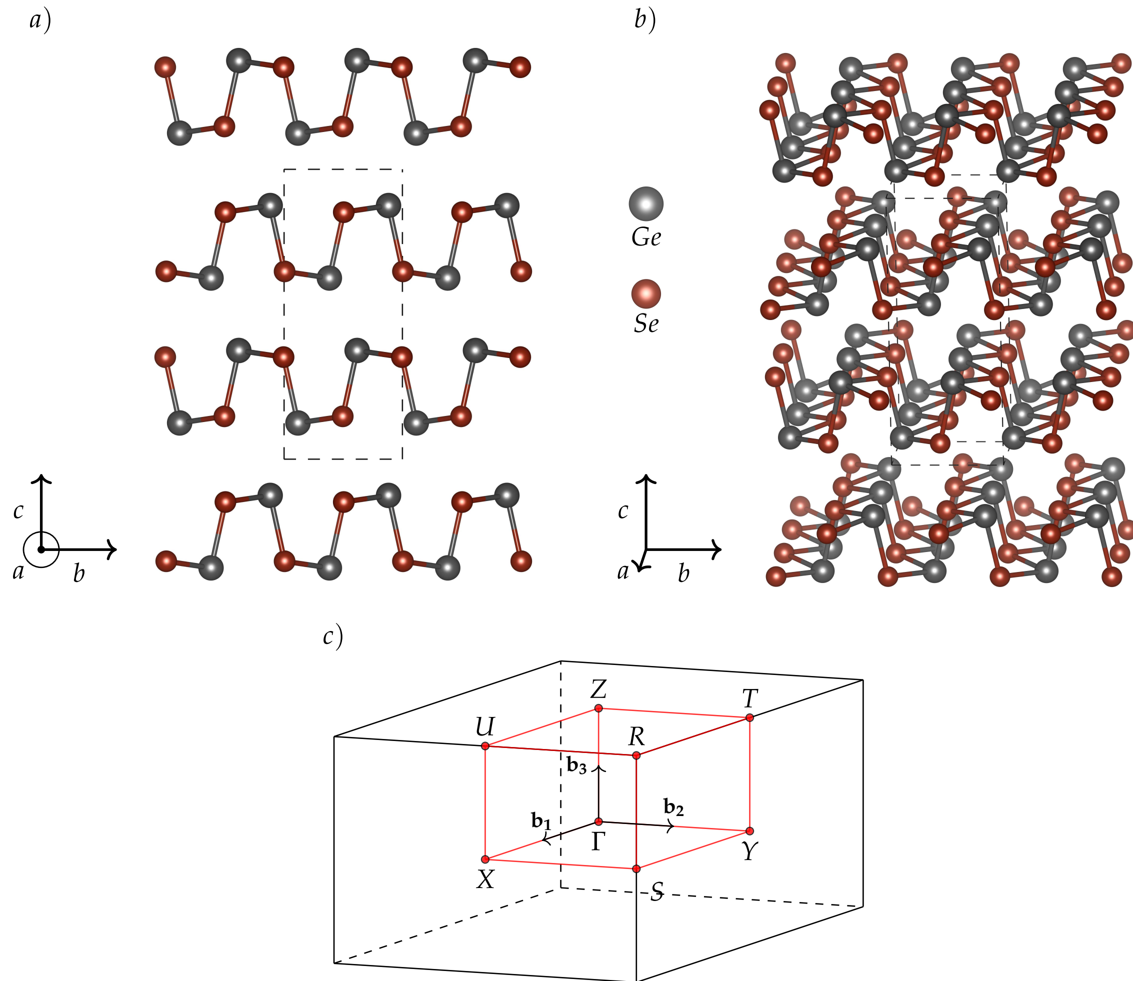

Figure 4.1: Visual presentation of the crystal structure of α-GeSe with the use of software VESTA [51] a) b) c) Irreducible Brillouin zone of 1.st Brillouin zone of orthorhombic structure in three dimensions. Showing special symmetri points along the sides and edges

about 13-21 meV/Å^2 [21]. In this work we analyse synthesized GeSe, and not mechanically exfoliated. The GeSe interlayer binding energy has been calculated as a function of interlayer distance (d) [1][52], and they suggest that monolayers of GeSe is obtainable through mechanical exfoliation. Where the interlayer binding energy was calculated to be 15-40meV/Å^2 when the interlayer distanced varied from 1.0-3.0Å.

In table 4.1 a number of material-dependent values are displayed through a number of articles. The main propose of this table is to show the variation in reported values across multiple articles as well as give a good overview over the to main phases α, β in bulk and monolayer. Interestingly, in bulk GeSe the reported space group is Pnma, with one article reporting a Pbnm structure, and once we have a monolayer, we see reports of space group Pmn2_1. The lattice vectors reported are relatively close in value within one phase, which amplifies the validity of the experimental values. The interlayer distance reported for

[1]Interlayer distance is the distance between every subsequent monolayer. Usually, a monolayer is defined by the intralayer distance plus the interlayer distance.

Table 4.1: Table of α & β - GeSe, showing space group, lattice vectors (a,b,c), interlayer distance (d), calculated fundamental bandgaps (E_g^{HSE}, HSE hybrid functional) for bulk and monolayers.. The star (*) indicates direct band gaps.

Phase	*Space Group*	a [Å]	b[Å]	c[Å]	*d*[Å]	E_g^{HSE} [eV]
			Bulk			
α-GeSe	Pnma,Pbnm[53,54]	4.4-4.5[53,55]	3.8-3.9[53,55]	10.84-11.31[53,55]	3.37[53]	0.6-1.38[53,55,56]
β-GeSe	Pnma[53,54,57]	8.1[53]	5.8[53]	3.8[53]	2.60-3.27[3,53]	0.5[53]
			Monolayer			
α-GeSe	$Pmn2_1$[54,58]	4.26-4.30[55,58,59]	3.97-3.99[55,58,59]	–	–	1.16-1.66*eV[4,52,54,55,59]
β-GeSe	$Pmn2_1$[54,57,58]	5.90-5.91[57,58]	3.66-3.67[57,58]	–	–	2.47-2.93[57,58]

bulk α, β-GeSe is in the range $d = 2.60 - 3.37$Å. Furthermore, a number of bandgap measurements through DFT calculation has been conducted, where they used a HSE hybrid functional. HSE hybrid functionals is know for overestimating the fundamental bandgap to some extend. What is important here is the clear increase in bandgap as one goes from bulk to two-dimensions, as well as the sharp increase in bandgap from α to β-GeSe. In α-GeSe we have a transition from indirect to direct bandgap as one goes from bulk to two-dimensions as well, which is compatible with literature of many two-dimensional materials [20, 21].

As well as many calculated values of the bandgap through the powerful algorithms of DFT, there has also been experimental values assembled. One of the greatest technique to measure optical bandgaps is through photoluminescence. As we know that there has been difficult challenges in producing pure two-dimensional GeSe. There has been a report of GeSe triangular nanoplates showing a bandgap of E_g = 1.246eV, at estimated thickness from AFM to be 44nm [60]. This would still be considered bulk, and bandgap as a function of thickness would still be plausible. The value of 1.246eV would then be attributed to bulk GeSe. The article *"Two-Dimensional GeSe as an Isostructural and Isoelectronic Analogue of Phosphorene: Sonication-Assisted Synthesis, Chemical Stability, and Optical Properties"* [3], were able to control the thickness of GeSe-flakes through varying the centrifugal speeds. They showed a variation in bandgap as a function of thickness to some extend. The reported values of bandgap was E_g = 1.08-1.53 eV. From bulk to four sheets of GeSe ($\sim 2nm$), where a monolayer was reported to be 0.54nm. Lastly, brute force methods have also been applied in order to achieve two-dimension in GeSe [8], here they laser thinned the GeSe sheets in order to achieve an average thickness of 1.5nm, and achieved a broad PL-spectra with eight continuous peaks located at $\approx$ 2.105, 1.893, 1.682, 1.494, 1.199, 1.053, 0.944, and 0.852 eV.

4.2 Determining topography of GeSe

In order to get a good overview of the sample under investigation, pure topography analysis is performed. Scanning electron microscope as well as optical microscope images are taken in order to get a 'feel' of what we are working with. Furthermore, the flake sizes along the elongated direction are measured. In addition to optical images, SEM images reveal potential binary phases which will be analysed further in section 4.3 . Lastly, we present AFM- images of what is believed to be GeSe. These AFM-images are analysed and a variety of thicknesses is observed within a single flake.

4.2.1 SEM & optical microscopy of layered structure

The sample under investigation is purchased from *2dsemiconductors Inc* and contains GeSe mono-and few-layer thick flakes dispensed in isopropanol (IPA). In order to examine the layered structure the solution was deposited on a substrate of choice. Under this section, the GeSe solution is deposited on a 1x1cm Si-substrate. We kept the original solution pure, with no additional IPA applied for thinning purposes. A cleaned Si-substrate [2] was used. The GeSe solution was transferred to the cleaned Si-substrate by a pipette. Typically, 3-4 droplets of GeSe solution was transferred, for high density of GeSe flakes.

To get an overview of concentration as well as size of GeSe flakes contained in the dispensed solution, optical images were taken in order to give an approximate understanding of concentration and size. The optical microscope used was an Olympus BX 41 M. All images are at 100X magnification power. In figure 4.2 four optical images of GeSe deposited on Si-substrate are presented. All four images are from the same substrate, and in close vicinity to each other. The GeSe flakes was inhomogeneously distributed across the Si-substrate. The location depicted in the four optical images were the highest density locations on this particular sample. At this high density location, one can clearly see a reasonably homogenous distribution with the small exception of figure 4.2b).

In addition to optical images, we performed high resolution SEM images. SEM images permits a better resolution than optical microscopes, contributing to a more in depth understanding of the surface structure of GeSe. The SEM used was a JEOL IT-300. As seen by figure 4.3, two images with 5 and 10 microns inset bar were acquired. These images differs somewhat by the phases occurring. In 4.3a) we see a potentially pure GeSe flake, as evidence by EDX in subsection 4.3.1. This image provides an excellent overview of the structure presented by GeSe. We can clearly see a layered structure as

[2]Basic cleaning procedure; Si-substrate washed in IPA for 2-3min and then displaced in ultrasonic water for another 2-3min. Thereafter, Si-substrates was rinsed of with deionized water for additional 2-3min. Finally, the Si-substrate was dried by N_2

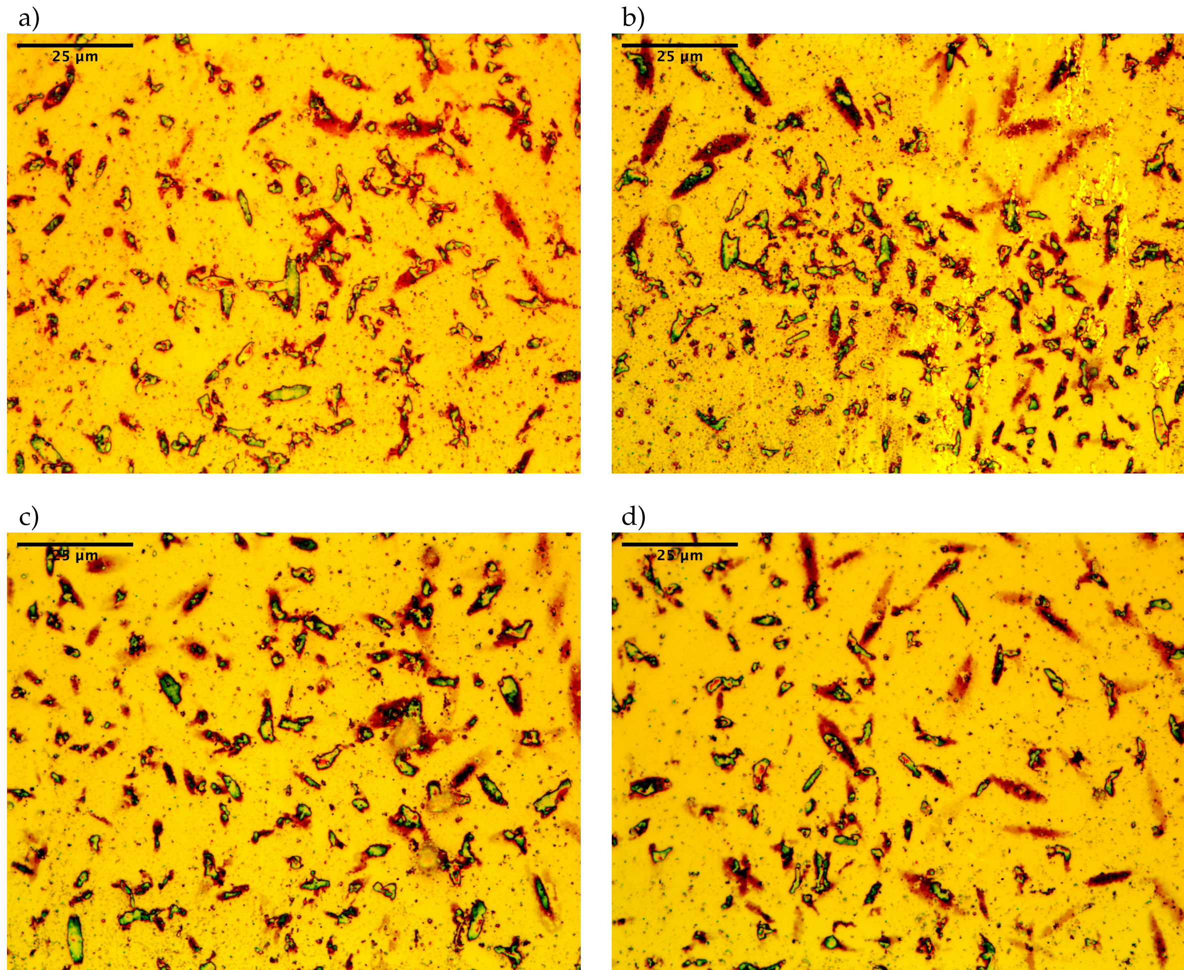

Figure 4.2: Microscopic image of GeSe on a 1x1cm Si-substrate. Inset bar is at 25μm. Every picture is taken in close vicinity to each other.

predicted for two-dimensional materials. It is fair to assume that this flake is not two-dimensional, it is rather in the bulk regime. However, towards the left side of the flake, one can see a minimised thickness. From the left side towards the centre, one can observe a clear step-wise increase in thickness as multiple layers of GeSe is applied. From figure 4.3a) it is hard to see any clear impurities or other phases present. From figure 4.3b) we can see a different SEM image with an approximately identical GeSe flake amongst an accumulation of needles and other irregularly shaped particles. This sample was provided by a previous batch of GeSe solution from *2dsemiconductors Inc* which was deemed impure due to the accumulation of different phases arising from thermal fluctuation during travel. These different phases occurring are nonetheless interesting, and we will determine the elemental composition as well as plasmon peak dependency as a function of phases. This will become subject of section 4.3.

To estimate the average size of the deposited GeSe flakes, a thorough analytical process of measuring each individual flake was used. From the optical images seen by figure 4.2, plus one additional site, we measured each individual flake along the elongated direction in

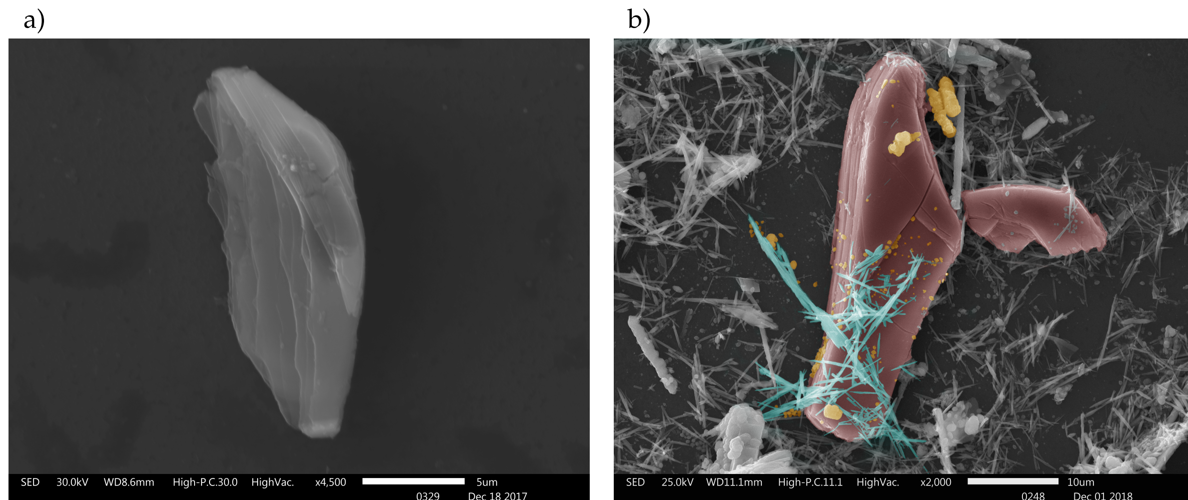

Figure 4.3: Scanning Electron Microscope image of GeSe from GeSe dispensed in isopropanol solution deposited on a 1x1cm Si-substrate. a) Image of pure GeSe flakes. One can clearly see the layered structure as anticipated. b) Accumulated region from another GeSe dispensed isopropanol solution. This show some binary phases differentiated by the colours orange and cyan, and GeSe flake coloured red. These binary phases will be addressed in subsections 4.3.2 and 4.3.3.

order to get an overview of the size. Measurements were done manually across 525 GeSe flakes seen in the optical images. The aim of this analytical process is not to get defined and exact data, but rather an estimate. Once the 525 data points were collected we could see the distribution of size. In figure 4.4 a histogram of the collected data points is shown. Flake-size collected was estimated to have a mean value of 3.049μm along the elongated direction with the standard deviation estimated to be σ=1.821μm. This show a rather large 'spread' of estimated size of the flakes along the elongated direction.

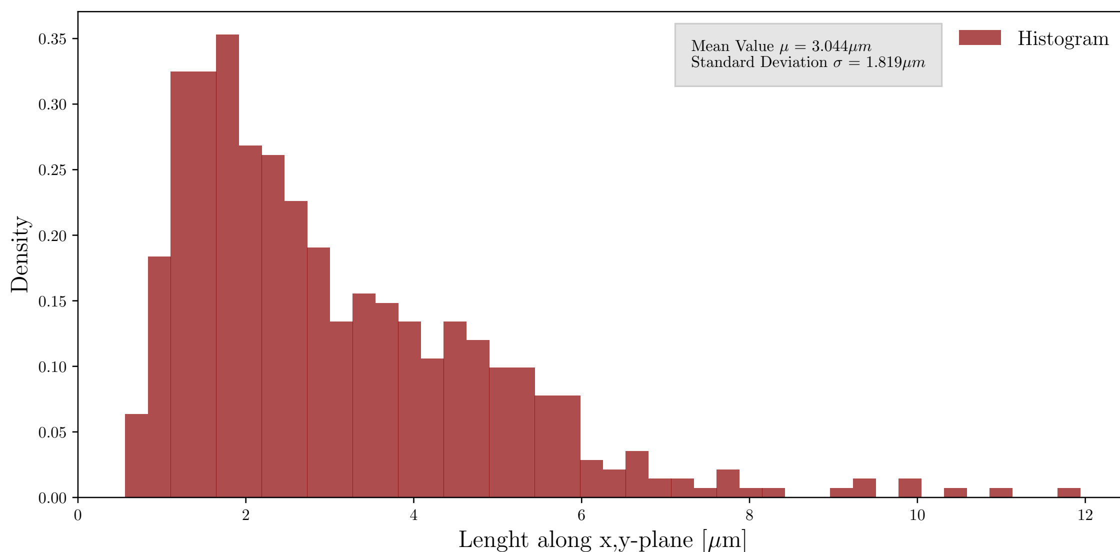

Figure 4.4: Histogram distribution of flake sizes. Values extracted from optical images along the elongated direction of each individual flake. Mean value from 525 data points from five different locations on sample is 3.049μm with a standard deviation $\sigma = 1.821\mu m$.

4.2.2 AFM-result of GeSe layered structure

Further analyses of the GeSe topography is presented here, through the technique of AFM. In order to give an overview of the thickness of the GeSe flakes distributed, AFM was performed. There is a great technical challenge to image pure two-dimensional materials through AFM. Sensitive measurements needs to be taken in order to see an atomic sheet down to 0.5-1.0nm. In this subsection we present two AFM-images from two distinct locations on GeSe deposited on Si-substrate. Si-substrate was the substrate of choice due to its fine surface structure, allowing a more accurate measurement of GeSe. The AFM used was a Veeco Dimension 3100.

In figure 4.5 we see the first AFM images, where the size of the flake is well within the margins of estimated values of the flakes elongated direction. As seen by the topography images 4.5a,b) the images are contaminated with periodically displayed spots. These spots

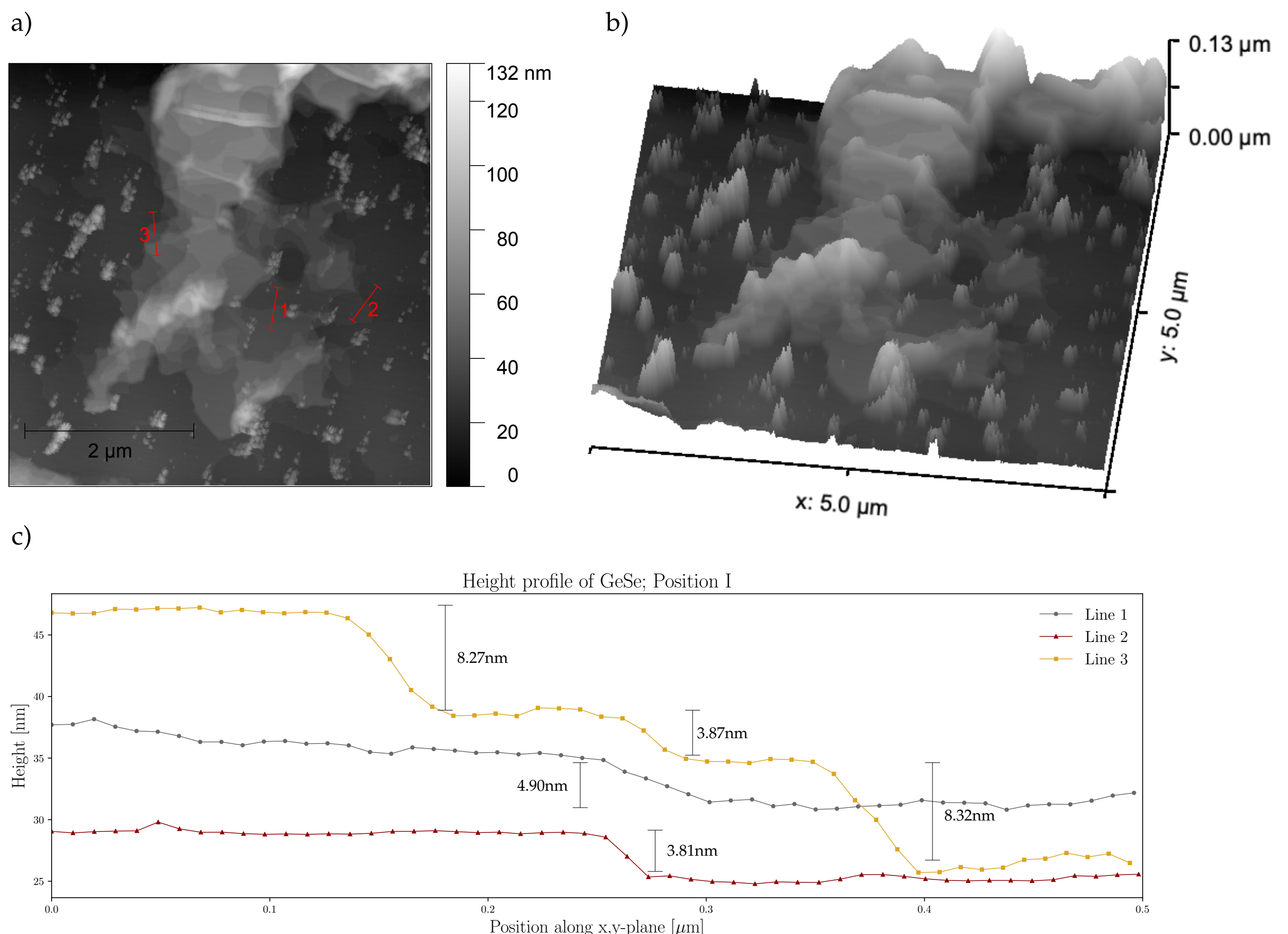

Figure 4.5: Topography image using AFM - from flake 1. a) 2D image of potential GeSe, with colorbar displaying thickness in nanometer. Red lines indicate the line profiles in c). b) 3D image of the same flake, where the z-axis is in the range of 0-132nm c) Thickness profile from the line profiles in a), with thickness of the layers inserted.

may be due to contamination of the AFM-tip. As the tip is scanned across the sample surface, it may pick up loose impurities and contaminate the produced image. One could by this assume that these spots are created by the contaminations of the AFM probe and are not representative to the real surface. Furthermore, line profiles were extracted from the images in order to examine the thickness profiles along certain directions. In figure 4.5a) we see three line profiles labeled 1,2 and 3. These three line profiles were placed along the location of the thinnest step-size available at this flake. In figure 4.5c) we see the thickness profiles belonging to the lines in 4.5a). The thickness was estimated by calculating the average thickness from each layer in the line profiles and subtract the lower layer to get the thickness. Line 1, gives a unsharp step of about 4.90nm. By following the reported

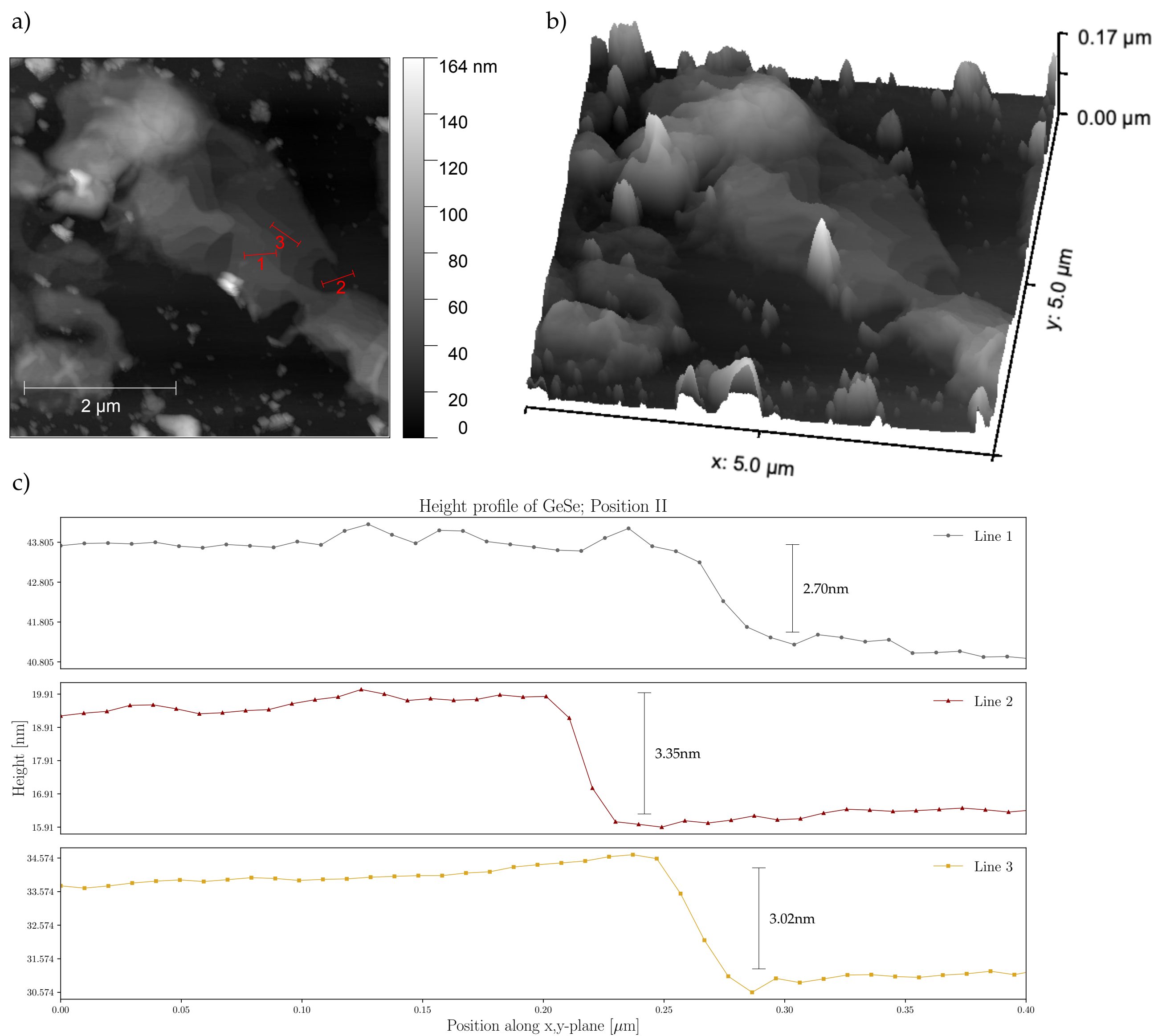

Figure 4.6: Topography image using AFM - from flake 2. a) 2D image of potential GeSe, with colorbar displaying thickness in nanometer. Red lines indicate the line profiles in c). b) 3D image of the same flake, where the z-axis is in the range of 0-164nmc) thickness profile from the line profiles in a), with thickness of the layers inserted.

monolayer thickness of 0.54nm [3] and the interlayer distance of $d = 2.60 - 3.37$Å, this is equivalent to a stacking of ~6 monolayers. Line 2, show a sharp step of 3.81nm, ~4 monolayers. Line 3 has three steps of $8.27, 3.87$ and 8.32nm which corresponds to ~ 10, 5 and 10 monolayers, respectively.

On the same sample we performed another AFM-image on another location. We were able to detect another flake with the same kind of structural shape as in figure 4.5. In figure 4.6, however, the remnants on the tip is removed by the use of a new AFM probe. The same procedure is conducted here, as in figure 4.5. In this flake there seems to be smaller steps in the layered structure, as seen by figure 4.6c) the steps is consistently in the range of $2.70 - 3.35$nm. Where line 1 has a step of 2.70, ~3 monolayers. Line 2, has a step of 3.35nm, ~4 monolayers, and line 3 has a step of 3.02nm, ~4 monolayers.

4.3 Transmission Electron Microcopy results (TEM)

In this section Transmission Electron Microscopy will be utilised. To further our understanding of GeSe as well as the peculiar binary phases occurring in our sample STEM, EDX and EELS will be used. We dive in to three main regions consisting of three different elemental compositions. The three phases under study are named GeSe flake (flake morphology), Ge-rich (random morphology) and Se-rich (Needle-like morphology), corresponding to figure 4.3b). The main goal in this section is to determine the exact elemental composition and the behaviour of plasmon peaks as a function of thickness in pure GeSe and plasmon peaks as a function of chemical variations (phases). In order to achieve the correct plasmon peaks dependencies, we will firstly investigate the sample through STEM and EDX. Then, once the phases and thickness are established we will move on to EELS measurements. The experiments were performed in a FEI Titan G2 60-300 kV STEM, equipped with a probe-corrector. Supplementary information of specific positions of EELS measurements, Low-loss spectra, python scripts, as well as calculated thickness profiles for GeSe flake is found in Supplementary Information[3]

4.3.1 STEM & EDX of GeSe (flake morphology)

We examined regions exhibiting three characteristic morphologies: flake, random and needle-like. Starting with GeSe flake, STEM images are shown in figure 4.7. The images show three different modes of STEM, a) Annular Dark Field (ADF), b) High Angle Annular Dark Field (HAADF) and c) Annular Bright Field (ABF). Close to the edges within both GeSe_ROI_1 and GeSe_ROI_2 there is a slight decline in intensity in the HAADF image. As we know from subsection 3.1.1, the HAADF image is pure Z-contrast, and the decrease in intensity in HAADF image could point to a lower concentration of Selenium (Z=34) in comparison to Germanium (Z=32). However, as the Z-numbers does not differ much, the intensity difference could be an indication of lower thickness of the sample. All further results are in the vicinity or in the marked regions, named, GeSe_ROI_1 and GeSe_ROI_2, as seen by the figure 4.7d).

A High resolution STEM-image is taken within GeSe_ROI_2 as seen in figure 4.8a), and the corresponding Fast Fourier transformation (FFT) in b). The colored rectangles in a) are line profiles along four different directions. Intensity profiles were collected from the given rectangles yielding a way of estimating the lattice spacing, the intensity profiles are available in Supplementary Information. The IP_1 intensity profile gave a lattice spacing of 0.284nm which is consistent with the (111) plane of GeSe, and IP_2 gave a lattice spacing of 0.289nm which matches the (011) plane of GeSe [3]. Furthermore, the intensity profiles of IP_3 and IP_4 yielded lattice spacings of 0.382nm and 0.429nm, respectively. These measurements may be attributed to (010) [0.382nm] and (001) [0.429nm] planes [7]. In figure 4.8b) a Fourier

[3]Supplementary Information is provided through the link: https://github.com/Kristopy/The-Effect-on-Plasmon-Peaks-in-Quasi-Two-Dimensional-GeSe-by-Variation-in-Thickness-Phases.

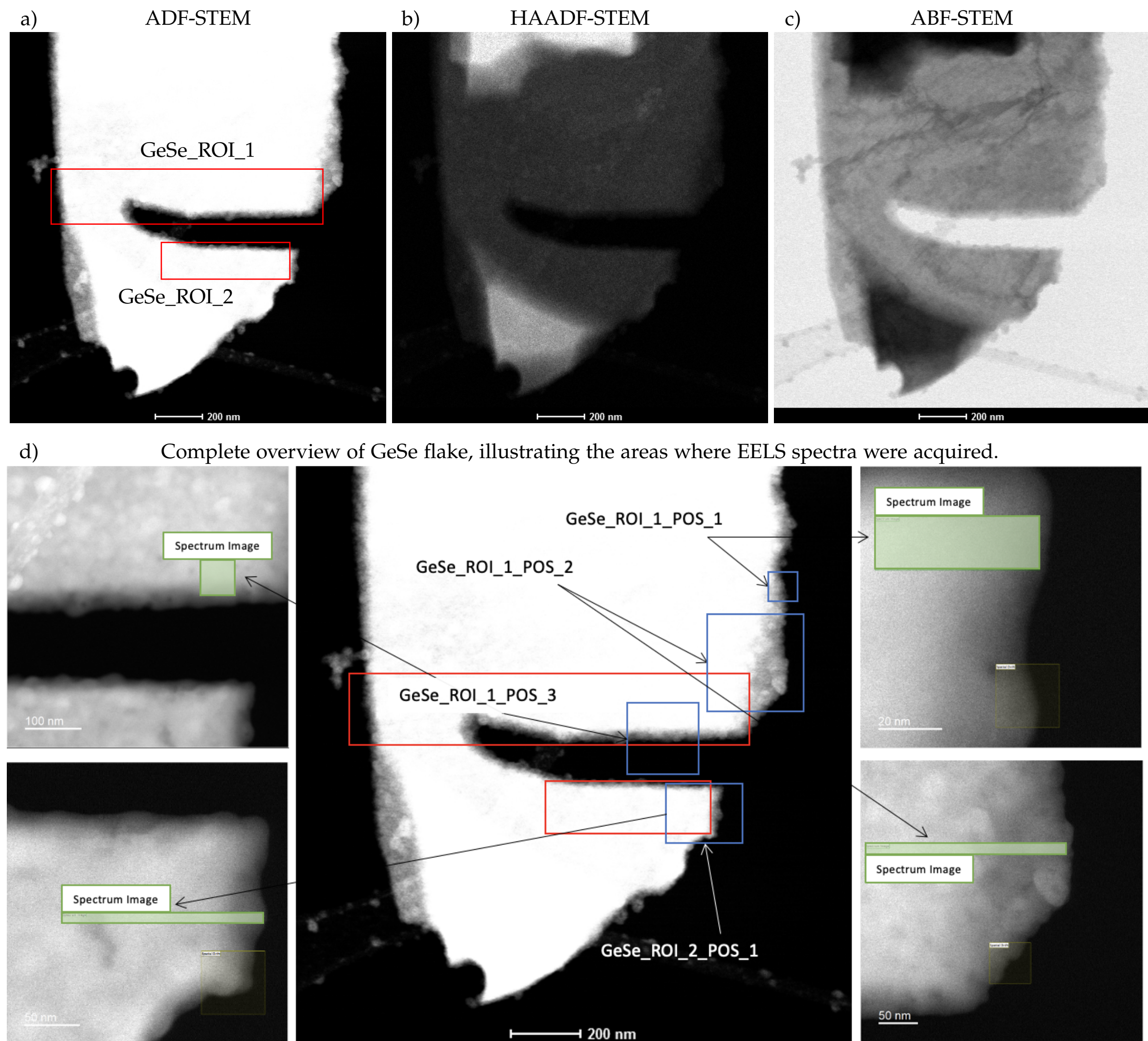

Figure 4.7: STEM image of GeSe flake and regions of interest (ROI) - GeSe_ROI_1 and GeSe_ROI_2. a) Angular Dark Field (ADF) image taken with STEM, showing regions of interest. b) High Angle Annular Dark Field (HAADF) image. c) Annular Bright Field image (ABF). All scale bars in a,b,c are at 200nm. d) A complete overview of EELS spectra obtained at four different location on GeSe flake.

transformation of the same STEM image in a) is shown, and the subscripted vectors were measures through intensity profiling as in a). Where we measured; $\mathbf{b_1} = 5.26$ 1/nm and the orthogonal vector $\mathbf{b_2} = 4.62$ 1/nm. $\mathbf{b}_3^1, \mathbf{b}_3^2$, was approximately the same with measured values of 3.51 and 3.52 1/nm.

In order to determine the atomic concentration we performed EDX to the main regions marked in figure 4.7a). These regions of interest are the regions where we perform EELS measurements as well (with some minor discrepancies seen in Supplementary Information). In order to determine the plasmon peaks as a function of phases we firstly need to determine the atomic concentration. As seen in figure 4.9a,b) an EDX-map of Ge and Se is shown. A rather homogeneous distribution of Ge and Se is observed. In addition to measuring the atomic concentration deep within the flake, we also performed measurements towards the edges (annotated by transparent boxes).

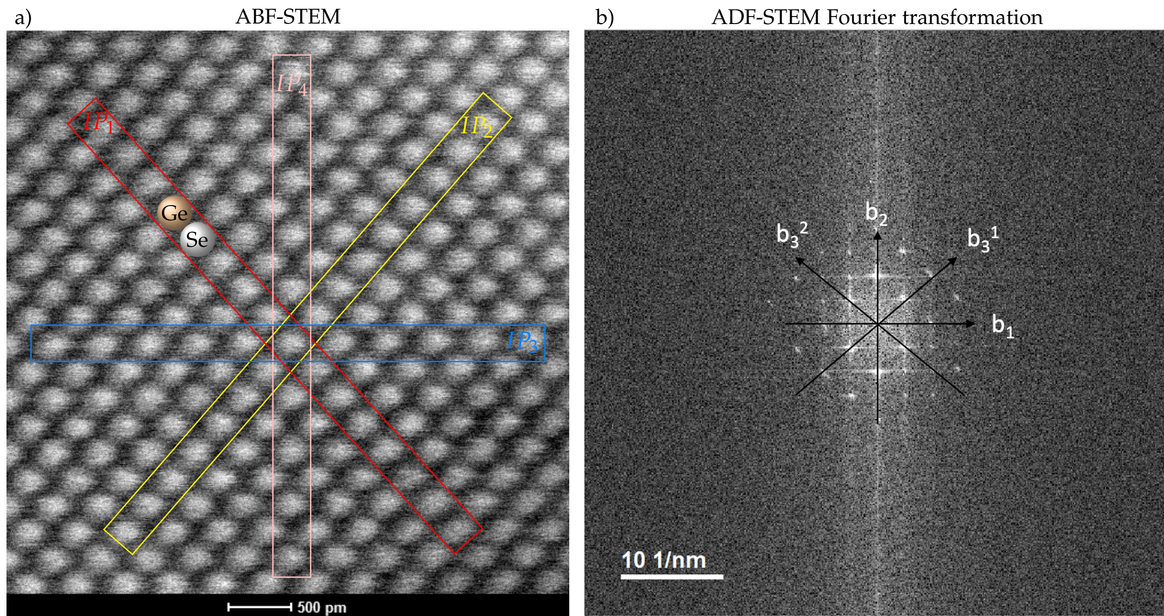

Figure 4.8: High resolution STEM-image of GeSe_ROI_2. a) High resolution HAADF-STEM image. b) Corresponding FFT.

Elemental composition within each region is provided through table 4.2. As seen, the total elemental composition in both GeSe_ROI_1 and GeSe_ROI_2 is both approximated to $Ge_{0.55}Se_{0.45}$. However, a slight Ge-enrichment at the edges is observed shown in table 4.2. The edge positions were measured such that vacuum was excluded. In the provided atomic concentration of edge position in table 4.2, oxygen is not taken into account. There is no

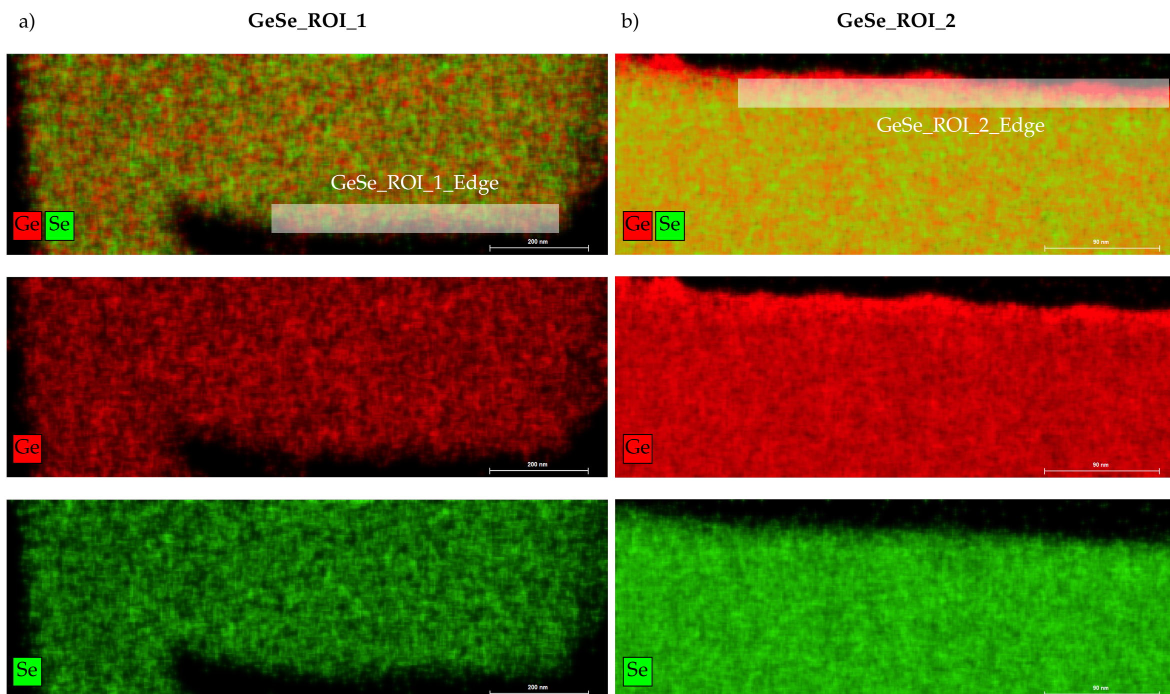

Figure 4.9: EDX quantified maps of the two regions of interest. a) EDX-maps of Ge and Se at GeSe_ROI_1, scale bar at 200nm b) EDX-maps of Ge and Se at GeSe_ROI_2, scale bar at 90nm.

doubt that oxygen is present within the sample, as seen by Supplementary Information, EDX-spectrum of both GeSe_ROI_1 and GeSe_ROI_2 is shown. The spectrum confirms the presence of oxygen within both regions of interest. There is also an intensity signal from Cu present, this is due to the TEM-grid used in sample preparations. The TEM grid is a copper grid coated with carbon.

We also defined local positions within each ROI. An overview over the positions within GeSe, is shown in figure 4.7d) as well as Supplementary Information. Multiple regions within ROI_1 and ROI_2 is analysed through EELS. Three regions analysed in ROI_1 named POS_1, POS_2 and POS_3. As well as EELS spectra collected at these positions, an estimation of the effective thickness is also collected through the method discussed in subsection 3.1.2, and will be further discussed in section 4.4.

Table 4.2: Table of elemental composition from EDX measurements. Local edge measurements GeSe_ROI_#_Edge* does not include oxygen.

	Element	***Atom. C [at.%]***	Rel. Error σ [%]
GeSe_ROI_1	Ge	**54.75**	3.14
	Se	**45.25**	3.18
GeSe_ROI_1_Edge*	Ge	**65.62**	5.76
	Se	**34.38**	7.90
GeSe_ROI_2	Ge	**54.54**	3.06
	Se	**45.46**	3.07
GeSe_ROI_2_Edge*	Ge	**79.86**	3.68
	Se	**20.14**	5.48

4.3.2 STEM & EDX of Se-rich phases (random morphology)

The second main regions under the scope of this thesis is called Se-rich phases. This region is consistent with what we saw in figure 4.3b). In figure 4.10, the images are of ADF, HAADF and ABF-STEM. Due to the weak structure we could not gather high resolution images from this region. As was done for GeSe flake, we also focus in on two regions of interest here and analyse through EELS. Mainly, our focus here is to collect the variation in elemental composition, and ultimately find how plasmon peaks varies with elemental composition.

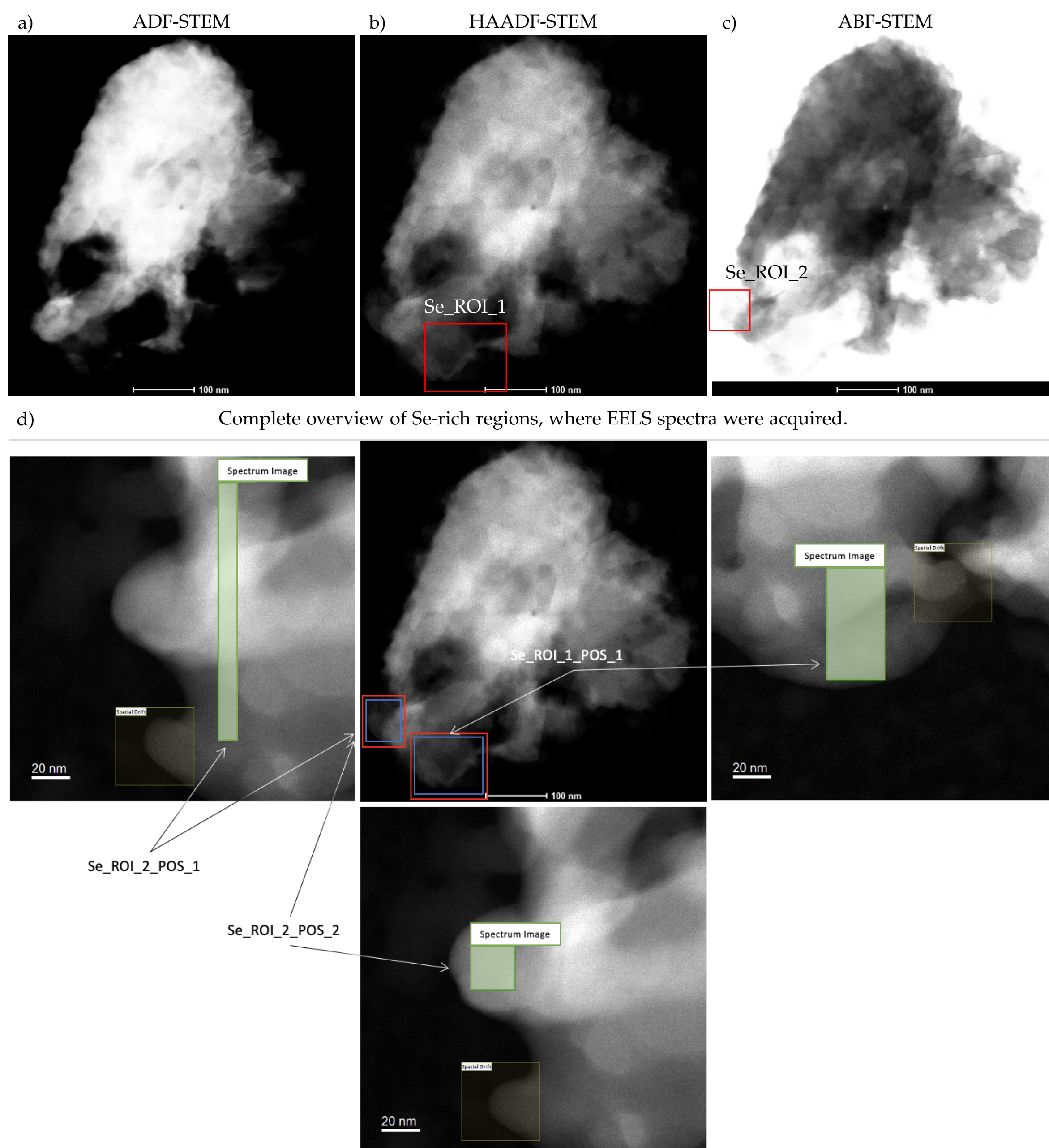

Figure 4.10: STEM image of Se-rich phases and regions of interest (ROI) - Se_ROI_1 and Se_ROI_2. a) ADF-STEM showing regions of interest. b) HAADF image. c) ABF image. All scale bars in a,b,c are at 100nm. d) A complete overview of area where we acquired EELS spectra.

Se-rich phase (ROI 1)

This is the first region of interest within the Se-rich phase. As seen by figure 4.10b) the square box indicates the position of Se_ROI_1. Only one EELS measurement were done here, named, Se_ROI_1_POS_1. The exact positions of where the EELS spectra were obtained are found in figure 4.10d). Two EDX-measurements were done here, in order to get a good understanding of the compositional nature. In the total Se_ROI_1 as seen by figure 4.11, the measured atomic concentration was $Ge_{0.14}Se_{0.86}$ (values from Table 4.3). This value indicates close to pure Selenium as an average of Se_ROI_1. Further measurements were done, and in this case they were manually placed in the vicinity of the obtained EELS spectra. As we locally varied the area of EELS spectra, we also needed to have the exact elemental composition within that exact EELS spectra location. The measured values on Se_ROI_1_POS_1 (seen in figure 4.10d)) were $Ge_{0.20}Se_{0.80}$. Here we again see a slight decrease in Selenium in the same manner as for GeSe flake along the edges. This is assumed to be due to a thinner region, and consequently a higher oxidised region because of increased surface to volume ratio.

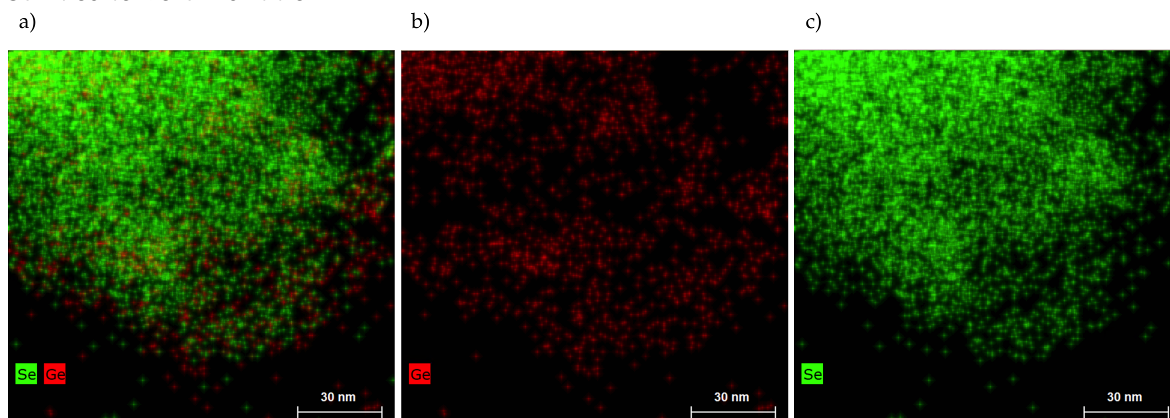

Figure 4.11: EDX maps of Se-rich phase (Se_ROI_1). All scale bars are at 30nm.

Se-rich phase (ROI 2)

The second region of interest in taken to the far left in figure 4.10c). Within this ROI, two subregions were measured through EELS. As seen by figure 4.10d), two areas of acquired EELS spectra were collected. Furthermore, in this section we will not go into detail of the collected EELS-data, specific information of the Low-loss spectra is provided in Supplementary Information and will be discussed in section 4.5.

The two regions named Se_ROI_2_POS_1 and Se_ROI_2_POS_2 show quite distinct different atomic concentration from the average EDX-map of Se_ROI_2. As we can see by the EDX-map in 4.12 there seems to be a higher density of Se near the bulk region compared to the edge (tip). On the other hand, the density of Ge is higher near the edge (tip) compared to that of the bulk. By examining the measured values from EDX-data, we see by table 4.3 that Se_ROI_2_POS_1 show an elemental composition of $Ge_{0.07}Se_{0.93}$, which is very

close to pure Selenium. Se_ROI_2_POS_2 on the other hand show a completely different atomic concentration. As mentioned previously, due to decreased thickness a superior surface-to-volume ratio favours oxidation. The result show an atomic concentration of $Ge_{0.56}Se_{0.44}$, which is nearly the same atomic concentration as seen by GeSe flake.

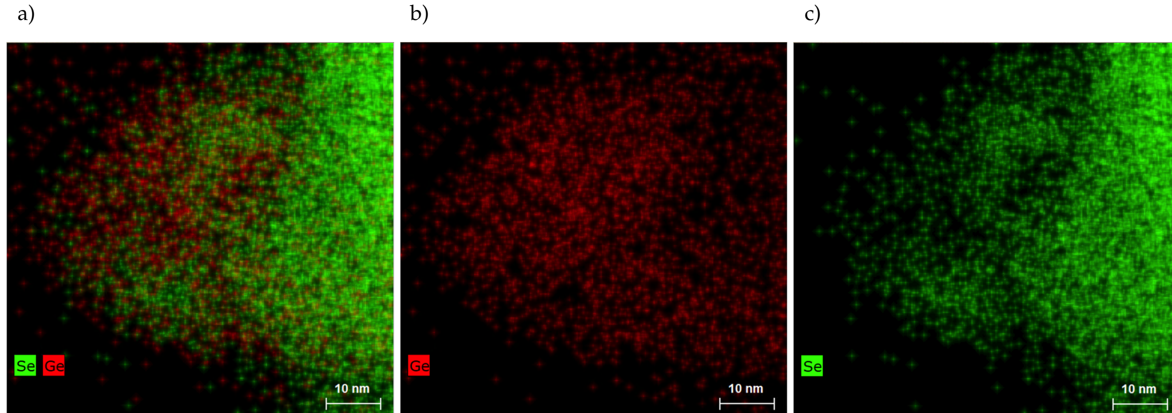

Figure 4.12: EDX maps of Se-rich phase (Se_ROI_2). All scale bars are at 10nm.

Table 4.3: Table of elemental composition from EDX measurements of Se-rich phases with some discrepencies marked with (*). Local measurements of Se_ROI_#_POS_# are included due to EELS measurements at these regions. Relative average thickness t/λ, and standard deviation σ_t.

	Element	*Atom. C [at.%]*	Rel. Error σ [%]	Rel. t/λ	σ_t [t/λ]
Se_ROI_1	Ge Se	**14.27** **85.73**	3.66 3.13	–	–
Se_ROI_1_POS_1	Ge Se	**20.36** **79.64**	5.67 3.96	0.33	0.09
Se_ROI_2	Ge Se	**32.00** **68.00**	3.28 3.14	–	–
Se_ROI_2_POS_1	Ge Se	**6.68** **93.14**	6.87 3.46	0.76	0.23
Se_ROI_2_POS_2 *	Ge Se	**56.43** **43.57**	3.74 4.05	0.83	0.02

4.3.3 STEM & EDX of Ge-rich phase (Needle-like morphology)

The final region of interest exhibited needle-like morphology. This is recalled from 4.3b) where we saw a needle-like structure. We will do here as we have done in the previous subsection, namely characterise the elemental composition in various key positions. Firstly, as seen by figure 4.3.3a-c), ADF, HAADF and ABD-STEM images is taken of the needle structure. Furthermore, we can see that the needle structure is accompanied with what looks like an accumulated region as seen previously. We divide between two regions of interest - Ge_ROI_1 and Ge_ROI_2. As we have seen previously, we divide these regions of interest in multiple subregions with designated names, ending with POS_#. In Ge-rich needle-like morphology, seen in figure 4.13d), we have four position within the two different ROIs, whereas three of them is within Ge_ROI_1, and one is from Ge_ROI_2. For exact

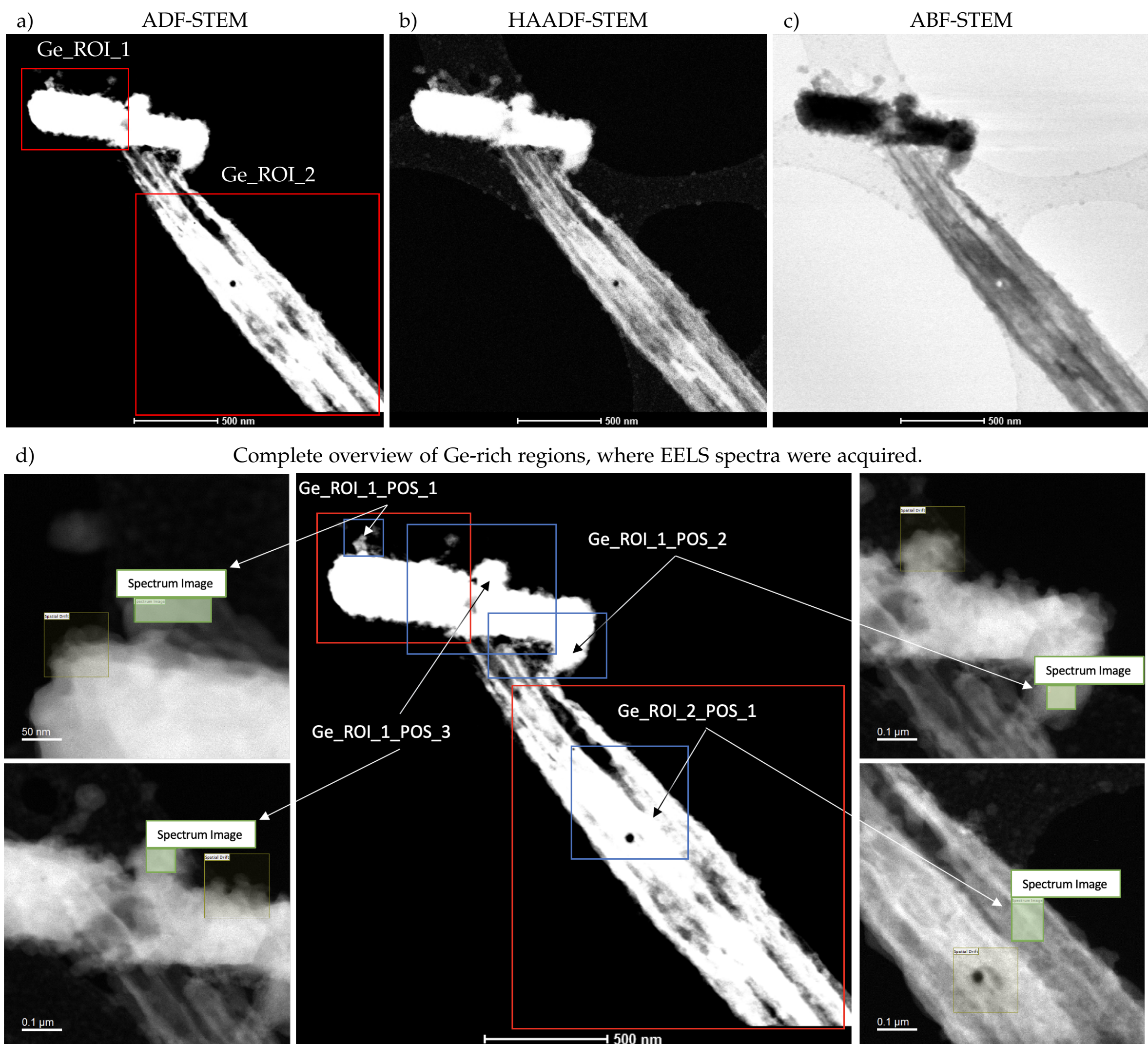

Figure 4.13: STEM image of Ge-rich phases and regions of interest (ROI) - Ge_ROI_1 and Ge_ROI_2. a) ADF-STEM showing regions of interest. b) HAADF image. c) ABF image. All scale bars in a,b,c are at 500nm. d) A complete overview of area where we acquired EELS spectra.

information of the Low-loss spectra for each distinct location provided, see Supplementary Information. Further information of the Low-loss spectra will be provided in section 4.5.

Se/Ge-rich phases (ROI 1)

We start by analysing Ge_ROI_1, and as we can see by figure 4.14, we could potentially work with a wide range of atomic concentration of Ge and Se. We analysed all regions marked in figure 4.13d), that is, all areas of EELS spectra are marked with green. For Ge_ROI_1, we analyse three regions including the entire Ge_ROI_1 seen by figure 4.14. The atomic concentration for Ge_ROI_1 is given by table 4.4. Here we find an atomic concentration of $Ge_{0.11}Se_{0.89}$, which is a Se-rich phase fairly similar to that seen in subsection 4.3.2. What is interesting is the layer-like composition of Ge and Se seen in figure 4.14. It seems like we have pure Ge and underneath we have an extension of the needle seen in figure 4.15. Nevertheless, we performed three more EDX-measurements of the three regions marked in 4.13d). Ge_ROI_1_POS_1 which is in the upper left in figure 4.14 show, non-surprisingly, an atomic concentration of $Ge_{0.94}Se_{0.06}$. Moving onwards to Ge_ROI_1_POS_2, we see a slight decline in Ge giving us $Ge_{0.91}Se_{0.09}$. The last position, Ge_ROI_1_POS_3, we seem to not measure the needle. We measure a Se-rich phase with an atomic concentration of $Ge_{0.07}Se_{0.93}$. It need to be mentioned that the relative error is significantly high during these measurements. This is mainly due to exposure time as well local estimation from a rather large spatial resolution image.

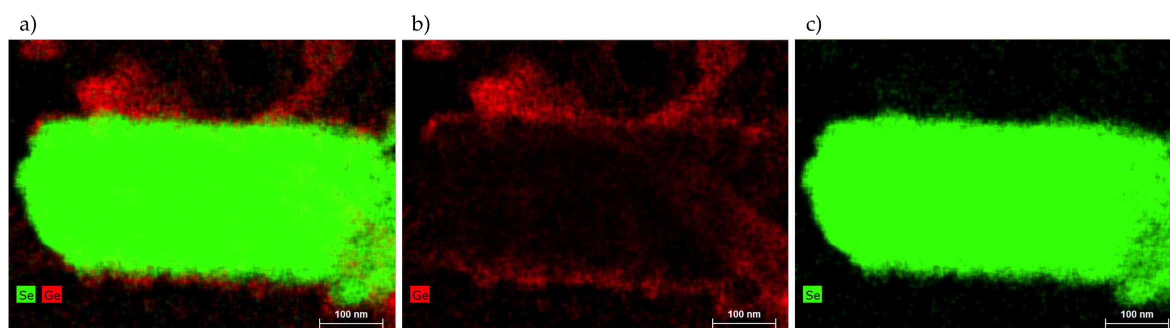

Figure 4.14: EDX maps of Ge/Se-rich phases (Ge_ROI_1). All scale bars are at 100nm.

Ge-rich phase (ROI 2)

Ge_ROI_2 is the final position analysed, as seen by figure 4.15, we mainly work with pure Germanium. Indeed, we made EDX-measurements in two locations (Ge_ROI_2 and Ge_ROI_2_POS_1) and found that the atomic concentration were almost identical $\sim Ge_{0.96}Se_{0.04}$. What is interesting by this region is the fact that the needle seems to have some peculiar structure. Further EELS measurements will be done here to see the effect on plasmon peaks. Average thickness measurements of the needle regions from the collected areas of EELS spectra show values ranging from 0.82-1.01 $[t/\lambda]$, for ROI_1, and 0.48$[t/\lambda]$

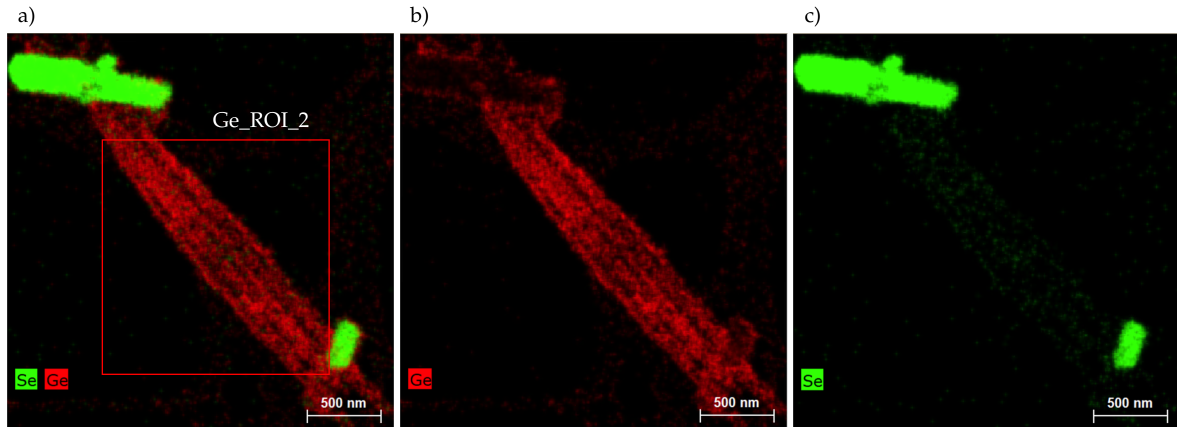

Figure 4.15: EDX maps of Ge-rich phase (Ge_ROI_2). All scale bars are at 500nm.

for ROI_2. λ is the mean free path for plasmon scattering. The typical value is in the order of 100nm, but dependency of material, energy of transmitted electrons and range of scattering angles enabled is to be expected [32].

Three main regions have been analysed through STEM and EDX. We have seen a wide range of atomic concentration throughout the three regions; Gese flake, Se-rich and Ge-rich. An overview of the elemental compositions are shown in figure 4.16. Where we have element on the x-axis and the atomic concentration on the y-axis. This wide range of elemental composition yields an intriguing oppurtionity of analysing plasmon peak energies as a function of phases. Furthermore, the average thickness of the Se-rich and the Ge-rich phases are given in tables 4.3,4.4. Further discussion will be given in section 4.5. As for now, we see that the average thickness is $\sim 76 - 101nm$ with $\lambda = 100nm$, for the two Ge and Se-rich phases, which is well within the bulk regime. We have some discrepancies for Se_ROI_1_POS_1 and Ge_ROI_2_POS_1 which show an average thickness of $\sim$ 33 and

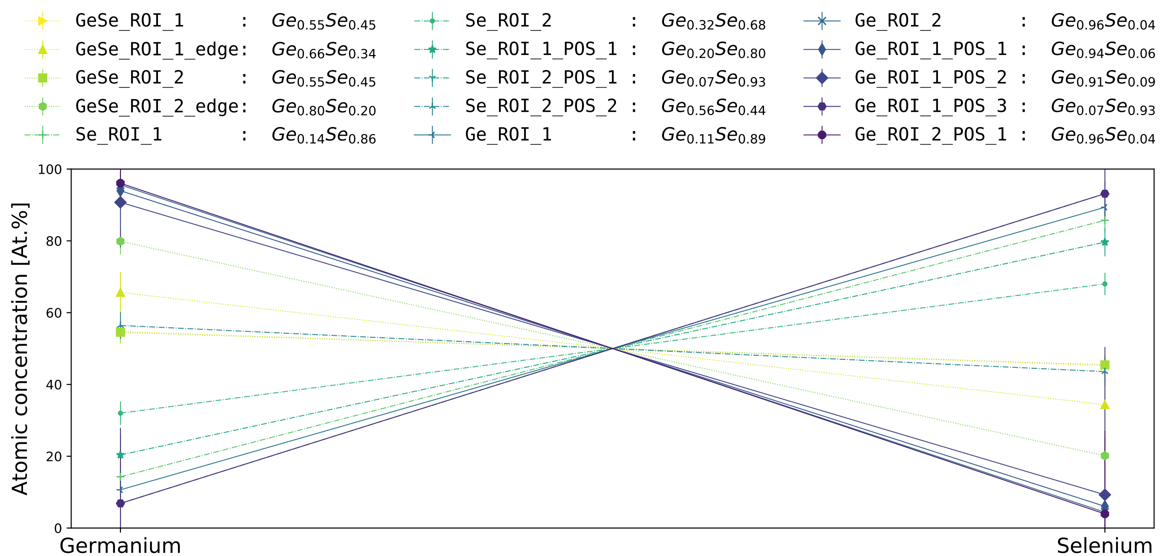

Figure 4.16: Complete overview of elemental composition of every ROI as well as POS within a ROI.

$\sim$ 48nm, respectively. These measurements will be taken into account when presenting plasmon peak energies as a function of phases in section 4.5.

Table 4.4: Table of elemental composition from EDX measurements of Ge-rich phases with some discrepencies marked with (*). Local measurements of Ge_ROI_#_POS_# is included due to EELS measurements at these regions. Relative average thickness t/λ, and standard deviation σ_t.

	Element	***Atom. C [at.%]***	Rel. Error σ [%]	Rel. t/λ	σ_t [t/λ]
Ge_ROI_1*	Ge Se	**10.65** **89.35**	3.33 3.04	–	–
Ge_ROI_1_POS_1	Ge Se	**93.96** **6.04**	5.27 18.88	0.82	0.10
Ge_ROI_1_POS_2	Ge Se	**90.73** **9.27**	12.52 41.18	0.98	0.13
Ge_ROI_1_POS_3*	Ge Se	**6.87** **93.13**	21.03 6.70	1.01	0.05
Ge_ROI_2	Ge Se	**95.59** **4.41**	3.15 5.81	–	–
Ge_ROI_2_POS_1	Ge Se	**96.05** **3.95**	5.20 23.15	0.48	0.05

4.4 Plasmonic behaviour as a function of thickness through EELS

We have by know examined the topography and elemental composition of multiple different occurring structures. Furthermore we have determined pure GeSe flake, in this section we will present and discuss the results of EELS-measurements of GeSe. The main goal is to characterise the behaviour of plasmon peaks as a function of thickness. EELS is capable of measuring the thickness as explained in section 3.1.2.

We start by analysing the acquired EELS spectra collected from GeSe_ROI_2_POS_1. The average Low-loss spectra from the entire EELS spectra is provided in Supplementary Information. In figure 4.17a) we see the familiar ADF-STEM image of GeSe flake. In

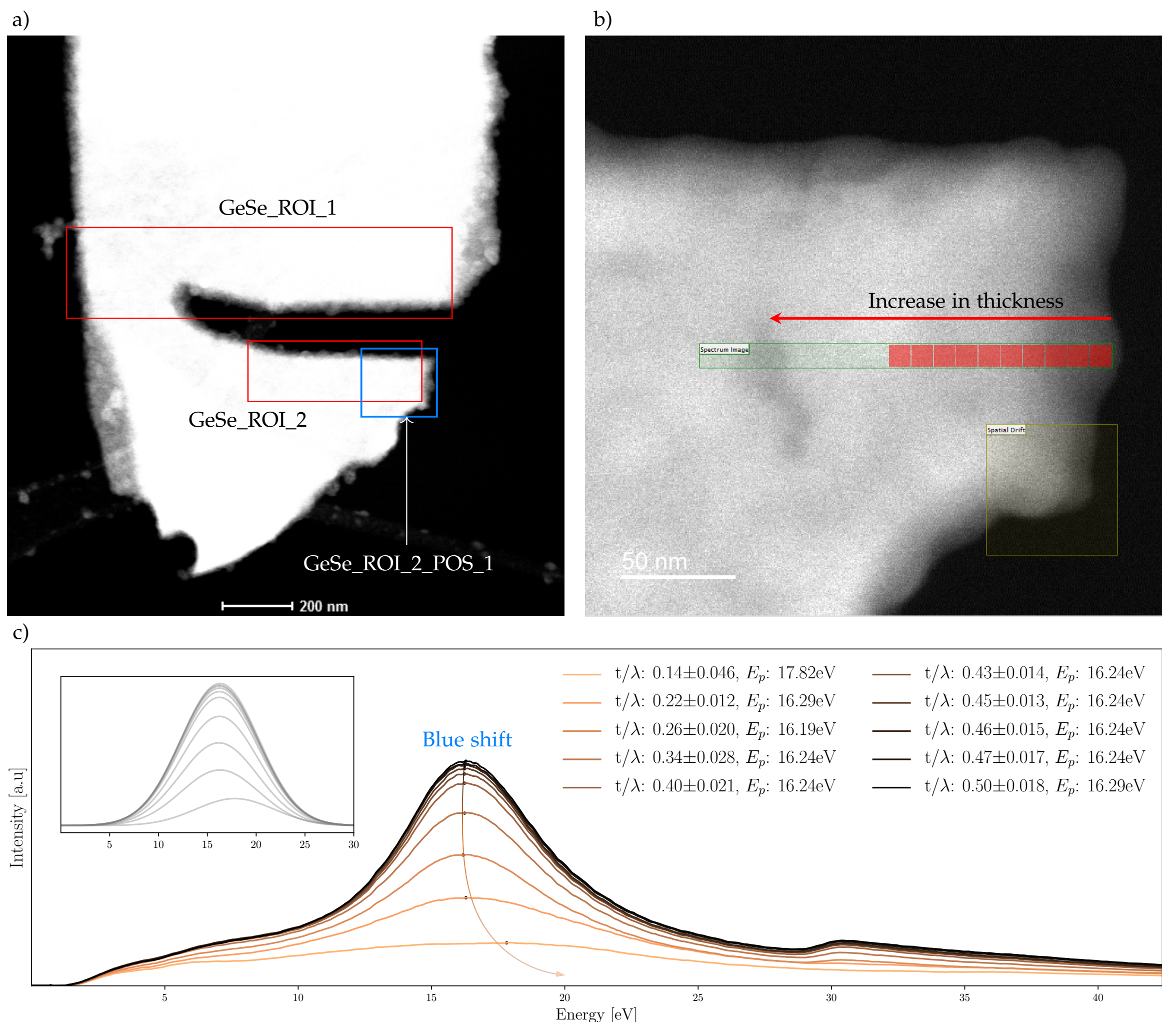

Figure 4.17: EELS measurements of GeSe_ROI_2_POS_1 acquired from the area annotated by the blue square in a).b) EELS measurements were done within the obtained EELS spectra shown by the green rectangle. Gradually increased thickness along the EELS spectra shown by the red arrow. Multiple red insets of 10x10nm was applied for Low-loss spectra at localised regions. c) Low-loss spectra of each red square from b). Dark lines indicates bulk region deep within the flake, and bright lines indicates quasi-two dimensional regions near the edge. Clear blue shift in plasmon peak is detected from bulk to quasi-two dimensions in GeSe.

figure 4.17b) we see the EELS spectra with 10x10nm red square insets. These insets are chosen and analysed individually in order to see clear thickness dependence in the plasmonic behaviour. As we previously mentioned we are able to analyse the average thickness in the EELS spectra from integral intensity profiles. By this we are able to collect a graph of the average thickness along the red arrow indicated in figure 4.17b). Once we have the thickness profile along the EELS spectra as well as correct dimensions, we calculated the average thickness of one 10x10nm inset. For further information of the thickness profile collected from the EELS spectra see Supplementary Information.

In figure 4.17c) we see the final Low-loss spectra from each individual square inset. Dark lines indicates bulk regions, deep within the flake. As the thickness is reduced, we see a clear decrease in intensity in the Low-loss spectra. This is due to a reduced amount of scattered electrons entering the GIF-entrance, as a consequence of the reduced thickness. Each Low-loss spectra has underwent a background-subtraction after calibrating the zero-loss peak. Furthermore, we analysed the position of plasmon peaks through a peak-finding algorithm. The dataset was transformed using a multiple gaussians-fit algorithm to exclude noice. In order to have a good approximation to the real values, the estimated Low-loss spectra had a root mean square $RMS = 10e^{-10}$. From this estimated function the plasmon peaks was found through a peak finding algorithm, which is based on the derivative and alternating signs. From this we found that the plasmon peaks had a clear blue shift in energy as the thickness was reduced. The shift in energy of the plasmon peak takes place at approximatly $\lesssim 22 \pm 1.2nm$ from $E_p \sim 16.30 - 17.83eV$. The inset in figure 4.17c) are pure gaussian functions from the estimated peaks in the Low-loss spectra.

As we previously mentioned, quasi-two dimensional materials tend to show a clear thickness dependency in bandgap energy. Further decreasing the dimensions to quasi-two dimensions quantum confinement effects becomes more prominent. The clear blue shift in plasmon peak could be related to the bandgap energy, as the number of layers (N) in GeSe is decreased so

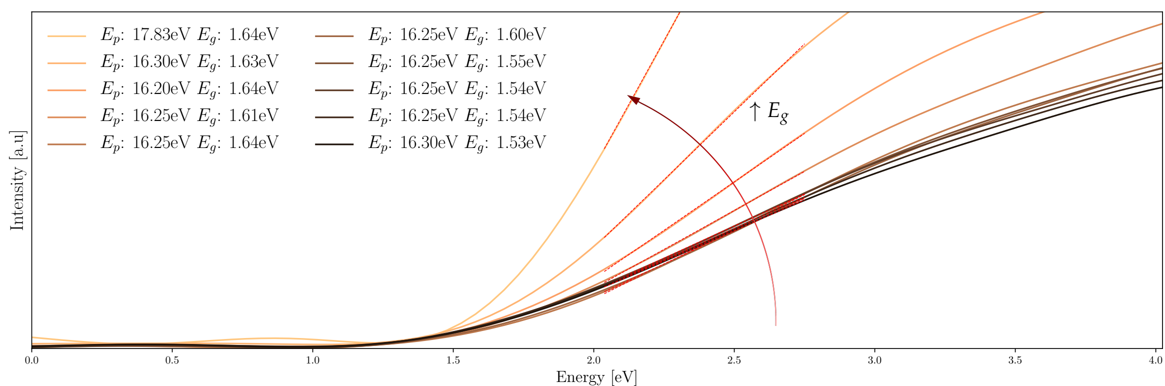

Figure 4.18: Bandgap estimation from Tauc plot method. Values collected from GeSe_ROI_2_POS_1, where each line is consistent with figure 4.17c). A clear increase in bandgap as the thickness is decreased is shown. From ∼1.53eV at ∼ 50±1.8nm to ∼1.64eV at ∼ 14±4.6nm

is the number of energy bands. Furthermore the surface-to-volume ratio is increasing with decreasing thickness, and the bandstructure becomes extremely sensitive to external interactions. This suggest that external interaction such as strain would modify the electronic bandstructure. There are two main factors which may provide a shift in plasmon peaks, as the thickness is decreased. The change in inter-atomic distance and dielectric constant. We have unfortunately, not measured these values.

In order to see a clear relation between plasmon peaks and bandgap, we estimated the bandgap through a linear fit method, which is frequently used in EELS [61]. The bandgap energy may be estimated from the intersection of a linear fit to the onset of the Low-loss spectra. The linear fit model was implemented on the Urbach tail as seen by figure 4.18. We are able to extract an estimation of the bandgap from each individual Low-loss spectrum

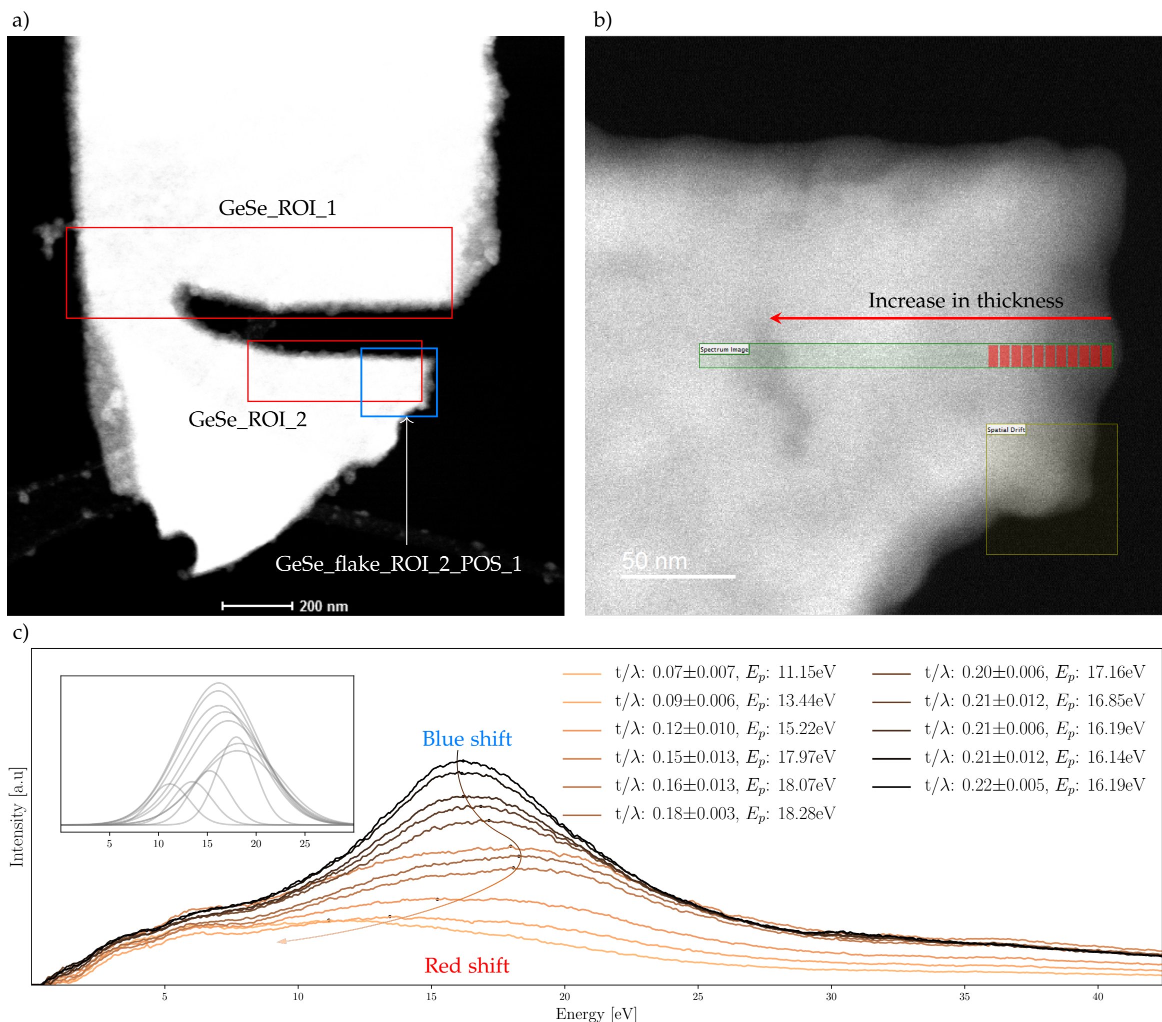

Figure 4.19: EELS measurements of GeSe_ROI_2_POS_1 acquired from the area annotated by the blue square in a).b) EELS measurements were done within the EELS spectra shown by the green rectangle. Gradually increased thickness along the EELS spectra shown by the red arrow. Multiple red insets of 1.5x10nm were applied for Low-loss spectra at localised regions. c) Low-loss spectra of each red square from b). Dark lines indicate bulk region deep within the flake, and bright lines indicate quasi-two dimensional regions near the edge. Both red and blue shifts of plasmon peaks was detected.

as seen in figure 4.17c), and we see a clear trend in in the variation in bandgap as a function of thickness and plasmon peak. The colour onset in figure 4.17c) is identical to that of figure 4.18. We see that the bandgap increases from $\sim 1.53eV$ at $t \sim 50 \pm 1.8nm$ to $\sim 1.64eV$ at $t \sim 14 \pm 4.6nm$. This does, however, not completely match that of plasmon peak variation. We see that the increase in bandgap starts around $t \sim 40nm$, where we do not have any clear shift in plasmon peak. The reason for this is unclear, even though multiple factors may intervene when collecting and analysing data from the EELS-measurments. As these measurements were not done with monochromated EELS, we are subject to low energy resolution, which consequently gives a poor estimate of the bandgap.

In Figure 4.19, we kept the same region of interest. We previously worked with 10x10nm insets, which gave a mean value of the Low-loss spectra as well as a mean thickness. The standard deviation of the average thickness from the 10x10 inset, seen in table 4.5, show an average deviation of $\sim 7.53\%$, we want to lower this value as well as the average thickness. As we see in figure 4.19b) the insets are decreased. In this case we have decreased them to 1.5x10nm. By narrowing down one dimension, we are able to get a more precise determination of the average thickness. Our new measurements show an average standard deviation of $\sim 6.04\%$, we have successfully reduced the average standard deviation, values of the standard deviation as well as thickness for each inset is seen in table 4.5. Furthermore, as seen by figure 4.19c) we have also successfully reduced the average thickness for each individual inset. By using $\lambda = 100nm$ we find the thinnest inset to be $t \sim 7 \pm 0.7nm$ which is around 8 monolayer of GeSe.

Table 4.5: Table of measured average thickness for each Low-loss spectrum in figure 4.17c) and 4.19c). Standard deviation of thickness is given by σ_t.

GeSe_flake_ROI_POS_1				
	10x10nm		*1.5x10nm*	
	Rel. t/λ	$\sigma_t[t/\lambda]$	Rel. t/λ	$\sigma_t[t/\lambda]$
—	0.14	0.046	0.07	0.007
—	0.22	0.012	0.09	0.006
—	0.26	0.020	0.12	0.010
—	0.34	0.028	0.15	0.013
—	0.40	0.021	0.16	0.013
—	0.43	0.014	0.18	0.003
—	0.45	0.013	0.20	0.006
—	0.46	0.015	0.21	0.012
—	0.47	0.017	0.21	0.006
—	0.50	0.018	0.22	0.012
—	–	–	0.21	0.005

The plasmon peaks show a peculiar variation which deviates from the plasmon peak variation in figure 4.17c). We can see that the plasmon peak show a clear blue shift in energy from around $t \sim 22 \pm 0.5nm$ to $t \sim 18 \pm 0.3nm$. Which is consistent with previous measurements of the 10x10nm inset. Once the thickness decreases below $t \sim 15 \pm 1.3nm$ we see a drastic red shift in plasmon peak energy. This red shift could be explained through surface plasmons. Once the quantum confinement effect becomes large, surface plasmon dominates over bulk plasmons. There has been reports of surface plasmon in atomically thin samples [38]. Where the plasmon peak energy showed a clear decrease in energy in contrast to the bulk plasmon peaks. The main reason could be that the excitation of a surface plasmon mode requires less energy than the bulk counterpart. The surface plasmon can be estimated from the simple relation [38]:

$$E_{sp} = \frac{E_p}{\sqrt{2}} \tag{4.1}$$

Bandgap measurements of the 1.5x10nm inset did not give any reliable data, as the number of incident electron scatterers sufficiently dropped from that of 10x10nm inset. The background subtraction proved to give an unreliable Urbach tail, as clearly seen in figure 4.19c), and the high noise-to-signal ratio gave insufficient results.

4.5 Plasmonic behaviour as a function of phase through EELS

We have by now analysed the elemental composition of the three main regions of interest; GeSe flake, Se-rich and Ge-rich phases. Furthermore we have determine the average thickness at the different locations. In the last section 4.4, we specifically looked at GeSe_ROI_2_POS_1, and saw clear plasmon peak dependency as a function of thickness. In this section we will look at each location to see a plasmon peak dependency as a function of elemental composition. As we already have seen, the plasmon peaks for pure GeSe, is around $\sim 16.25eV$. One would expect a shift in plasmon peak as a function of elemental composition, as the fundamental structural arrangement change with variation in atomic percentage. A number of factors within the structural arrangement could give a response in plasmon peaks. A change in the compositions space group would definitely change the bandstructure which consequently could give a shift in plasmon peak. Furthermore, slight increase or decrease in the interlayer distance (d), lattice vectors (a, b, c) and bond lengths would potentially give a shift in plasmon peaks.

In order to discover a potential plasmon peak shift as a function of phase we used the values calculated in tables 4.2,4.3 and 4.4. As we already have collected EELS spectra at these locations we are able to extract the average Low-loss spectra at these locations. As seen by figure 4.20a) the plasmon peak energy is plotted in the x-axis and every position of interest as mentioned in subsections 4.3.1 , 4.3.2 and 4.3.3 are plotted in the y-axis. The first column is represented by GeSe flake, and the plasmon peaks show an average energy of

~ 16.33, when excluding the 10x10nm_GeSe_ROI_2_POS_1. The measurements are taken as an average over the entire EELS spectra, if not stated otherwise. The black dot from the 10x10nm inset in figure 4.20a) show a plasmon peak at $\sim 17.82eV$, and is directly taken from the values in figure 4.17c), as we see, this value is extracted from the thinnest 10x10nm inset. We have already established that the plasmon peaks in pure GeSe shifts as a function of thickness, and we can with confident say that the plasmon peaks for pure GeSe is around $\sim 16.33eV$. As we saw from the EDX-analysis, we determined a stable atomic percentage of $Ge_{0.55}Se_{0.45}$. Naturally, as the surface-to-volume ratio increases the presence of oxygen becomes more prominent. It is possible to assume that the edge location suffers from a higher concentration of oxygen as mention previously, furthermore we have shown that the edges are Ge-rich.

The second column in figure 4.20a) show a trend in the Se-rich phase. On first sight, we see that the plasmon peaks has shifted up in energy by $\sim 1.53eV$, for the three positions in the second column, these three location show a high percentage of Selenium as we previously discussed. And the average plasmon peak energy was estimated to be $\sim 17.83eV$. We also note that the relative average thickness for these three positions were $\sim 33 \pm 9nm$, $\sim 76 \pm 23nm$ and $\sim 101 \pm 5nm$ for Se_ROI_1_POS_1, Se_ROI_1_POS_2 and Ge_ROI_1_POS_3, respectively. It is fair to assume that surface plasmon do not dominate within these regions.

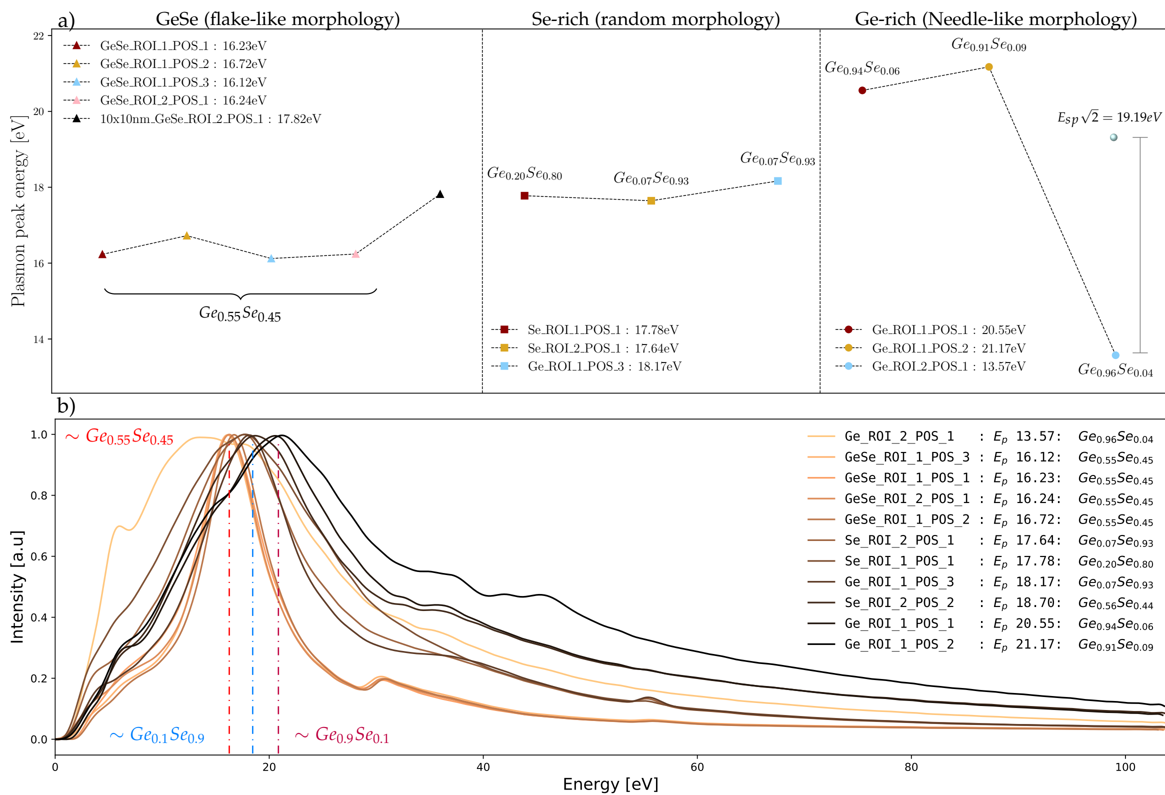

Figure 4.20: a) Diagram of plasmon peak energies as a function of phases. b) Designated Low-loss spectra from each position showing a clear shift in plasmon peak as a function of phase.

The third and final column in figure 4.20a) show the trend in the Ge-rich phase. When we analysed the elemental composition of the variety of regions we got a wide spread in atomic percentage at the different locations. The first two positions in the third column are nearly pure Germanium, which show an plasmon peak energy of $\sim 20.55eV$ and $\sim 21.17eV$, respectively. The average plasmon peaks energy results in a shift up in energy of $3.15eV$ from that of nearly pure selenium from column two. Furthermore, the last position in the third column; Ge_ROI_2_POS_1, show a peculiar plasmon peak at $13.57eV$. This discrepancy of plasmon peak energy compared average energy of $\sim 20.86eV$, suggest that surface plasmons dominate. By using the estimated equation for surface plasmons in equation 4.1, we find that the approximated bulk plasmon should be $\sim 19.19eV$. The average thickness at this location was calculated to be $48 \pm 5nm$. Even though we did not see any prominent surface plasmons at this thickness in pure GeSe, this could still be the case. A close look at figure 4.20b) reveals that the surface plasmon is accompanied by a shoulder peak which is the bulk plasmon counterpart.

In figure 4.20b) we simultaneously plot all Low-loss spectra for all positions discussed, except the localised 10x10nm insets. At first sight it is difficult to see a clear trend, the stippled lines indicates how the plasmon peak is shifted as a function of phase. We see that pure GeSe from the flake has the lowest plasmon peak energy, followed by $Ge_{0.1}Se_{0.9}$ at a slight increase of about $1.38eV$, thereafter followed by $Ge_{0.9}Se_{0.1}$ at an increase of about $3.15eV$. The plot of the spectra are normalized in order to see the shape of each plasmon peaks. One imminent feature of the plasmon peaks are the width. We can see that pure GeSe show narrow plasmon peaks in contrast to $Ge_{0.1}Se_{0.9}$ and $Ge_{0.9}Se_{0.1}$. The reason for an increase in width could be the fact that not all Low-loss spectra pixels yields the same plasmon peaks, so that when we are taking the average we are in fact observing a superposition of multiple plasmon peaks. We also see $Ge_{0.56}Se_{0.44}$, named Se_ROI_2_POS_2, which is nearly identical to that of GeSe flake. Even though the elemental composition is nearly identical, the plasmon peak energy is clearly shifted. We measured the average thickness in this EELS spectra in table 4.3, the value extracted was around $83 \pm 2nm$. This value is clearly bulk, which suggest that the peak should be around $\sim 16.33eV$. The plasmon peak energy is at $18.70eV$, which is in close proximity of the $t \sim 18 \pm 0.3nm$ plasmon peak at $18.28eV$ in figure 4.19c).

4.6 Bandgap measurements - EELS & micro-PL

Here we will make a small comparison between bandgap measurements from EELS in section 4.4 and micro-PL. Micro-PL technique allows for excitation spot of only a few microns in diameter, which potentially allows for addressing individual GeSe flakes. Furthermore, it has an advantages in leading to very high excitation intensities (of the order of 100kW/cm2). Micro-PL: Coaxial excitation configuration: OBJ X50 DM450+LP550 / iHR320Gr2 SL0.2 exc405nm (14mW FWHM 3um) Iexc ~100kW/cm2.

Micro-PL measurements of the sample was taken as a supplement to the EELS-measurements. The goal was to analyse and determine single sheet bandgap of GeSe. Throughout this chapter we have seen that we are not working with pure GeSe, there are multiple other phases involved as well. This would deem that our micro-PL results are solely from GeSe, as questionable at least. In figure 4.21b) we see the prope position for the measurements in a). The probe position were positioned at the highest density for increasing the probability of signal.

In figure 4.21a) we see the emission spectra from the measurements with a 405nm laser. We can see interband emission peaks around 1.8-2.3eV as it exceeds the expected bandgap of GeSe. Furthermore, we see a prominent emission band centred at $1.24eV$, this optical signal may be attributed to GeSe, however, little evidence suggest that this is indeed pure GeSe. Even though there have been reports of an optical signal of $\sim 1.20eV$ of triangular nanoplate arrays with thickness of $\geq 44nm$[60]. These results does not suggest any clear quantum confinement effects, as the thickness of an average flake is in the bulk region. There is also no evidence of Spin-Orbit coupling as discussed in section 2.4.4. The interference from other phases is also a reason to distrust these kind of measurements. As the emission spectra could contain the emission spectra from several different phases and thicknesses.

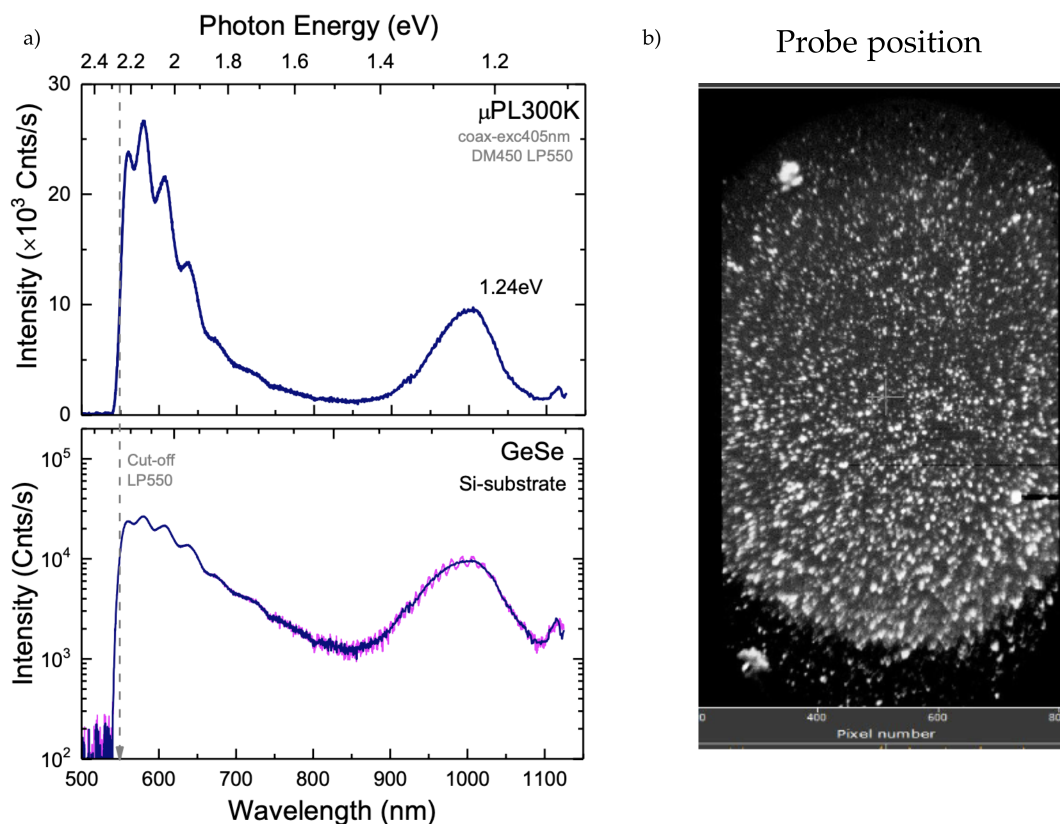

Figure 4.21: Micro-PL measurements of potential GeSe at 300K. a) Prominent emission band centred at around 1.24eV (∼1000nm) which might be an optical signature of GeSe. b) Probe position for measurements in a).

In comparison to our EELS-measurments there is an offset of about $\sim 0.3eV$, to the micro-PL measurements. The comparison is based upon the bulk values from EELS. Furthermore, an advantage of EELS is the spatial resolution. This yields opportunities of selecting localized regions of interest within the material for data-collection. As we saw in section 4.4, we were able to vary the measurements with extreme precision, controlling the thickness variation and enabling bandgap measurements through the linear method. As there are advantages with EELS there are also disadvantages in comparison to micro-PL. In EELS, one subject to lower energy resolution, which may yield inaccurate measurements. With this in mind, we might be subject of inaccurate measurements of EELS when we estimated the bandgap.

Chapter 5

Conclusion

In summary, we purchased GeSe mono-and few-layer thick flakes dispensed in IPA from *2dsemiconductors Inc*, to analyse the plasmonic behaviour as a function of thickness and phases. In section 4.2, we analysed the topography of the sample after depositing GeSe solution on Si-substrate. A numerous optical images as well as SEM images gave a greater understanding of the shapes and sizes of the material dispensed in IPA. The optical images were analysed through a histogram of the flake size along the elongated direction, and a mean value of $3.049\mu m$ with a standard deviation $\sigma = 1.821$ was calculated. Furthermore, the SEM images collected showed what is believed to be pure GeSe, with the exception of the needle, and other irregularly shaped particles. Clear step-size topography revealed itself in the SEM images. In addition to optical and SEM images, the topography was investigated through AFM. Two successful AFM images was analysed, and showed clear step-size behaviour. Multiple line profiles was placed on the collected image. With the assumption that a monolayer is 0.54nm and the interlayer distance is in the range of $d = 2.60 - 3.37$Å, the line profiles revealed around $\sim 3 - 10$ monolayers of GeSe. Which is, to the best of our knowledge, the only result confirming a 3 monolayer GeSe from AFM-measurements.

Topography analysis was implemented for a greater understanding of the sample under investigation. As we saw in section 4.2, multiple phases of GeSe was present. In section 4.3, a number of EDX-maps was presented as well as STEM images. Firstly, we analysed the GeSe flake which proved to be pure GeSe, however, no clear step-size structure was detected from the STEM images. High resolution STEM images were taken from the GeSe_flake, which gave lattice spacings of 0.284nm consistent with the (111) plane, and of 0.289nm which matches the (011) plane, according to literature. The EDX-maps showed a clear decrease in Selenium near the edges of GeSe_flake, which could be due to higher surface-to-volume ratio, which could increase the possibility of oxidation. Even though, there have been reports that $\alpha - GeSe$[50], and $\beta - GeSe$ [53] are stable under ambient conditions. Two other regions of interest was analysed for their elemental composition, namely, Se-rich and Ge-rich. The EDX-maps revealed a wide variation in the elemental composition ranging from $\sim Ge_{0.9}Se_{0.1}$ to $\sim Ge_{0.1}Se_{0.9}$, which gave an intriguing opportunity of analysing plasmonic behaviour as a function of phases.

The main goal was to investigate the plasmonic behaviour as a function of thickness and phases. In section 4.4 we analysed one region in GeSe flake with EELS. A clear trend in plasmonic behaviour was seen by varying the thickness of the sample. We observed both blue and red shift in plasmon energy. The blue shift resulted in an increase in conduction band energy which consequently increased the bandgap. The bandgap was estimated through a linear method allowing us to see a clear increase in bandgap as the thickness decreased. Furthermore, we decreased the size of average Low-loss spectra enabling analysis of thinner regions on GeSe. The results showed a clear blue shift followed by a red shift at thickness below $\sim 15 \pm 1.3nm$. This red shift could be explained by surface plasmons. As the surface-to-volume ratio is sufficiently large, the effect of surface plasmon surpasses that of bulk plasmon, and surface plasmon is lower in energy compared to that of bulk plasmons by a factor of $\sqrt{2}$ according to [38]. In section 4.5, every Low-loss spectra presented was analysed as an average in order to see a trend in plasmon peaks as a function of phases. We could see a clear shift in plasmon peak energy as the atomic percentage changed. In addition, average thickness was calculated at each EELS spectra obtained to rule out any potential surface plasmons. Some discrepancies occurred, but a clear blue shift took place from $\sim Ge_{0.5}Se_{0.5}$, $\sim Ge_{0.1}Se_{0.9}$ to $\sim Ge_{0.9}Se_{0.1}$. The variation in plasmon width could be determined through the average measurements taken, where we could very well be observing a superposition of multiple plasmon peaks.

Finally, a brief comparison of EELS and micro-PL was discussed. We estimated the bandgap through EELS and found a clear increase in bandgap as the thickness was reduced. These measurements showed a bandgap from $\sim 1.53eV$ at $\sim 50 \pm 1.8nm$ to $\sim 1.64eV$ at $\sim 14 \pm 4.6nm$. On the other hand, micro-PL measurements gave a prominent emission band centred at 1.24eV, which contradict our EELS measurements. The reason are manifold, as we have pros and cons in both techniques. Mainly, the energy precision in micro-PL surpasses that of EELS, while EELS provide a much greater spatial resolution than micro-PL. Furthermore, micro-PL measurements may collect some signal from the other phases discussed which could influence the emission band observed. The EELS-measurements that provided the bandgap estimation, could overestimate the bandgap, however, there are reasons to believe that the bandgap variation as a function of thickness is a real property observed.

Suggestions for Further Work

In this work the plasmonic behaviour as a function of thickness and phases were analysed. The purchased GeSe dispensed in IPA, proved to be consistent of multiple different atomic concentrations of Germanium and Selenium. This gave us a genuine opportunity of analysing the different phases occurring through plasmons.

For future work, one could optimise EELS measurements for higher accuracy, as well as gather Low-loss spectra at even thinner regions. One would perhaps not expect any fundamentally different results if the thickness decreased even further, as surface plasmon dominate. In addition to analysing different regions of pure two-dimensional thickness, it would be highly beneficial to conduct strain analysis of the different phases. In this work, no strain analysis were done. It is therefore difficult to solely attribute the plasmonic behaviour to either thickness and phases. Especially, strain analysis near the edge of the pure GeSe flake would yield some interesting result regarding the shift in energy as well as bandgap. At least in order to determine what is the most reasonable cause of the plasmonic behaviour.

Furthermore, the bandgap analysis conducted through EELS were a rough estimate which suffers from unreliable data due to low energy resolution. A suggestion would be to implement a higher energy resolution to EELS measurements, in order to give a more accurate bandgap estimate - by applying monochromation and work at 60kV to reduce Cherenkov radiation effects. In addition, it would be interesting to create a 2D map of the plasmon peaks from the low-loss spectra. This would in turn yield a 2D map of the bandgaps at different pixels at the low-loss spectra. One would then in theory be able to see a clear bandgap correlation to the plasmon peaks - which could confirm or disconfirm this theory.

A more far-fetched approach could be to manipulate the zone axis for a better understanding of the band structure. By changing the zone axis to multiple different direction, prior to EELS measurements, one could in theory collect the bandgap of a specified high symmetry point (in reference to the irreducible Brillouin zone). Electron traveling along a lattice direction specified by the zone-axis indices [uvw], would then be scattered along this high symmetry point, potentially yielding the plasmonic behaviour as well as the bandgap. If this could be realised, a unique technique for analysing the band structure of semiconductors would be feasible, without any density functional theory applied.

Appendix A

Effective mass I

Let us consider the **effective mass** of an electron or hole in a semiconductor. The simplest way to go about is to treat the eigenvalue of the schrodinger equation as a free electron experiencing no external potential, the energy dispersion is then:

$$E(\mathbf{k}) = E_0 + \frac{\hbar^2 \mathbf{k}^2}{2m} \tag{A.1}$$

Which is the energy of a free electron. The number of electrons in the conduction band, as well as the number of holes in the valence band, is small compared to the number of available electronic states in all cases of relevance, and the few carriers will find themselves in close proximity to the band extremal points. Around these extremal points, we can expand the energy dispersion in a Taylor series up to second order:

$$E(\mathbf{k}) \approx E_0 + \mathbf{k} \left. \frac{\partial E}{\partial k_i} \right|_{\mathbf{k}=0} + \frac{1}{2} k^2 \left. \frac{\partial^2 E}{\partial k_i \partial k_j} \right|_{\mathbf{k}=0} + ... \tag{A.2}$$

Where the first derivative around the extramal points is zero, so we are only left with the second order term. Now we may insert the energy for the free electorn into the expansion of around the extrema points.

$$E_0 + \frac{\hbar^2 k^2}{2m} \approx E_0 + \frac{1}{2} k^2 \left. \frac{\partial^2 E}{\partial k_i \partial k_j} \right|_{\mathbf{k}=0} \tag{A.3}$$

Which then yield the effective mass, which is dependent on the second order derivative of energy with respect to **k**.

$$\left(\frac{1}{m^*} \right)_{ij} \approx \frac{1}{\hbar^2} \left. \frac{\partial^2 E}{\partial k_i \partial k_j} \right|_{\mathbf{k}=0} \tag{A.4}$$

Here the effective mass is a second order tensor defines the efficive masses along different crystal directions. Take for example Si and GaAs. Si has a indirect bandgap where the valence band is located around the Γ point whereas the conduction band is located close to the X point. Because the X point is symmetric, and has six equivalent points in the

first Brillouin zone, the masses need to be determined by the effective mass tensor. The crystal structures is identical but the bandstructur is different, yielding bandgaps at different high symmetry point within the 1.st Brillouin. At the Γ point for GaAs there is no Valley degenerated states, because the Γ has no equivalent positions. So for GaAs the electron effective mass simply becomes a scalar of m_e^*.

References

[1] K. S. Novoselov, A. K. Geim, S. V. Morozov, D. Jiang, Y. Zhang, S. V. Dubonos, I. V. Grigorieva, and A. A. Firsov, “Electric field effect in atomically thin carbon films”, *science*, vol. 306, no. 5696, pp. 666–669, 2004.

[2] S. Pisana, M. Lazzeri, C. Casiraghi, K. S. Novoselov, A. K. Geim, A. C. Ferrari, and F. Mauri, “Breakdown of the adiabatic born–oppenheimer approximation in graphene”, *Nature materials*, vol. 6, no. 3, pp. 198–201, 2007.

[3] Y. Ye, Q. Guo, X. Liu, C. Liu, J. Wang, Y. Liu, and J. Qiu, “Two-dimensional gese as an isostructural and isoelectronic analogue of phosphorene: Sonication-assisted synthesis, chemical stability, and optical properties”, *Chemistry of Materials*, vol. 29, no. 19, pp. 8361–8368, 2017.

[4] P. Ramasamy, D. Kwak, D.-H. Lim, H.-S. Ra, and J.-S. Lee, “Solution synthesis of ges and gese nanosheets for high-sensitivity photodetectors”, *Journal of Materials Chemistry C*, vol. 4, no. 3, pp. 479–485, 2016.

[5] D. D. Vaughn, R. J. Patel, M. A. Hickner, and R. E. Schaak, “Single-crystal colloidal nanosheets of ges and gese”, *Journal of the American Chemical Society*, vol. 132, no. 43, pp. 15 170–15 172, 2010.

[6] Y. Mao, X. Mao, H. Zhao, N. Zhang, X. Shi, and J. Yuan, “Enhancement of photoluminescence efficiency in gese ultrathin slab by thermal treatment and annealing: Experiment and first-principles molecular dynamics simulations”, *Scientific reports*, vol. 8, no. 1, pp. 1–9, 2018.

[7] X. Zhou, X. Hu, B. Jin, J. Yu, K. Liu, H. Li, and T. Zhai, “Highly anisotropic gese nanosheets for phototransistors with ultrahigh photoresponsivity”, *Advanced science*, vol. 5, no. 8, p. 1 800 478, 2018.

[8] H. Zhao, Y. Mao, X. Mao, X. Shi, C. Xu, C. Wang, S. Zhang, and D. Zhou, “Band structure and photoelectric characterization of gese monolayers”, *Advanced Functional Materials*, vol. 28, no. 6, p. 1 704 855, 2018.

[9] H Cohen, P Rez, T Aoki, P. Crozier, N Dellby, Z Dellby, D Gur, T. Lovejoy, K March, M. Sarahan, *et al.*, “Hydrogen analysis by ultra-high energy resolution eels”, *Microscopy and Microanalysis*, vol. 21, no. S3, pp. 661–662, 2015.

[10] C. Kittel, “Introduction to solid state physics”, 1976.

[11] K. W. Böer and U. W. Pohl, *Semiconductor physics*. Springer, 2018.

[12] T. Heinzel and I. Zozoulenko, *Mesoscopic electronics in solid state nanostructures*. Wiley Online Library, 2003, vol. 3.

[13] D. Ferry and S. M. Goodnick, *Transport in nanostructures*, 6. Cambridge university press, 1999.

[14] R. P. Feynman, “Space-time approach to quantum electrodynamics”, *Physical Review*, vol. 76, no. 6, p. 769, 1949.

[15] G. Cunningham, M. Lotya, C. S. Cucinotta, S. Sanvito, S. D. Bergin, R. Menzel, M. S. Shaffer, and J. N. Coleman, “Solvent exfoliation of transition metal dichalcogenides: Dispersibility of exfoliated nanosheets varies only weakly between compounds”, *ACS nano*, vol. 6, no. 4, pp. 3468–3480, 2012.

[16] A. P. Gaur, S. Sahoo, M. Ahmadi, S. P. Dash, M. J.-F. Guinel, and R. S. Katiyar, “Surface energy engineering for tunable wettability through controlled synthesis of mos2”, *Nano letters*, vol. 14, no. 8, pp. 4314–4321, 2014.

[17] R Winkler, S Papadakis, E De Poortere, and M Shayegan, *Spin-Orbit Coupling in Two-Dimensional Electron and Hole Systems*. Springer, 2003, vol. 41.

[18] W. Li, M. Guo, G. Zhang, and Y.-W. Zhang, “Gapless mos 2 allotrope possessing both massless dirac and heavy fermions”, *Physical Review B*, vol. 89, no. 20, p. 205 402, 2014.

[19] T. Mueller and E. Malic, “Exciton physics and device application of two-dimensional transition metal dichalcogenide semiconductors”, *npj 2D Materials and Applications*, vol. 2, no. 1, pp. 1–12, 2018.

[20] N. S. Arul and V. D. Nithya, *Two Dimensional Transition Metal Dichalcogenides: Synthesis, Properties, and Applications*. Springer, 2019.

[21] A. V. Kolobov and J. Tominaga, *Two-dimensional transition-metal dichalcogenides*. Springer, 2016, vol. 239.

[22] D. Allender, J. Bray, and J. Bardeen, “Model for an exciton mechanism of superconductivity”, *Physical Review B*, vol. 7, no. 3, p. 1020, 1973.

[23] A. Kavokin and P. Lagoudakis, “Exciton–polariton condensates: Exciton-mediated superconductivity”, *Nature materials*, vol. 15, no. 6, pp. 599–600, 2016.

[24] T. Olsen, S. Latini, F. Rasmussen, and K. S. Thygesen, “Simple screened hydrogen model of excitons in two-dimensional materials”, *Physical review letters*, vol. 116, no. 5, p. 056 401, 2016.

[25] R. F. Egerton *et al.*, *Physical principles of electron microscopy*. Springer, 2005, vol. 56.

[26] E. Ruska, “The development of the electron microscope and of electron microscopy”, *Bioscience reports*, vol. 7, no. 8, pp. 607–629, 1987.

[27] C. B. Carter and D. B. Williams, *Transmission electron microscopy: Diffraction, imaging, and spectrometry*. Springer, 2016.

[28] P. Tiemeijer, M Bischoff, B Freitag, and C Kisielowski, “Using a monochromator to improve the resolution in tem to below 0.5 Å. part i: Creating highly coherent monochromated illumination”, *Ultramicroscopy*, vol. 114, pp. 72–81, 2012.

[29] C. S. Granerød, W. Zhan, and Ø. Prytz, “Automated approaches for band gap mapping in stem-eels”, *Ultramicroscopy*, vol. 184, pp. 39–45, 2018.

[30] C. S. Granerød, A. Galeckas, K. M. Johansen, L. Vines, and Ø. Prytz, "The temperature-dependency of the optical band gap of zno measured by electron energy-loss spectroscopy in a scanning transmission electron microscope", *Journal of Applied Physics*, vol. 123, no. 14, p. 145 111, 2018.

[31] E. Okunishi, I. Ishikawa, H. Sawada, F. Hosokawa, M. Hori, and Y. Kondo, "Visualization of light elements at ultrahigh resolution by stem annular bright field microscopy", *Microscopy and Microanalysis*, vol. 15, no. S2, pp. 164–165, 2009.

[32] R. Egerton and M Malac, "Eels in the tem", *Journal of Electron Spectroscopy and Related Phenomena*, vol. 143, no. 2-3, pp. 43–50, 2005.

[33] B Rafferty and L. Brown, "Direct and indirect transitions in the region of the band gap using electron-energy-loss spectroscopy", *Physical Review B*, vol. 58, no. 16, p. 10 326, 1998.

[34] P. Batson, K. Kavanagh, J. Woodall, and J. Mayer, "Electron-energy-loss scattering near a single misfit dislocation at the gaas/gainas interface", *Physical review letters*, vol. 57, no. 21, p. 2729, 1986.

[35] S Lazar, G. Botton, M.-Y. Wu, F. Tichelaar, and H. Zandbergen, "Materials science applications of hreels in near edge structure analysis and low-energy loss spectroscopy", *Ultramicroscopy*, vol. 96, no. 3-4, pp. 535–546, 2003.

[36] U Buechner, "The dielectric function of mica and quartz determined by electron energy losses", *Journal of Physics C: Solid State Physics*, vol. 8, no. 17, p. 2781, 1975.

[37] R. F. Egerton, *Electron energy-loss spectroscopy in the electron microscope*. Springer Science & Business Media, 2011.

[38] C. S. Granerød, S. R. Bilden, T. Aarholt, Y.-F. Yao, C. Yang, D. C. Look, L. Vines, K. M. Johansen, and Ø. Prytz, "Direct observation of conduction band plasmons and the related burstein-moss shift in highly doped semiconductors: A stem-eels study of ga-doped zno", *Physical Review B*, vol. 98, no. 11, p. 115 301, 2018.

[39] R.-w. Shao, K. Zheng, B. Wei, Y.-f. Zhang, Y.-j. Li, X.-d. Han, Z. Zhang, and J. Zou, "Bandgap engineering and manipulating electronic and optical properties of zno nanowires by uniaxial strain", *Nanoscale*, vol. 6, no. 9, pp. 4936–4941, 2014.

[40] J. Palisaitis, C.-L. Hsiao, M. Junaid, J. Birch, L. Hultman, and P. Å. Persson, "Effect of strain on low-loss electron energy loss spectra of group-iii nitrides", *Physical Review B*, vol. 84, no. 24, p. 245 301, 2011.

[41] T. Lovejoy, Q. Ramasse, M Falke, A Kaeppel, R Terborg, R Zan, N Dellby, and O. Krivanek, "Single atom identification by energy dispersive x-ray spectroscopy", *Applied Physics Letters*, vol. 100, no. 15, p. 154 101, 2012.

[42] D. B. Williams and C. B. Carter, "The transmission electron microscope", in *Transmission electron microscopy*, Springer, 1996, pp. 3–17.

[43] Y. Zhang, H. Li, H. Wang, R. Liu, S.-L. Zhang, and Z.-J. Qiu, "On valence-band splitting in layered mos2", *ACS nano*, vol. 9, no. 8, pp. 8514–8519, 2015.

[44] D. Bing, Y. Wang, J. Bai, R. Du, G. Wu, and L. Liu, "Optical contrast for identifying the thickness of two-dimensional materials", *Optics Communications*, vol. 406, pp. 128–138, 2018.

[45] F. J. Giessibl, “Atomic resolution of the silicon (111)-(7x7) surface by atomic force microscopy”, *Science*, vol. 267, no. 5194, pp. 68–71, 1995.

[46] C. Quate, C. Gerber, and C Binnig, “Atomic force microscope”, *Phys. Rev. Lett*, vol. 56, no. 9, pp. 930–933, 1986.

[47] G. Gilliland, “Photoluminescence spectroscopy of crystalline semiconductors”, *Materials Science and Engineering: R: Reports*, vol. 18, no. 3-6, pp. 99–399, 1997.

[48] A. K. Geim, “Graphene: Status and prospects”, *science*, vol. 324, no. 5934, pp. 1530–1534, 2009.

[49] A. K. Geim and K. S. Novoselov, “The rise of graphene”, in *Nanoscience and technology: a collection of reviews from nature journals*, World Scientific, 2010, pp. 11–19.

[50] S. Zhang, S. Liu, S. Huang, B. Cai, M. Xie, L. Qu, Y. Zou, Z. Hu, X. Yu, and H. Zeng, “Structural and electronic properties of atomically thin germanium selenide polymorphs”, *Science China Materials*, vol. 58, no. 12, pp. 929–935, 2015.

[51] K. Momma and F. Izumi, “Vesta 3 for three-dimensional visualization of crystal, volumetric and morphology data”, *Journal of applied crystallography*, vol. 44, no. 6, pp. 1272–1276, 2011.

[52] X. Lv, W. Wei, Q. Sun, F. Li, B. Huang, and Y. Dai, “Two-dimensional germanium monochalcogenides for photocatalytic water splitting with high carrier mobility”, *Applied Catalysis B: Environmental*, vol. 217, pp. 275–284, 2017.

[53] F. O. Von Rohr, H. Ji, F. A. Cevallos, T. Gao, N. P. Ong, and R. J. Cava, “High-pressure synthesis and characterization of b-gese a six-membered-ring semiconductor in an uncommon boat conformation”, *Journal of the American Chemical Society*, vol. 139, no. 7, pp. 2771–2777, 2017.

[54] Y. Hu, S. Zhang, S. Sun, M. Xie, B. Cai, and H. Zeng, “Gese monolayer semiconductor with tunable direct band gap and small carrier effective mass”, *Applied Physics Letters*, vol. 107, no. 12, p. 122 107, 2015.

[55] L. C. Gomes and A Carvalho, “Phosphorene analogues: Isoelectronic two-dimensional group-iv monochalcogenides with orthorhombic structure”, *Physical Review B*, vol. 92, no. 8, p. 085 406, 2015.

[56] P. A. Murgatroyd, M. J. Smiles, C. N. Savory, T. P. Shalvey, J. E. Swallow, N. Fleck, C. M. Robertson, F. Jackel, J. Alaria, J. D. Major, *et al.*, “Gese: Optical spectroscopy and theoretical study of a van der waals solar absorber”, *Chemistry of Materials*, vol. 32, no. 7, pp. 3245–3253, 2020.

[57] Y. Xu, K. Xu, C. Ma, Y. Chen, H. Zhang, Y. Liu, and Y. Ji, “Novel two-dimensional b-gese and b-snse semiconductors: Anisotropic high carrier mobility and excellent photocatalytic water splitting”, *Journal of Materials Chemistry A*, vol. 8, no. 37, pp. 19 612–19 622, 2020.

[58] Y. Xu, H. Zhang, H. Shao, G. Ni, J. Li, H. Lu, R. Zhang, B. Peng, Y. Zhu, H. Zhu, *et al.*, “First-principles study on the electronic, optical, and transport properties of monolayer a-and b-gese”, *Physical Review B*, vol. 96, no. 24, p. 245 421, 2017.

[59] L. Xu, M. Yang, S. J. Wang, and Y. P. Feng, “Electronic and optical properties of the monolayer group-iv monochalcogenides m x (m= ge, sn; x= s, se, te)”, *Physical Review B*, vol. 95, no. 23, p. 235 434, 2017.

[60] X. Li, X. Zhang, X. Lv, J. Pang, L. Lei, Y. Liu, Y. Peng, and G. Xiang, “Synthesis and photoluminescence of high density gese triangular nanoplate arrays on si substrates”, *Nanotechnology*, vol. 31, no. 28, p. 285 702, 2020.

[61] J. Park, S. Heo, J.-G. Chung, H. Kim, H. Lee, K. Kim, and G.-S. Park, “Bandgap measurement of thin dielectric films using monochromated stem-eels”, *Ultramicroscopy*, vol. 109, no. 9, pp. 1183–1188, 2009.